Meningeal macrophages protect against viral neuroinfection

Julie Rebejac, Elisa Eme-Scolan, Laurie Arnaud Paroutaud, Sarah Kharbouche, Matei Teleman, Lionel Spinelli, Emeline Gallo, Annie Roussel-Queval, Ana Zarubica, Amandine Sansoni, et al.

› Immunity. 2022 Nov 8;55(11):2103-2117.e10. doi: 10.1016/j.immuni.2022.10.005. Epub 2022 Nov 1.

Meningeal macrophages protect against viral neuroinfection

Julie Rebejac [1], Elisa Eme-Scolan [2], Laurie Arnaud Paroutaud [1], Sarah Kharbouche [1], Matei Teleman [1], Lionel Spinelli [1], Emeline Gallo [1], Annie Roussel-Queval [1], Ana Zarubica [3], Amandine Sansoni [3], Quentin Bardin [3], Philippe Hoest [3], Marie-Cécile Michallet [4], Carine Brousse [1], Karine Crozat [1], Monica Manglani [5], Zhaoyuan Liu [6], Florent Ginhoux [7], Dorian B McGavern [5], Marc Dalod [1], Bernard Malissen [8], Toby Lawrence [9], Rejane Rua [10]

Affiliations + expand

PMID: 36323311 DOI: 10.1016/j.immuni.2022.10.005

Meningeal macrophages protect against viral neuroinfection

Julie Rebejac(1), Elisa Eme-Scolan(1,2), Laurie Arnaud Paroutaud(1), Sarah Kharbouche(1), Matei Teleman(1), Lionel Spinelli(1), Emeline Gallo(1), Annie Roussel-Queval(1), Ana Zarubica(3), Amandine Sansoni(3), Quentin Bardin(3), Philippe Hoest(3), Marie-Cécile Michallet(4), Carine Brousse(1), Karine Crozat (1), Monica Manglani(5), Zhaoyuan Liu(6), Florent Ginhoux(6,7,8), Dorian B. McGavern(5), Marc Dalod(1), Bernard Malissen(1,3), Toby Lawrence(1,9) & Rejane Rua(1, 10, *)

Affiliations:

(1) Centre d'Immunologie de Marseille-Luminy, Aix Marseille Université, Inserm, CNRS, Marseille, France

(2) École Normale Supérieure de Lyon, Université Claude Bernard Lyon I, Université de Lyon, Lyon, France

(3) Centre d'Immunophénomique, Aix Marseille Université, Inserm, CNRS, Marseille, France

(4) TERI (Tumor Escape, Resistance and Immunity) Department, Centre de Recherche en Cancérologie de Lyon, Centre Léon Bérard, Université Claude Bernard Lyon 1, Université de Lyon, Inserm, CNRS, Lyon, France

(5) Viral Immunology and Intravital Imaging Section, National Institute of Neurological Disorders and Stroke, National Institutes of Health, Bethesda, MD 20892, USA

(6) Shanghai Institute of Immunology, Shanghai Jiao Tong University School of Medicine, Shanghai, China.

(7) University Paris-Saclay, INSERM U1015, Gustave Roussy Cancer Center, Villejuif, France

(8) Singapore Immunology Network, A*STAR, Singapore, Singapore

(9) Centre for Inflammation Biology and Cancer Immunology, Cancer Research UK King's Health Partners Centre, School of Immunology and Microbial Sciences, King's College London, UK

(10) Lead contact

*** Correspondence:** rua@ciml.univ-mrs.fr

Summary

The surface of the central nervous system (CNS) is protected by the meninges, which contain a dense network of meningeal macrophages (MM). However, the role of MM in protecting the brain from infection remains unknown (QUESTION). Using histocytometry, flow cytometry and single-cell RNA sequencing, we analyzed 2 MM populations: MHC-II- MM which were abundant neonatally and MHC-II+ MM which appeared over time (FIGURE 1,2). Those barrier macrophages differentially responded to *in vivo* peripheral challenges such as LPS, SARS-CoV2 and lymphocytic choriomeningitis virus (LCMV) (FIGURE 2). Focusing on LCMV, we found that even a peripheral and asymptomatic infection led to a transient infection and activation of the meninges (FIGURE 3). We then used a novel genetic depletion strategy and found that in mice lacking macrophages but conserving brain microglia (FIGURE 4), or in mice with *Stat1*- or *Ifnar*-deficient macrophages (FIGURE 5), the virus could massively spread into the CNS. Similarly, using innovative transcranial pharmacological depletion strategies to better target MM locally, we confirmed that in their absence, several areas of the meninges became highly infected, leading to fatal brain disease (FIGURE 6). Moreover, experimental models with low levels of MHC-II+ MM were correlated with stronger brain viral load (FIGURE 7). Thus, MM populations represent a major line of protection against neuroinfection (TAKE HOME MESSAGE).

Introduction

The central nervous system (CNS) is protected from the periphery by different anatomical barriers which ensure its structural integrity (Banks, 2016). While several studies have focused on the neuroprotective role of the blood-brain barrier and the choroid plexus, much less is known about the barrier localized at the surface of the CNS (Banks, 2016; Dragunow, 2013; Rua and McGavern, 2018; Schwartz and Baruch, 2014). The surface of the CNS (brain and spinal cord) is connected to the periphery by highly vascularized membranes devoid of a blood-brain barrier, the meninges (Rua and McGavern, 2018; Rustenhoven et al., 2021; Weller et al., 2018). The outer layer is called the 'dura mater' while the inner layer also called 'leptomeninges' contains the arachnoid and the pia mater, between which circulates the cerebrospinal fluid (Rua and McGavern, 2018). Meninges were thought to represent an inert connective tissue. However, similar to other barrier tissues in the skin, lung and intestine, the meninges (especially the dura mater, the focus of this study) are populated by a myriad of resident immune sentinels such as dendritic cells, lymphocytes, mast cells and also macrophages, the most abundant population (Brioschi et al., 2021; Cugurra et al., 2021; Fitzpatrick et al., 2020; Goldmann et al., 2016; Korin et al., 2017; Mrdjen et al., 2018; Rua and McGavern, 2018; Schafflick et al., 2021; Van Hove et al., 2019). Due to their strategic localization at the interface between the periphery and the brain, immune cells in the meninges can communicate with both compartments. In particular, the sinuses that drain venous blood from the meninges, the brain and the skull, are highly surveilled and constitute an immune hub (Rustenhoven et al., 2021). At homeostasis, meningeal immune cells are already known to contribute to social and cognitive behavior in particular through the release of IL4, IFNγ and IL17, released by CD4+ or γδ T lymphocytes (Brynskikh et al., 2008; Ellwardt et al., 2016; Kipnis et al., 2004; Kipnis et al., 2012; Salvador et al., 2021). On the other hand, due to the high density of immune cells located in the meninges, the immune system is also involved in neuro-inflammatory diseases (Ma et al., 2021; Waisman et al., 2015). For instance, we and others have shown that innate lymphocytes in the dural meninges can initiate and propagate neuroinflammation in cases of autoimmune diseases (Kwong et al., 2017; Rua and McGavern, 2018). In infection models, neutrophil recruitment in the meninges and the parenchyma has been shown to promote vascular pathology (Kim et al., 2009), while IgA+ producing plasma cells located at the dural meningeal sinuses were shown to protect the brain from *Candida albicans* infection (Fitzpatrick et al., 2020).

In contrast to neutrophils and lymphocytes, the role of meningeal macrophages in neuroinflammation has been elusive so far. In EAE, antigen-presentation by meningeal macrophages seemed dispensable for disease progression (Jordao et al., 2019). However, meningeal macrophages could play a role in different CNS challenges, such as infections. The surface of the CNS is seeded by 2 populations of tissue-resident meningeal macrophages

(MM), MHC-II+ and MHC-II- of elusive functions (Mrdjen et al., 2018; Prinz et al., 2017; Rua et al., 2019; Van Hove et al., 2019). In contrast with macrophages differentiating from blood monocytes during the peak or the resolution phase of a disease, which have been extensively studied, the function of tissue-resident macrophages is just starting to be elucidated (Ginhoux et al., 2016; Guilliams and Scott, 2017; Perdiguero and Geissmann, 2016; Utz et al., 2020). Whether MM populations control viral neuroinvasion or promote inflammation, and by which mechanisms, is unknown.

Most studies on CNS viral infection in mouse models use an intracranial route of injection which bypasses potential antiviral mechanisms located at the CNS borders (Manglani and McGavern, 2017). In the case of LCMV, the intracranial infection model indeed induces a strong replication of the pathogen in the CNS, together with immune infiltration, such as neutrophils and CD8+ T cytotoxic cells (Kang et al., 2011; Kang and McGavern, 2008, 2009; Kim et al., 2009). The virus is not cytopathic, but the immune antiviral response is actually responsible for neuroinflammation, edema and death 6 days after infection, in all infected animals (Kang et al., 2011; Kim et al., 2009). Even if the strong penetrance of the disease makes this model useful to study the mechanisms underlying immunopathology, it does not enable us to study the barriers present in cases of natural infections, such as the meninges. Using a more natural route of infection (hematogenous instead of intracranial), we analyzed for the first time the initial events occurring at the CNS borders, using the acute lymphocytic choriomeningitis model (LCMV Armstrong neurotropic strain 53b, noted LCMV thereafter) and uncovered the role of MM in controlling viral spread.

Results

MM populations coexist and uptake peripheral compounds

We first analyzed the MM populations present at steady state in primate and mouse dural meninges and confirmed the presence of a vast network of MM that can be identified using Ionized calcium binding adaptor molecule 1 (Iba1) or the mannose receptor CD206 (Figure 1A and S1A-D). MM density did not significantly vary over time (Figure S1E) and appeared similar in primates (Figure S1F). Most MM were both CD206+ and Iba1+ (Figure S1G). MM could be subdivided into MHC-II^{+} and MHC-II^{-} populations (noted ‘MHC-II+ MM’ and ‘MHC-II- MM’ thereafter), and the proportion of MHC-II+ MM was high in aged primates (Figure 1B). We developed a panel of antibodies allowing flow cytometric analysis of immune cells in mouse dural meninges (Figure S1H, panel used in the manuscript unless otherwise specified). We also designed an alternative antibody panel based on previous studies (Guilliams et al., 2016) and confirmed that MM expressed high levels of CD206, MerTK and lower levels of CD11c and CD26 compared to cDCs (Figure S1I, J) (Rua et al., 2019; Van

Hove et al., 2019). Kinetic experiments indicated an increase of MHC-I and MHC-II+ MM in mouse dural meninges over time (Figure 1C), which was partially dependent on the presence of T cells at steady-state (Figure S2A-D). To know whether maintenance of MHC-II+ MM in the adult was dependent on blood-derived monocytes, we performed lineage-tracing experiments using Cx3cr1-CreERT2 : R26-LSL-TdTomato mice to label resident cells and Ms4a3-Cre mice to track monocytes. Monocyte-derived cells were enriched in both MM populations over time (Figure S2E-G) (Van Hove et al., 2019). We then compared MM ability to detect compounds injected peripherally. MM could readily pick up dextran injected in the vasculature (Figure 1D and Figure S2H-K), with a slight but significant higher uptake by MHC-II+ MM (Figure 1E). Dextran was uptaken efficiently, especially by MHC-II+ MM in the sutures (Figure 1F). Taken together, these results indicate that MM are organized in a dense network allowing efficient detection of peripheral compounds at the brain surface.

Both MM populations respond to a peripheral microbial product

We next performed single-cell RNA sequencing on total nucleated meningeal cells 24 hours after saline (PBS) or lipopolysaccharide (LPS) intravenous injection (Figure 2A and Figure S3A). MM (cluster 4) changed their transcriptional program after LPS injection (Figure 2A). When subdivided into two clusters, we could detect that MHC-II+ and MHC-II- MM responded to LPS (Figure 2B and Figure S3B-E), and more than two thirds of their transcriptomic changes were specific of each population (Figure 2C-E). Interestingly, the main response of MHC-II+ MM consisted in suppressing several pathways linked with translation and antigen-presentation. The upregulated pathways were linked with chemotaxis and IL1 response (Figure 2F and Supplementary Table 1). In contrast, MHC-II- MM upregulated metabolic processes and downregulated tissue development pathways (Figure 2G and Supplementary Table 2, and Figure S3F-H). We also analyzed putative cell-cell interactions using NicheNet and CellChatDB algorithms, which suggested that MHC-II+ MM established stronger communications with other meningeal cells compared to MHC-II- MM upon LPS challenge (Figure S3I-K).

The proportion of MHC-II+ MM was decreased upon activation (Figure 2H) which was also confirmed in meningeal samples of mice injected with LPS (Figure 2I and Figure S4A-C), SARS-CoV2 (Figure 2J-L) and LCMV (Figure 2M, N and Figure S4D-G). Of note, IL10R and IFNAR signaling did respectively affect MHC-II changes occurring upon LPS and LCMV injections (Figure S4H-K). Overall, these data suggest that MM populations both respond to a peripheral insult: MHC-II+ MM developed putative cell-cell interactions with other meningeal cells, and blocked metabolic pathways.

Peripherally injected LCMV reaches the dural meninges leading to immune cells activation

Following intravenous LCMV injection, dural meninges and brain contained LCMV mRNA, viral proteins and infectious particles (Figure 3A, B, Figure S4L-N). Analysis of dural meninges 6 days after infection showed a significant increase in the number of immune cells (Figure 3C), and MM activation (Figure 3D). Immunohistochemistry showed clusters of meningeal immune cells (Figure 3E, F). This suggests that LCMV could transiently infect the CNS compartment even after a peripheral injection, where it triggered an immune response.

Genetic depletion of MM results in fatal meningitis

To further elucidate the role of MM, we used Cd163-Cre mice (Etzerodt et al., 2019). We first evaluated the recombination efficiency in the CNS using a YFP-reporter mouse. In the dural meninges, a majority of MM were YFP+ (>50% of MHC-II+ MM and >60% of MHC-II- MM, Figure 4A), while the other cell types were less affected by the recombination. Importantly, in the brain, microglia were almost not targeted (<1%), while a majority of parenchymal barrier-associated macrophages (>50%) were YFP+ (Figure 4B). We next investigated the role of MM using a direct depletion strategy. In DT-treated Cd163-Cre : Csf1r-LSL-DTR mice, we achieved depletion of macrophages in the meninges, which was statistically significant for MHC-II+ macrophage populations (Figure 4C), while microglia were not significantly affected (Figure 4D). Following LCMV infection, meningeal inflammatory profile was similar to non-depleted mice (Figure 4E), while the viral load in the brain was significantly increased (Figure 4F), leading to fatal meningitis (Figure 4G). Of note, the viral load in the spleen was also increased in Cd163-Cre : Csf1r-LSL-DTR mice, although to a lesser extent than in the brain (Figure S5A). Further analysis of the dural meninges revealed appearance of infected cells (Figure 4H). This innovative genetic depletion strategy thus indicated a role for non-microglial macrophages in blocking viral spread to the CNS.

IFNs sensing by MM, but not MHC-II-mediated antigen presentation, is required for LCMV control

Deletion of *Stat1* in LysM-derived cells resulted in higher number of CD8+ T cells than controls at day 6 post-infection (Figure 5A) and an increased brain viral load (Figure 5B). Mice did not succumb to the infection (Figure S5B-C). Of note, LysM is not specific to MM (immgen.org) and the spleens of LysM-Cre : $Stat1^{fl/fl}$ mice were also more infected compared to controls (Figure S5D). Numerous clusters of LCMV+ cells and inflammatory cells were seen around blood vessels (Figure 5C) (of note, Ly6C stains both blood vessels and monocytes). Similarly, deletion of *Stat1* in Cd163-derived cells resulted in a strong recruitment of inflammatory cells in the dural meninges and an increased viral load in the brain (Figure 5D-

F), although mice did not succumb to the infection (Figure S5E, F). To more specifically target IFN-I signaling pathway, we used Cd163-Cre : Ifnar$^{fl/fl}$ mice. We checked that MM, but not the negative fraction of meningeal cells, were affected by *Ifnar* deletion (Figure S5G). Intravenous infection of those mice with LCMV resulted in a strong recruitment of inflammatory cells in the dural meninges (Figure 5G), and an increased viral load in the brain (Figure 5H) compared to controls, which was associated with weight loss and fatal meningitis (Figure S5H,I). Of note, the spleens of Cd163-Cre : Ifnar$^{fl/fl}$ mice were also more infected compared to controls, although to a lower extent (Figure S5J). The antiviral function of macrophages did not seem to strictly require antigen presentation to CD8+ T cells or CD4+ T cells, as Cd163-Cre : Csf1r-LSL-DTR mice still had higher CNS viral loads compared to controls upon depletion of CD8+ T cells (Figure S5K-L) or CD4+ T cells (Figure S5M-N) in all mice. Of note, we found that DT seemed less efficient at increasing viral load upon CD8$^+$ T cells and CD4$^+$ T cells depletion (Figure S5K-N) compared to T cells-competent mice (Figure 4F), thus not ruling out potential antigen presentation to T cells. However, MHC-II itself on MM was not required to control LCMV as Cd163-Cre : H2Ab1$^{fl/fl}$ mice did not have higher viral loads than controls (Figure S5O-Q). Moreover, in Cd163-Cre : Csf1r-LSL-DTR mice, no vascular leakage was observed after DT injection (Figure S5R,S). Overall, even though Cd163 is not specific to the CNS compartment, this suggests that macrophages protect the meninges from viral infection through IFNAR signaling, and that this protection does not strictly depend on antigen presentation or vascular functions.

Pharmacological depletion of MM results in fatal meningitis

To more locally target macrophages in the meninges, we developed an innovative transcranial delivery approach to deliver CSF1R antagonist (PLX3397) in the meninges. Titration of the drug allowed depletion of MM (Figure 6A-C and Figure S6A). Although flow cytometric analysis showed that parenchymal non-microglial macrophages were not affected (Figure 6D), a more detailed analysis of the brain surface revealed a decrease of pial macrophage density (Figure 6E). Importantly, microglia, blood and spleen myeloid cells were not affected by the treatment (Figure 6F-H). Strikingly, in the absence of MM (Figure 6I), LCMV viral load was specifically increased in the brain, but not the spleen, of infected mice (Figure 6J) which led to fatal meningitis in ~1/3 of the mice (Figure 6K). Some areas of the dural meninges became massively infected following intravenous LCMV injection after PLX3397 treatment (Figure 6L). Of note, similar results were obtained using PLX5622 (Figure S6B-I). Overall, the results of these depletion studies demonstrate the importance of MM in preventing fatal meningitis.

Low proportion of post-natal MHC-II+ MM correlates with higher viral spread to the CNS

We analyzed three different setups in which MHC-II+ MM proportion was experimentally or naturally low. First, we took advantage of the LPS-induced decrease of MHC-II+ MM (Figure 2H, I and Figure S7A). Twenty-four hours following LPS treatment, LCMV was injected in the vasculature. Six days later, meningeal immune response and viral loads revealed a loss of viral control (Figure 7A and Figure S7B). Second, we compared viral spread in the CNS of 4 months and 1 month-old mice, as younger mice have less MHC-II+ MM (Figure 1C). Viral loads were higher in young mice (Figure 7B) which correlated with higher inflammation in the dural meninges (Figure S7C). Third, we noticed that in LysM-Cre : Csf1r-LSL-DTR mice injected with diphtheria toxin (to deplete macrophages) and with an anti-integrin blockade regimen (to block infiltrating monocytes), MM depletion was followed by macrophage repopulation through local proliferation of MHC-II- MM (Figure S7D-G). Of note, off-target effects were limited (Figure 7C and Figure S7H). The MM landscape was thus reminiscent of neonatal mice and we refer to these mice as 'rejuvenated' mice. Infection with LCMV resulted in a significant increase in brain viral load in rejuvenated mice compared to controls (Figure 7D) with similar inflammation (Figure S7I). Of note, spleen viral loads were also increased in rejuvenated mice (Figure S7J). We then studied the overall antiviral response in the whole dural meninges by RT-qPCR, 2 days post-infection. Interestingly, the antiviral response was blunted in rejuvenated mice, suggesting a role of MM, especially MHC-II+ MM, in CNS protection (Figure 7E). Finally, we investigated the cell-intrinsic antiviral properties of MM, by measuring viral RNA by RT-qPCR in sorted MHC-II+ and MHC-II- MM at day 1 and day 2 after infection. Interestingly, LCMV was detected in both MM populations, but with different kinetics (Figure 7F). MHC-II+ MM contained more viral RNA than MHC-II- cells 24 hours post-infection. However, they quickly cleared viral RNA. On the opposite, MHC-II- MM had higher viral load 48 hours after infection (Figure 7F). Altogether, these results suggest that low levels of MHC-II+ MM correlate with a decreased antiviral state in the meninges after a peripheral infection, and that MHC-II+ MM can intrinsiquely quench viral replication.

Discussion

Recent data suggest that immune responses in the CNS are important players of neurocognition and neuropathology. Most of the studies focusing on brain infections use intracranial injection of the pathogen to achieve sufficient disease penetrance, which by-passes the initial events at the brain borders potentially blocking CNS invasion (Manglani and McGavern, 2017). The CNS is protected by highly vascularized membranes, the dural meninges, that contain at least two main MM populations (neonatal MHC-II- and post-natal MHC-II+), of elusive functions. We show that those populations responded to peripheral stimulation, and that *Stat1* and *Ifnar* in macrophages prevented viral spread to the CNS. The antiviral function of macrophages did not depend on their MHC-II mediated antigen-

presentation. Moreover, using novel pharmacological depletion strategies, we show that MM were crucial in blocking fatal neuroinfection.

MHC-II- MM are prevalent in neonates, and MHC-II+ MM progressively appear over time (Chakarov et al., 2019; Goldmann et al., 2016; Mrdjen et al., 2018; Van Hove et al., 2019). At least two main macrophage populations, MHC-II^{high} and MHC-II^{low}, have been described across tissues in mice, and in humans (Chakarov et al., 2019; Perdiguero and Geissmann, 2016; Wang et al., 2022). The appearance of MHC-II+ MM over time is linked in part with a recruitment of blood-derived cells that occurs under homeostatic conditions, as shown in this study and as previously reported for dural macrophages (Van Hove et al., 2019) and choroid plexus macrophages (Goldmann et al., 2016; Van Hove et al., 2019). Alternatively, as the bone-marrow of the skull has been shown to be a myeloid reservoir, it is possible that monocytes directly seed the dural meninges from the bone-marrow (Cugurra et al., 2021). The increase of MHC-II and MHC-I is coherent with the theory of inflammaging (Franceschi et al., 2018), which associates low level of inflammation upon aging with decline in cognitive functions (Baruch et al., 2014; Dulken et al., 2019). However, our study sheds light on the positive role of MM, including post-natal MHC-II+, in surveying the brain borders.

Upon peripheral challenge, we first noticed a decrease of MHC-II+ MM. This could be linked with (1) MHC-II down-regulation, (2) migration of MHC-II+ cells, (3) death of MHC-II+ MM, or (4) a combination thereof. Cytokines (IL10, IFNs) influenced the ratio of MHC-II+ MM, but further studies using lineage tracing methods should provide a better understanding of the biology of those cells. For instance, down-regulation of MHC-II expression has important regulatory functions (Oh and Shin, 2015), and loss of resident macrophages upon challenge has been described in both lymphoid and non-lymphoid tissues (Barth et al., 1995; Gaya et al., 2015; Ginhoux et al., 2017). In addition, response of both MM populations was distinct. The major transcriptomic changes in the MHC-II+ MM population involved upregulation of IL1 pathway and downregulation of antigen-presentation and metabolic processes. In contrast, the transcriptomic changes of the MHC-II- MM included down-regulation of homeostatic functions linked with tissue nurturing. This suggests that several subpopulations of tissue-resident macrophages coexist, and that the tissue-nurturing, neonatal, MHC-II- MM population is progressively replaced by more inflammatory, anti-microbial macrophages.

We next analyzed the response of this barrier tissue to viral infection using a more natural route of infection than usually performed (hematogenous instead of intracranial). This infection model resulted in a transient and ‘asymptomatic’ infection. LCMV injected in the vasculature infected the dural meninges and the brain parenchyma at low levels before being cleared, and we hypothesized that the absence of pathology was in fact due to an active control of the virus at the CNS borders.

The role of perivascular macrophages in viral and bacterial infections has mainly been assessed using clodronate which is inflammatory and non-specific to resident macrophages (Abtin et al., 2014; Polfliet et al., 2001a; Polfliet et al., 2001b; Steel et al., 2010). Using Cd163-Cre mice, we uncovered the role of non-microglial macrophage populations in controlling neuroinfection.

By which mechanisms do MM control CNS invasion? Outcome of the infection with LCMV has been shown to depend on several antiviral pathways, including IFN-response through *Stat1* pathway (Jung et al., 2020). Our data indicate that MM also use this pathway, and act as an amplifier to block further infection. Moreover, *Ifnar* deletion in macrophages is enough to drive a pathological outcome, suggesting that among IFNs, IFN-I are key regulators of MM antiviral functions. Whether *Stat1* and *Ifnar* play a role in MHC-II+ or MHC-II- MM is unknown due to the lack of genetic tools to perform conditional ablation in those populations. Of note, in the Cd163-Cre:Csf1r-LSL-DTR model, DT treatment seemed less efficient at increasing viral load upon T cells depletion compared to T cells-competent mice. Thus, we cannot rule out an additional role of antigen presentation, as CD8+ T cells are known to control LCMV viral load (Kang and McGavern, 2008). The Cd163-Cre mice however allowed us to rule out the role of MHC-II mediated antigen presentation, which does not seem to be required for MM antiviral functions.

PLX treatment (using PLX3397 or PLX5622) has been useful to deplete body macrophages, including microglia. Using a transcranial drug-delivery approach, we were able to deplete barrier macrophages more specifically. This resulted in the death of LCMV-infected mice. Because macrophages in the pial meninges were also affected by the PLX treatment, it will be important to generate new tools to be able to dissect the role of dural versus pial macrophages, and within dural macrophages, to dissect the role of CD206+ (mostly studied in this manuscript) and CD206- macrophages (minor population).

The role of MHC-II+ versus MHC-II- tissue-resident macrophages is still controversial (Chakarov et al., 2019). Using different models, we show that a lower proportion of MHC-II+ MM was associated with higher viral loads. Our data also suggest that MHC-II+ MM could quickly promote a broad antiviral state in the dural meninges, and could quench viral replication. As MHC-II+ MM appear after the neonatal period, this study should also set the ground for understanding the high susceptibility of neonates to CNS infection (de Vries, 2019; Kim, 2010; Sahu et al., 2009). Of note, it is counter-intuitive that even though MHC-II+ MM seem important to control viral load, MHC-II labelling of MM was decreased acutely upon infection. We hypothesize that this could be due to 2 distinct functions of MM: (1) MHC-II-independent (e.g. antimicrobial role in the acute phase, as described here) and (2) MHC-II-dependent (e.g. regulatory role in the repair phase). Those functions would thus need to be temporally and sequentially regulated. As acute antimicrobial functions do not require MHC-II

expression, a decrease of MHC-II on MM could allow redirection of CD4+ T cells to inflammatory monocytes or macrophages and DC that infiltrate the tissue and are more efficient at presenting antigens during neuroinflammation, as shown in the context of EAE (Jordao et al., 2019). Then, in the post-inflammatory phase, restauration of MHC-II levels on MM could help return to homeostasis by interacting with Treg for instance (Chaudhry et al., 2011; Nobs and Kopf, 2021).

Overall, our study unraveled the key role of MM in protecting the brain borders. IFNs allowed MM to counteract viral spread to the CNS and MM depletion resulted in fatal meningitis. This unraveled key cellular pillars of neuroinvasion that have been elusive for decades. The data that we obtained did not only increase our understanding of the role of immune sentinels in neuroinvasion but could also provide a rationale for targeting innate immune meningeal sentinels in the clinic.

Limitations of the study

Although we found that sensing of IFNs was required for MM antiviral functions, it will be important to elucidate the exact molecular mechanisms by which MM provide such a broad meningeal protection. As meningeal macrophages contain different populations, further studies will be needed to determine if there is a division of labor between MHC-II+ and MHC-II- MM, with a population being more antimicrobial, and another more tissue-nurturing, for instance. Finally, we evaluated the role of MM in antiviral responses against LCMV, but it remains unknown if MM also protect the brain against other viruses, bacteria, fungi and parasites, in mice but also in humans.

STAR Methods

Key resources table attached

Resource availability

Lead contact

Further information and requests for resources and reagents should be directed to and will be fulfilled by the lead contact, Rejane Rua (rua@ciml.univ-mrs.fr)

Materials availability

This study did not generate new unique reagents.

Data and code availability

All since-cell RNA-sequencing data were deposited in the Gene Expression Omnibus public database as superseries under GSE189887. Microscopy, RT-qPCR and flow cytometry data reported in this paper will be shared by the lead contact upon request.
All codes and data are available on Github and Zenodo. In-house-made code, original data, and corresponding docker images are available from the project github repository (https://github.com/mteleman/LCMV_paper_RRLab_PBS_LPS_single_cell) both with a readme explaining the detailed procedure to reproduce the results.
Any additional information required to reanalyze the data reported in this paper is available from the lead contact upon request.

Experimental model and subject details

Mice. C57BL/6J (B6), B6.129P2(Cg)-Cx3cr1$^{tm2.1(Cre/ERT2)Litt/WganJ}$ (Cx3cr1-CreERT2), B6.129P2-Lyz2$^{tm1(cre)Ifo/J}$ (LysM-Cre), B6.Cg-Gt(ROSA)26Sor$^{tm14(CAG-tdTomato)Hze/J}$ (R26- LSL-TdTomato), B6.129X1-Gt(ROSA)26Sor$^{tm1(EYFP)Cos/J}$ (R26-LSL-YFP), Tg(Csf1r-HBEGF) (Cs1fr-LSL-DTR) and heterozygous K18-hACE2 (2B6.Cg-Tg(K18-ACE2)2Prlmn/J), H2-Ab1$^{fl/fl}$ (B6.129X1-H2-Ab1tm1Koni/J) mice were obtained from The Jackson Laboratory. Cd3e$^{\Delta 5/\Delta 5}$ mice (noted CD3$^{-/-}$) were provided by B. Malissen (Malissen et al., 1995). Ms4a3-Cre mice were provided by F. Ginhoux (Liu et al., 2019). B6 D^{b}GP$_{33–41}$ TCR-tg (P14), and actin-OFP were bred and maintained at the National Institutes of Health (NIH). Ifnar1^{tm1Uka} (Ifnar$^{fl/fl}$) (Kamphuis et al., 2006; Le Bon et al., 2006), C57BL/6-Stat1$^{tm1c(EUCOMM)Wtsi}$ (Stat1$^{fl/fl}$) (Tomasello et al., 2018) and Cd163-Cre mice (Etzerodt et al., 2019) were maintained in our facility. Cd163-Cre : R26-LSL-YFP, CD163-Cre : Csf1r-LSL-DTR, Cd163-Cre : Stat1$^{fl/fl}$, Cd163-Cre : Ifnar$^{fl/fl}$, LysM-Cre : Stat1$^{fl/fl}$, LysM-Cre : Csf1r-LSL-DTR, Cx3cr1-CreERT2: R26-LSL-TdTomato, Ms4a3-Cre : R26-LSL-TdTom and littermate controls (noted ‘control’ thereafter) were obtained in the F1 and F2 generations by originally crossing the aforementioned homozygous mouse lines. P14 OFP^{+} were derived from the F1 cross: actin-OFP x P14. Male and female mice in this study were used at 6–8 weeks of age unless otherwise specified. All animals used were sex- and age-matched. Unless otherwise specified, all mice were then bred and maintained under specific pathogen free conditions at Centre d’Immunologie de Marseille-Luminy (CIML), with water and food ad libitum and 12h/12h night/daylight cycle. All animal experiments were approved and performed in accordance with the limiting principles for using animal in testing (the three Rs: replacement, reduction, and refinement) and approved by the French Ministry of Higher Education and Research or in accordance with the guidelines set forth by the NIH Animal Care and Use Committee. Animal experiments were done in accordance with institutional animal care and ethical committees and French and European guidelines for

animal care under approval APAFIS#26484-2020062213431976 v6 (experiments involving SARS-CoV2) and APAFIS#20225-2019041017282751 v4 (other experiments).

Baboons. Adult baboons were maintained at the local primate center (Rousset, France) which harvested and provided the tissues.

Method details

LCMV. LCMV Arm53b stocks were prepared as previously mentioned (Rua et al., 2019). Adult mice at 6 to 8 weeks of age were infected intravenously with 1×10^7 plaque forming units (PFU) of LCMV Armstrong clone 53b. Survival following infection was monitored.

SARS-CoV2 Virus Vero E6 (CRL-1586; American Type Culture Collection) were cultured at 37°C in Dulbecco's modified Eagle's medium (DMEM) supplemented with 10% fetal bovine serum (FBS), 10 mM HEPES (pH 7.3), 1 mM sodium pyruvate, 1 X non-essential amino acids and 100 U/ml penicillin–streptomycin. The BetaCoV/France/IDF0372/2020 strain was supplied by the National Reference Centre for Respiratory Viruses hosted by Institut Pasteur (Paris, France) and headed by Pr. Sylvie van der Werf. The human sample from which strain BetaCoV/France/IDF0372/2020 was isolated has been provided by Dr. X. Lescure and Pr. Y. Yazdanpanah from the Bichat Hospital, Paris, France. Moreover, the strain BetaCoV/France/IDF0372/2020 was supplied through the European Virus Archive goesGlobal (Evag) platform, a project that has received funding from the European Union's Horizon 2020 research and innovation program under grant agreement No 653316. Infectious stocks were grown by inoculating Vero E6 cells and collecting supernatant upon observation of cytopathic effect; debris were removed by centrifugation and passage through a 0.22-µm filter. Supernatant was then aliquoted and stored at -80°C. 8–12-week-old female K18-hACE2 mice (noted Tg-K18) were intranasally inoculated with $1.1x10^5$ TCID50 (50% of Tissues Culture Infective Dose) of SARS-CoV-2 (strain BetaCoV/France/IDF0372/2020) or saline injection solution (PBS). Mice were harvested at 2, 3, 4, 5, 6 and 7 days post-infection. In addition, one control group of K18-hACE2 non-carrier animals ('NC') was intranasally inoculated with of SARS-CoV-2 and one control group of K18-hACe2 animals was injected with PBS. SARS-CoV2 virus inoculations were performed under anesthesia that was induced and maintained with ketamine hydrochloride and xylazine, and all efforts were made to minimize animal suffering.

Biosafety Work with LCMV was performed in the biosafety level 3 laboratory (BSL3) of CIML by authorized, trained personnel. Work with SARS-CoV-2 was performed in the BSL3 of

Center for Immunophenomics (CIPHE) by personnel equipped with powered air-purifying respirators. All the CIPHE BSL3 facility operations are overseen by a Biosecurity Officer and accredited by Agence Nationale de Sécurité du Médicament (ANSM).

Meningeal whole mount immunohistochemistry of mouse dural meninges. Mice were euthanized with overdose of ketamine-xylazine anesthetic and perfused with phosphate buffered saline (PBS) for subsequent antibody staining. Skull caps were removed, and following a brief wash in PBS, dural meninges were incubated at room temperature for 15 min in 1.5 mL of blocking solution containing mouse IgG (0.5 mg/mL, Jackson Research) and Fc Block CD16/32 (24G2 supernatant purified from tissue culture supernatant, 1/100). The dural meninges were subsequently stained with coupled primary antibodies at room temperature for 1 h. The following coupled antibodies were used at a concentration of 2.5 µg/mL unless otherwise specified and were obtained from BioLegend: Brilliant Violet 421 anti-mouse IA^b/IE^b (1.25 µg/mL; clone M5/114.15.2), Alexa Fluor 488 and Alexa Fluor 647 anti-mouse Ly6C (clone HK1.4), Alexa Fluor 488 and Alexa Fluor 647 anti-mouse CD206 (clone C068C2), FITC anti-mouse CD11b (clone M1/70), PE anti-mouse CD31 (clone 390), PE anti-mouse CD8a (clone 53-6.7). All antibodies were diluted in PBS + 2% FBS, referred to as 'staining buffer'. Dural meninges were then washed three times in staining buffer for 30 seconds (30 s) and fixed overnight at 4°C in 5% formalin (Sigma). The following day the dural meninges were carefully removed from the skull caps with fine-tipped forceps. The dural meninges were placed in mounting medium (FluorSave Reagent with or without DAPI; Vectashield) on a glass slide (Superfrost Plus; ThermoScientific), spread out and flattened with forceps, and cover-slipped. For uncoupled primary antibody staining, the dural meninges were incubated at 4°C overnight in formalin 5%. The next day, the following primary antibodies were used at a concentration of 2.0 µg/mL: goat anti-mouse IBA1 (Novus Biologicals), rabbit anti-mouse IBA1 (Fujifilm-Wako), chicken anti-mouse NF-H (Abcam) in staining buffer with Triton-X100 (Sigma) at 0.5%, overnight at 4°C. The third day, the dural meninges were washed three times in staining buffer for 30 s and stained with secondary antibodies. The following secondary antibodies were used at a concentration of 2.0 µg/mL: donkey anti-rabbit IgG Alexa Fluor 647 (clone Poly4064, BioLegend), donkey anti-goat IgG Alexa Fluor Plus 488 (Thermofischer). All secondary antibodies were diluted in staining buffer and secondary stainings were performed at room temperature for 2 h. For LCMV staining, dural meninges were briefly fixed in 5% formalin during 10 min at room temperature, to facilitate LCMV detection. This was followed by intracellular staining in staining buffer supplemented with 0.5% Triton-X100 overnight at 4°C, of Alexa Fluor 647 rat anti-LCMV (2.5 µg/mL; clone VL-4; BioXCell). Anti-LCMV monoclonal antibody was directly conjugated to Alexa Fluor 647 using a Mix-N-Stain CF647 antibody-labeling kit (Sigma) according to manufacturer's instructions. Alternatively, purified rat anti-LCMV (2.0 µg/mL;

clone VL-4; BioXCell) was used overnight at 4°C, and followed by aforementioned washes and secondary stains. For EdU staining, 1 mg of EdU was injected 1hour prior to sacrifice, and EdU was revealed following the manufacturer's instructions (Click-iT EdU, Thermofischer).

Meningeal whole mount immunohistochemistry of baboon dural meninges. Baboon dural meninges were fixed in 4% paraformaldehyde (Sigma) for 24 h. The following primary antibodies were used for staining: chicken anti-human IBA1 (1.25 µg/mL, Synaptic Systems) and mouse IgG2a anti-human HLA-DR (1.25 µg/mL; L243, BioLegend) for 48 h at 4°C in staining buffer supplemented with 0.5% Triton X-100. After three 5 min washes, dural meninges were incubated for 24 h at 4°C with secondary antibodies. Following three 5 min washes, dural meninges were incubated in clearing medium (Histodenz, Sigma) for 48 h at 4°C.

Pia mater immunohistochemistry. Brain samples were fixed in a solution of formalin 5% during 10 min on ice and incubated in a staining solution containing staining buffer supplemented with 0.5% Triton X-100 and staining was then performed as for meningeal whole mounts.

Brain immunohistochemistry. Brains were fixed in formalin 5% overnight at 4°C. The next day, samples were washed with PBS before dehydration in a solution of 30% sucrose overnight at 4°C. For inclusion, each brain was individually placed in a clear base mold (37x24x5 mm, Leica), covered with OCT Embedding Medium (Thermofischer) and frozen using isopenthane. Brain slices were cut with a cryostat at a thickness of 25 µm and stained with antibodies in staining buffer supplemented with 0.5% Triton-X100, with similar steps as indicated for meningeal whole mounts.

Imaging acquisition. Fluorescent images were acquired using a Zeiss LSM780 x 2 laser scanning confocal microscope (Carl Zeiss Microscopy) equipped with 405, 488, 561, and 635 nm laser lines, 4 side window PMTs for simultaneous 4 channel acquisition, and a 10X objective (or 20X for zooms). 3D tile scans encompassing the entire meninges were collected (*z* depth = 400 µm, *z* step size = 20 µm for meninges, and 10 µm for brain sections).

Imaging analysis. After collecting tile scans by confocal microscopy, entire meningeal whole mounts or specific anatomical regions within the meninges (e.g. lobe, suture) were analyzed using Imaris 9.6.0 software. The Surface Creation Wizard was used to identify positively stained cells within the maximal intensity projections of meningeal tile scans. Once identified, a value-based visual surface was generated for all positively stained cells, which enabled

quantification of fluorescence intensity as well as the frequency of labeled and unlabeled cells. Channel statistics for MHC-II or dextran were obtained for cellular surfaces defined based on CD206. For the clustering approach, the Surface Creation Wizard of Imaris 9.6.0 software was also used to quantify cell clusters quantities and total meningeal area, using adequate object size parameter.

Histocytometry. Channel statistics for MHC-II, dextran, CD206 and IBA1 previously obtained, were exported into Excel (Microsoft), and mean voxel fluorescence was plotted in FlowJo software by utilizing the Text to FCS conversion utility (TreeStar Inc). Percentages of surfaces either positive or negative for MHC-II or dextran were gated using traditional log-scale based flow cytometry plots in FlowJo and then graphed on linear XY plots to map their respective positions within the meninges.

Mononuclear cell isolation. Anesthetized mice received an intracardiac perfusion with PBS to remove contaminating blood cells. Dural meninges were isolated using forceps to gently separate them from the underside of the skull cap (the same method used to prepare meningeal whole mounts above). For the brains and the spleens, organs were recovered and cut in small pieces. This was followed by enzymatic digestion in RPMI containing 2.5 mg/mL collagenase D (Roche) + 0.1 mg/mL DNase (Roche) for 30 min at 37°C with gentle shaking every 10 min, for all three organs. Following digestion, cellular suspensions were passed through a 35-µm pore cell strainer (meninges) or 70-µm pore cell strainer (brains and spleens). After this step, meningeal cells were used for staining. Cells from the brain, however, were resuspended in 40% Percoll (GE Healthcare) gradient and centrifuged to remove myelin and debris from the preparation. Afterwards, brain leukocytes were stained comparably to meningeal cells. Spleen leukocytes were treated with RBC 1X lysis buffer (Thermofischer) to eliminate red blood cells, then washed and 1:20 of total cells were isolated for cell staining.

Blood cell isolation. Blood samples were collected by retro-orbital bleeding using capillary tubes (Microhematocrit Tubes, Thermofischer) and placed in 1 mL PBS. Red blood cells were lysed with RBC 1X lysis buffer and samples were washed twice with staining buffer before antibody staining.

Flow cytometry. Surface staining was performed by incubating cell suspensions for 30 min on ice with cocktails of monoclonal antibodies in staining buffer. Prior to staining, cell preparations were blocked with 5 µg/mL rat anti–mouse CD16/32 (Fc receptor block; BDBiosciences) and 0.5 mg/mL whole mouse IgG (Jackson ImmunoResearch Laboratories, Inc.) for 10 min on ice to reduce unspecific antibody binding. Dead cells were excluded from

the analysis by using the LiveDead fixable Blue Cell Staining kit (Invitrogen). The following rat or mouse anti-mouse antibodies were obtained from BioLegend (BL), BDBiosciences (BD) or ThermoFisher (T) and were used at a concentration of 0.5 µg/mL unless otherwise specified: CD45.2 BUV737 (clone 104, BD), CD11b Brilliant Violet 570 (clone M1/70, BL), CD90.2 (Thy1.2) BUV395 (clone 30-H12, BD), Ly6G Brilliant Violet 711 (clone RA3–6B2, BL), CD206 Alexa Fluor 488 (1.25 µg/mL; clone C068C2, BL), CD206 PE-Cy7 (1.25 µg/mL; clone C068C2, BL), IAb/IEb Brilliant Violet 421 (clone M5/114.15.2, BL), H-2Db H-2Kb PE (clone 28–8-6, BL), Ly6C PE-CF594 (clone AL-21, BD), CD8a Alexa Fluor 700 (clone SK1, BL), CD4 Brilliant Violet 786 (clone RM4.5, BD), NK1.1 APC (clone S17016D, BL), CD64 Brilliant Violet 605 (clone X54–5/7.1, BL), CD11c PE-Cyanine5.5 (clone N418, T) and CD115 Alexa Fluor 647 (2.5 µg/mL, clone AFS98, BL), CD24 BV650 (clone M1/69, BD), CD26 PE (clone H194-112, BL), XCR1 BV510 (clone ZET, BL), F4/80 APC7 (clone BM8, BL), MerTK Alexa Fluor 700 (clone DS5MMER, T), CD172a FITC (clone P84, BD), CD68 PE (clone FA-11, BL), CD55 Alexa Fluor 647 (clone DAF, BL), CD38 PE (clone 90, BL), BST2 BV785 (clone RU0, BL). For intracellular staining to detect LCMV, single cell suspensions were first stained with surface antibodies and were then treated with Cytofix/Cytoperm (BD). This was followed by intracellular staining anti–LCMV (VL-4; Bio X Cell). Anti-LCMV mAb was directly conjugated to Alexa Fluor 647 using an antibody-labeling kit from Invitrogen. Samples were acquired using BD FACSymphony™ A5 Cell Analyzer or an Aurora CellSorter (Cytek), and data were analyzed using FlowJo software version 10.5.3. For flow analyses, unless otherwise specified, meningeal cells were gated as follows : neutrophils : LiveDead$^-$ CD45$^+$ CD11b$^+$ Thy1.2$^-$ Ly6C$^-$ Ly6G$^+$ cells; monocytes : LiveDead$^-$ CD45$^+$ CD11b$^+$ Thy1.2$^-$ Ly6C$^+$ Ly6G$^-$ cells, with MHC-II subsets; MM : LiveDead$^-$ CD45$^+$ CD11b$^+$ Thy1.2$^-$ Ly6C$^-$ Ly6G$^-$ CD11c$^-$ CD64$^+$ CD206$^+$ cells, with MHC-II subsets; other macrophages : LiveDead$^-$ CD45$^+$ CD11b$^+$ Thy1.2$^-$ Ly6C$^-$ Ly6G$^-$ CD11c$^-$ CD64$^+$ CD206$^-$ cells, with MHC-II subsets; CD11b$^+$ DC : LiveDead$^-$ CD45$^+$ CD11b$^+$ Thy1.2$^-$ Ly6C$^-$ Ly6G$^-$ CD11c$^+$ CD64$^-$ MHC-II$^+$ cells; CD11b$^-$ DC : LiveDead$^-$ CD45$^+$ CD11b$^-$ Thy1.2$^-$ CD11c$^+$ CD64$^-$ MHC-II$^+$ cells; CD8$^+$ T cells : LiveDead$^-$ CD45$^+$ CD11b$^-$ Thy1.2$^+$ CD8$^+$ cells; CD4$^+$ T cells : LiveDead$^-$ CD45$^+$ CD11b$^-$ Thy1.2$^+$ CD4$^+$ cells; NK cells : LiveDead$^-$ CD45$^+$ NK1.1$^+$ Thy1.2$^-$ cells; NKT/ILC1 cells : LiveDead$^-$ CD45$^+$ CD11b$^-$ Thy1.2$^+$ NK1.1$^+$ cells; other T cells/ILC : LiveDead$^-$ CD45$^+$ CD11b$^-$ Thy1.2$^+$ CD4$^-$ CD8$^-$ NK1.1$^-$ cells and CD45neg cells : LiveDead$^-$ CD45$^-$ cells. For brain cells, gating was done for microglia on LiveDead$^-$ CD45^{int} CD11b$^+$ Thy1.2$^-$ Ly6C$^-$ Ly6G$^-$ CD11c$^-$ CD206$^-$ cells; for brain macrophages on LiveDead$^-$ CD45$^+$ CD11b$^+$ Thy1.2$^-$ Ly6C$^-$ Ly6G$^-$ CD11c$^-$ CD64$^+$ CD206$^+$ cells, with MHC-II subsets and for neutrophils, monocytes, CD11b$^+$, CD11b$^-$ DC, CD8$^+$ T cells, CD4$^+$ T cells, NK cells, NKT cells, other T cells/ILC and CD45neg cells : identical to meningeal gating. Spleen neutrophils

were gated on LiveDead$^-$ CD45$^+$ Thy1.2$^-$ CD11b$^+$ Ly6C$^-$ Ly6G$^+$ cells, monocytes on LiveDead$^-$ CD45$^+$ CD11b$^+$ Thy1.2$^-$ Ly6C$^+$ Ly6G$^-$ cells and macrophages on LiveDead$^-$ CD45$^+$ CD11b$^+$ Thy1.2$^-$ Ly6C$^-$ Ly6G$^-$ CD64$^+$ cells. Blood neutrophils were gated on LiveDead$^-$ CD45$^+$ Thy1.2$^-$ CD11b$^+$ Ly6C$^-$ Ly6G$^+$ cells and monocytes on LiveDead$^-$ CD45$^+$ CD11b$^+$ Thy1.2$^-$ CD115$^+$ Ly6C$^+$ Ly6G$^-$ cells.

In vitro quantification of LCMV by flow cytometry. Brain and meningeal samples were homogenized in 300 µl and 1 ml of MEM respectively and centrifuged at 480g for 5 min at 4 °C. Then, 25 µl of supernatant was used to infect Vero cells in 250 µl MEM 7% FBS (culture medium). After 1 hour incubation at 37 °C, the medium was replaced by fresh culture medium and after 48 h, Vero cells were analyzed for LCMV infection using flow cytometry, as described in the Flow cytometry section.

In vitro quantification of LCMV by plaque assay. Brain and meningeal samples were homogenized in 300 µl and 1 ml of MEM respectively and centrifuged at 480g for 5 min at 4 °C. Then, 10 µl (meninges) or 100 µl (brains) of supernatant were used for plaque assay titration on Vero cells. Six days later, PFU were quantified by immunofluorescence using intracellular LCMV staining.

Cell sorting. MM were isolated from PBS or LCMV-infected mice at day 1 and day 2 post-infection using a Melody Cell Sorter (BDBiosciences) equipped with an integrated BSL-2 enclosure. Meningeal cells were extracted and stained as described in the Mononuclear cell isolation and Flow cytometry sections above. Two different cell populations (MHC-II+ MM and MHC-II- MM for LCMV quantification; or MM fraction versus MM-negative fraction for *Ifnar* exon deletion measurement) were sorted to >95% purity.

Adoptive transfers. Mice were seeded i.v. with 10^4 OFP$^+$ P14 CD8$^+$ T cells in PBS purified from the splenocytes of naive transgenic mice using a CD8 negative selection kit (Stem Cell Technologies). The purity after enrichment was determined to be greater than 98%. Mice were infected one day later.

PLX3397 and PLX5622 administration. Mice were injected transcranially under the scalp with 2 mg of Pexidartinib (PLX3397, DC Chemicals, China) or 2mg of PLX5622 (DC Chemicals, China), dissolved in 20 µL of dimethyl sulfoxide (Sigma Aldrich) and 180 µL of Corn oil (delivery vehicle for fat soluble, Sigma Aldrich). The control is composed equally but does not contain PLX.

LPS and Dextran injections. 100 µl of LPS (InVivogen, 0.1 mg/mL) or Dextran-Rhodamine B isothiocyanate (70 kDa; Sigma Aldrich, 10 mg/mL) were injected intravenously via the retro-orbital vein, and analyzed or manipulated 24 hours (LPS) or 1 hour (Dextran) later.

Evans blue injection. To analyze vascular leakage, 200 µl of Evans Blue (Sigma, 10 mg/mL) was injected intraperitoneally for 1 hour, before sacrifice.

CD8+ T and CD4+ T cell depletion

CD8+ T and CD4+ T cells were depleted by injecting 0.25 mg of CD8-depleting antibody (clone YTS 169.4, BioXCell) or CD4-depleting antibody (clone GK1.5, BioXCell) intravenously at day 3 and day 5 post-infection.

IL10R-blocking

Mice were injected with 125 µg of IL10R blocking antibody (clone 1B1.3A, BioXCell) both intravenously and transcranially 4 hours before PBS, LPS or LCMV injection. Controls were similarly injected with 125 µg of rat IgG1 isotype control (clone HRPN, BioXcell).

DT administration and rejuvenation treatment. A solution of 100 µl containing 0.1 µg of diphteria toxin ('DT'; Sigma) in carboxymethylcellulose (12 mg/mL; Sigma) was injected transcranially under the scalp of mice. DT was injected on two consecutive days before infection or sacrifice. For 'rejuvenation' experiments, LysM-Cre : Csf1r-LSL-DTR mice and controls were injected with 0.1 µg of DT (Sigma) at day 0 and day 1 to deplete MM. Then, mice were injected intravenously at day 2 and 3 with 250 µg of anti-LFA-1 (clone M17/4, BioXcell) and 250 µg anti-VLA-4 (clone PS/2, BioXcell) to block immune infiltration and promote local repopulation. Mice were then infected with LCMV at day 8, and analyzed 2 days later (whole meningeal qPCR antiviral genes plate) and 6 days later (meningeal immune flow and parenchymal LCMV RT-qPCR).

Tamoxifen administration. For induction of Cre recombinase, 6- to 8-week-old Cx3cr1-CreERT2 : R26-LSL-TdTomato mice received daily intraperitoneal injections (for 5 days) of 2 mg Tamoxifen (Cayman Chemicals) dissolved in 100 µL corn oil (Sigma Aldrich).

Isolation of nucleated meningeal cells and scRNA-sequencing using 10X Genomics platform. Single-cell RNA sequencing was performed on 4 meningeal samples (from 2 mice injected with PBS and 2 with LPS) using 10X genomics and data was analyzed using Seurat software in combination with public datasets (http://brainimmuneatlas.org). Meningeal cells

were extracted as described in the Mononuclear cell isolation and Flow cytometry sections above and stained with Hoechst 33342 (10 µg/mL, Sigma) and Draq7 (0.3 µM, ThermoFischer). The 4 samples were differentially labelled using 4 Hashtags (TotalSeq-A, clone M1/42; 30-F11, BioLegend) at 0.1 mg/mL for 15 min at 4°C. After a wash, nucleated cells were isolated from 2 PBS or 2 LPS-injected mice (7 weeks-old males) at day 1 post-injection using a FACS Aria III SORP (BDBiosciences) using a 100 µm nozzle. 52 000 cells of each sample were pooled, centrifuged at 350g for 3 min, and 35 000 cells of the pool were loaded on a Chromium Single Cell Instrument (10x Genomics) to generate single-cell gel beads-in-emulsion (GEM). GEM and scRNA-libraries were prepared using the Single Cell 3'v3 Gel Bead and Library Kit (10X Genomics, No. 1000092) and the Chromium i7 Multiplex kit (10x Genomics, No 120262) according to the manufacturer's instructions. Briefly, GEM reverse-transcription incubation was performed in a 96-deep-well reaction module at 53°C for 45 min, 85°C for 5 min and ending at 4°C. Next, GEMs were broken and complementary DNA (cDNA) was cleaned up with DynaBeads MyOne Silane Beads (Thermo Fisher Scientific, No. 37002D) and SPRIselect Reagent Kit (Beckman Coulter, No. B23317). Full-length, barcoded cDNA was PCR amplified with a 96-deep-well reaction module at 98°C for 3 min, 11 cycles at 98°C for 15 s, 63°C for 20 s and 72°C for 1 min, one cycle at 72°C for 1 min and ending at 4°C. Following cleaning up with the SPRIselect Reagent Kit and enzymatic fragmentation, library construction to generate Illumina-ready sequencing libraries was performed by the addition of R1 (read 1 primer), P5, P7, i7 sample index and R2 (read 2 primer) via end repair, A-tailing, adapter ligation, post-ligation SPRIselect cleanup/size selection and sample index PCR. After generation of the gene expression and HTO libraries, the cDNA content of post-sample index PCR samples was analyzed using the 2100 BioAnalyzer (Agilent) and the samples were sequenced by the TGML platform (TAGC, Marseille). Sequencing libraries (molar ratio 92/8 for gene expression/HTO) were loaded on a NextSeq500 Illumina flow cell High output (75 cycles) with sequencing settings following the recommendations of 10x Genomics (read 1:28 cycles; read 2: 55 cycles; index i7: 8 cycles; index i5: no cycles; 1.8 pM loading concentration).

scRNA-seq analysis. Preprocessing and analysis of data were done through the usage of standard tools and custom R and bash scripts. We notably used R version 4.0.3, Seurat package version 3.2.2 (Stuart et al., 2019), 10x Genomics CellRanger version 4, CITE-seq-count version 1.4.3 (Stoeckius et al., 2018). Docker and Singularity containers were used to ensure the reproducibility of analyses. All codes and data are available on Github and Zenodo.

Pre-processing of 10x 3' datasets. Raw fastq files from gene expression libraries were processed using Cell Ranger software, with alignment on the mm10 reference genome. For each experiment, cells with less than 200 genes detected and genes detected in less than 3

cells were removed. We further excluded bad quality cells expressing less than 1,000 UMI, more than 20% mitochondrial genes or less than 3% ribosomal genes. HTO barcodes for sample demultiplexing after hashing were counted using CITE-seq-count and were normalized for each cell using a centered log ratio (CLR) transformation across cells implemented in the Seurat function NormalizeData. Cells were demultiplexed using Seurat MULTIseqDemux function and barcodes assigned as doublets or negative were excluded from further analysis. The resulting filtered UMI count matrices were log-normalized with Seurat NormalizeData with a scale factor of 10,000.

10x Dataset analysis. Analysis of datasets were performed using custom R scripts. Variable genes (n=2000) were identified with Seurat FindVariableFeatures (vst method). After centering with Seurat ScaleData, principal component analysis was performed on variable genes with Seurat RunPCA, and embedded in two-dimensional UMAP plots with Seurat RunUMAP on 50 principal components. UMAP embeddings colored by sample metadata or clusters were generated by Seurat DimPlot, those colored by single gene expression or module scores were generated by Seurat FeaturePlot or with ggplot2 ggplot. Clustering was performed using the FindNeighbors and FindClusters methods of the Seurat package using 30 number of neighbors for SNN graph build and Leiden clustering method with a sensitivity set to 2.0 within the global data and with a sensitivity set to 0.3 within the MM subset. Subsetting was performed using *subset* function of the Seurat package using the identities of relevant clusters. Marker genes between clusters were identified using the FindAllMarkers method of the Seurat package using the Wilcoxon Rank Sum test on genes expressed at least in 10% of the cells, a logFC threshold of 0.25 and a FDR threshold of 0.001. Heatmap of gene expression along tissue clusters was done performing a mean of the expression of the genes of interest over the clusters, using the heatmap package (version 1.0.12) for the plot. Heatmap of Szymkiewicz–Simpson coefficient were computed using the set of identified marker genes of each cluster and the ggplot2 ggplot function (version 3.3) for the plot. For the 'thresholding method', cells expressing CD206 were selected, and the expression score of MHC-II was obtained with *AddModuleScore* function of the Seurat package based on the expression score of *H2-Ab1, Cd74, H2-Eb1* and *H2-Aa*. The selection of cells depending on the expression score was set with a threshold of 0. Gene Ontology pathways were obtained with clusterProfiler v4.0.0 R package and volcano plots were obtained with EnhancedVolcano v.1.9.13 R package. Pseudo-time analyses were performed with Monocle3 v.1.0.0 R package. More precisely, Seurat's function CellSelector() was used to remove outlier cells. In order to compute the activation trajectory of each MM cluster, we analyzed separately MHC-II- and MHC-II+ MM to avoid interference. Then, the Monocle pipeline was applied on the UMAP computed by Seurat.

RT-qPCR. After perfusion with PBS, meningeal, brain and spleen tissues or FACS-sorted cells were collected in Trizol (Invitrogen) or RLT (supplied by the RNeasy Mini Kit), and total RNA was extracted using RNeasy Mini Kit (Qiagen) per the manufacturer's instructions. Purified RNA was reverse transcribed into cDNA by using an iScript cDNA Synthesis kit (Life Technologies). Real-time qPCR was performed using SYBR® Premix Ex Taq™ (Takara) reactions and cDNA template or water (non-template negative control) with the Applied Biosystems 7500 Real-Time PCR System. Reactions were conducted in duplicates, and PCR products were subjected to melt analysis to confirm purity after DNA amplification. Expression values of LCMV viral load were defined using the following primers: LCMV GP Forward 5'-CAGAAATGTTGATGCTGGACTGC-3', LCMV GP Reverse 5'-CAGACCTTGGCTTGCTTTACACAG-3' and were normalized to *Actb* housekeeping gene (Forward 5'-AGCTCATTGTAGAAGGTGTGG-3', Reverse 5'-GTGGGAATGGGTCAGAAGG-3'). The resulting relative gene expression was then expressed relative to the housekeeping gene or as a fold-change from indicated control samples. Primers were designed and obtained from Integrated DNA Technologies (IDT). For qPCR plates, RNA concentrations were quantified using a Nanodrop, and gDNA was digested using a DNAse I kit (ThermoFisher). cDNA was generated using an iScript cDNA Synthesis kit (Bio-Rad). 96-well custom or pre-made PrimePCR plates (Bio-Rad) were used for qPCR experiments. 10–20 ng of cDNA and SYBR green reagent (Bio-Rad) were added to lyophilized primers in each well and the plate was read on a Bio-Rad CFX96 Real-Time with C1000 Thermal Cycler system. On each PrimePCR plate, there were control wells for RNA quality and gDNA contamination. To detect the deletion of *Ifnar* gene (exon 10) in Cd163-Cre : Ifnar$^{fl/fl}$ mice, RT-qPCR was performed on RNA from sorted cells of the meninges (MM fraction and MM-negative fraction), using primers flanking the exon 10 on the mRNA sequence (forward 5'-AGACCAGCAACTTCAGTGAAA-3' and Reverse 5'-TTGAAGGCGGCTCAGAGA-3'). The melting curve of the amplicon correlates with the size of the full exon (~82°C, 0.2kbp) or the truncated exon (~78°C, 0.07kbp). Products of the RT-qPCR (5µl) were mixed with the ExactLadder DNA Premix (Ozyme) and run on a 2.5% agarose gel electrophoresis (UltraPure agarose, Invitrogen) along with the 1Kb Plus DNA Ladder (Invitrogen).

Statistical analysis. Statistical analyses for experiments containing two datasets were performed using a Student's *t* test (parametric datasets) or a Mann-Whitney rank sum test (non-parametric datasets). Normal distribution was assessed using a Shapiro-Wilk test. Experiments involving more than two datasets were analyzed by ANOVA (parametric datasets) and Kruskall-Wallis (non-parametric datasets) followed by a Holm-Sidak test for multiple comparisons, unless otherwise specified. All statistical analyses were performed in Graphpad Prism 9.1.2 and were considered statistically different at a p-value<0.05. All data are displayed

as the mean ± s.e.m. Technical replicates and iterative measures were averaged per biological unit, so that one symbol represents one individual.

Supplementary Table 1. Pathways differentially regulated in MHC-II+ MM 24 h after i.v. LPS injection (related to Figure 2)

Gene Ontology pathways of DEGs in LPS condition compared to PBS condition in MHC-II+ MM obtained with clusterProfiler R package.

Supplementary Table 2. Pathways differentially regulated in MHC-II- MM 24 h after i.v. LPS injection (related to Figure 2)

Gene Ontology pathways of DEGs in LPS condition compared to PBS condition in MHC-II- MM obtained with clusterProfiler R package.

Acknowledgements

We thank Cathleen Lutz and The Jackson Laboratory for providing K18-hACE2 mice, and Sylvie van der Werf for strain BetaCoV/France/IDF0372/2020. We acknowledge the CIML Flow Cytometry Core (M. Barad and S. Bigot for their technical support), as well as the Imaging, Histology and Genomics Platforms of the CIML for technical assistance and Pierre Golstein (Centre d'Immunologie Marseille-Luminy) for critical advice. These studies were supported by the ATIP-AVENIR young group leader program (INSERM), the Marie Curie reintegration fellowship (EU), the Federation pour la Recherche sur le Cerveau, the Région Sud Provence-Alpes-Côte d'Azur (co-financed by Innate Pharma S.A.), the European Research Council and the AMIDEX (Aix-Marseille Université) grants, as well as by institutional funding from the Institut National de la Santé et de la Recherche Médicale, Centre National de la Recherche Scientifique, and Aix-Marseille-Université as well as Marseille-Immunopole. Microscopy facilities are supported by l'Agence Nationale de la Recherche (grant ANR-10-INBS-04-01 France Bio Imaging). High throughput sequencing was performed at the TGML Platform, supported by grants from Inserm, GIS IBiSA, Aix-Marseille Université, and ANR-10-INBS-0009-10. CIPHE is supported by the Investissement d'Avenir program PHENOMIN (French National Infrastructure for mouse Phenogenomics; ANR-10-INBS-07) and the DCBIOL LabEx (grants ANR-11-LABEX-0043 and ANR-10-IDEX-0001-02 PSL). SARS-CoV2 studies were also supported by the COVIDHUMICE project (Fondation pour la Recherche Médicale-ANR Flash Covid-COVI-0066 to B. Malissen). The authors declare no competing financial interests.

Author contributions

JR and RR designed the experiments. JR, EES and RR performed the experiments with help from LA, CB, KC, EG, SK, and ARQ. AS, QB, PH, AZ and BM performed SAS-CoV2 infections and samples preparation. AZ and BM provided critical feedback. MT and LS performed the bioinformatics analyses. MD provided Ifnar$^{fl/fl}$ and Stat1$^{fl/fl}$ mice. TL provided Cd163-Cre mice. FG and ZL provided Ms4a3-Cre mice. DM provided LCMV virus and P14 mice. MCM, AZ, BM, MD, TL and DM provided critical feedback. JR and RR wrote the manuscript.

Legend

Figure 1. MM populations inhabit mouse and primate dural meninges

A. Maximal intensity projection of a confocal z-stack of dural meninges from an aged baboon (top) and an adult mouse (bottom) with MHC-II stain (red) and IBA1 or CD206 stain (green). Scale bar: 100 µm. Image is representative of 4 baboons and 5 mice.

B. Baboon dural meninges were cleared and stained for IBA1 and MHC-II. The proportion of MHC-II+ MM in baboons is indicated. Graphs show the mean ± s.e.m. Data are representative of 4 baboons and 2 regions per baboon were quantified.

C. At different ages, expression of MHC-II and MHC-I by MM was assessed by flow cytometry on mouse dural meninges. Graphs show the mean ± s.e.m. and asterisks denote statistical significance (*p<0.05; ***p<0.001; Pearson correlation test, with “r” correlation coefficient indicated). Data are representative of 6 independent experiments with 6 mice (d10, d14), 5 mice (d60), 10 mice (d30), 15 mice (d90) and 3 mice (d120, d150, d210) per group for MHC-II assessment, and 6 independent experiments with 3 mice (d14), 5 mice (d60), 10 mice (d30), 15 mice (d90) and 3 mice (d120, d150, d210) per group for MHC-I assessment.

D. Representative maximal intensity projection of meningeal whole mount of B6 mice injected intravenously with 70 kDa fluorescent dextran 60 min prior. The inset shows an area of the parietal lobe, with CD206 (red) and dextran (green). Scale bar: 3 mm (whole meninges) and 200 µm (inset). IL: interparietal-occipital lobe; PL: parietal lobe; FL: frontal lobe; SSS: superior sagittal sinus; TS: transverse sinus. ‘i.v.’= intravenous. Data are representative of 2 independent experiments with 4 mice per group.

E, F. Dextran uptake was quantified using histocytometry. (E) Intensity of dextran fluorescence in MM. Bar graphs show the mean ± s.e.m. for the indicated groups and asterisks denote statistical significance (**p<0.01; Unpaired two-tailed Student’s t test). (F) Dextran uptake by MHC-II+ MM (blue) and MHC-II- MM (orange) subsets was visualized. Data are representative of 2 independent experiments with 4 mice per group.

Figure 2. MHC-II+ MM and MHC-II- MM differentially respond to peripheral stimuli

A. UMAP representation of nucleated meningeal cells (7,035 cells). MM are indicated by the red box.

B. UMAP representation of MM subsets (497 cells). Visualization of *H2-Ab1* expression within MM subsets (right).

C. Venn diagram of differentially expressed genes (DEGs) in LPS versus PBS conditions (adjusted p-value<0.05, abs(log2FC)>0.25) in MHC-II+ MM and MHC-II- MM.

D, E. Volcano plot of DEG in LPS versus PBS conditions in MHC-II+ MM (D) and MHC-II- MM (E) obtained with EnhancedVolcano R package.

F, G. Gene ontology pathways of differentially expressed genes (DEGs) in LPS versus PBS condition in MHC-II+ MM (F) and MHC-II- MM (G) obtained with clusterProfiler R package.

H. Violin plot of the expression of *H2-Ab1* in MM according to the treatment (PBS or LPS), and the proportion of cells positive for *H2-Ab1* is noted.

I. MHC-II+ and MHC-II- MM populations were enumerated by flow cytometry 24 h after LPS or PBS intravenous injection. Bar graphs show the mean ± s.e.m. and asterisk denote statistical significance (ns=not significant; *p<0.05; Kruskall Wallis test followed by Mann-Whitney two-tailed test with Holm-Sidak correction for multiple analysis). Data are representative of 7 independent experiments with 17 mice (PBS) and 16 mice (LPS) per group.

J-L. K18-hACE2 mice (noted Tg-K18) were infected intranasally with $1.1x10^5$ TCID50 of SARS-CoV2 and harvested at day D2, D3, D4, D5, D6 and D7 post-infection. In addition, one control group of K18-hACe2 animals was injected with saline solution ('PBS') and one control group of K18-hACE2 non-carrier animals ('NC') was also infected. (J, K) MM populations' density was calculated based on IBA1 staining at different timepoints after SARS-CoV2 intranasal infection. Bar graphs show the mean ± s.e.m. and asterisks denote statistical significance (ns=not significant; *p<0.05; **p<0.01; Kruskall-Wallis test with Dunn's post-hoc test). (L) MM were identified based on IBA1 staining (green) in Tg-K18 mice, depicting loss of MHC-II expression (red) on MM 6 days after infection with SARS-CoV-2. Data are representative of 3 independent experiments with 6 mice (PBS), 6 mice (NC), 8 mice (SARS-CoV2 D2), 2 mice (SARS-CoV2 D3), 7 mice (SARS-CoV2 D4), 3 mice (SARS-CoV2 D5), 7 mice (SARS-CoV2 D6) and 4 mice (SARS-CoV2 D7) per group, and 2 to 3 regions per mouse were analyzed. Scale bar: 50 µm.

M, N. MM were identified based on CD206 staining, with MHC-II subsets, 48 h after intravenous PBS or LCMV injections. (M) A representative image of histocytometry results in PBS and LCMV conditions is shown. (N) MHC-II+ and MHC-II- MM density was calculated by histocytometry 48 h after PBS or LCMV intravenous injection. Bar graphs show the mean ± s.e.m. and asterisks denote statistical significance (*p<0.05; ***p<0.001; Kruskall Wallis test followed by Mann-Whitney two-tailed test with Holm-Sidak correction for multiple analysis).

Data are representative of 4 independent experiments with 8 mice (PBS) and 9 mice (LCMV) per group.

Figure 3. Infection of LCMV via the intravenous route leads to a transient infection in the dural meninges and the brain

A, B. LCMV mRNA levels were quantified by in the dural meninges (A) and brains (B) at days 1, 6 and 30 post-infection and compared to mock-infected mice. Bar graphs show the mean ± s.e.m. and asterisks denote statistical significance (ns=not significant; **p<0.01; ****p<0.0001; Kruskall-Wallis test with Dunn's post-hoc test). Data are representative of 4 independent experiments with 12 mice (naive) and 6 mice (d1, d6, d30) per group.

C, D. At day 6 post LCMV infection, meningeal infiltrating cells were enumerated. Bar graphs show the mean ± s.e.m. and asterisks denote statistical significance (**p<0.01; ****p<0.0001; One-way ANOVA test followed by unpaired two-tailed Student's *t*-test with Holm-Sidak test for pairwise comparison for C; Unpaired two-tailed Student's *t*-test for D). Data are representative of 2 independent experiments with 7 (PBS) and 8 (LCMV) mice per group.

E, F. B6 mice were injected intravenously with P14-OFP$^+$ CD8$^+$ T cells and with either PBS or LCMV and analyzed at day 6 (D6) post-infection. (E) Immune clusters of MHC-II+ cells were analyzed and quantified in interparietal-occipital, parietal and frontal regions of the dural meninges. Bar graphs show the mean ± s.e.m. for the indicated groups and asterisks denote statistical significance (**p<0.01; Kruskall Wallis test followed by Mann-Whitney two-tailed test with Holm-Sidak correction for multiple analysis). (F) Maximal intensity projections of meningeal whole mounts from B6 mice showing MHC-II (blue), CD11b (green) and P14-OFP$^+$ T cells (red). Scale bar: 1 mm. Magnified area highlighted in the white box is shown on the right. Scale bar: 30 µm. Data are representative of 2 independent experiments with 7 mice per group.

Figure 4. MM genetic depletion increases susceptibility to fatal meningitis

A, B. CNS immune cells of Cd163-Cre : R26-LSL-YFP mice were analyzed by flow cytometry. (A) Bar graphs show the percentage of YFP$^+$ cells. Bar graphs show the mean ± s.e.m. for the indicated groups, and asterisks denote statistical significance (*p<0.05; **p<0.01; ****p<0.0001; Kruskall Wallis test followed by Mann-Whitney two-tailed test with Holm-Sidak correction for multiple analysis). Data are representative of 4 independent experiments with 8 mice (Control) and 17 mice (Cd163-Cre : R26-LSL-YFP) per group. A representative FACS plot of YFP expression in MM of control versus Cd163-Cre : R26-LSL-YFP mice is shown (right). (B) Bar graphs show the percentage of YFP$^+$ cells. Bar graphs show the mean ± s.e.m. for the indicated groups, and asterisks denote statistical significance (ns=not significant; *p<0.05; **p<0.01; ***p<0.001; Kruskall Wallis test followed by Mann-Whitney two-tailed test

with Holm-Sidak correction for multiple analysis). Data are representative of 4 independent experiments with 5 mice (Control) and 17 mice (Cd163-Cre : R26-LSL-YFP) per group. A representative FACS plot of YFP expression in microglia of control versus Cd163-Cre : R26-LSL-YFP mice is shown (right).

C, D. Cd163-Cre : Csf1r-LSL-DTR mice were injected with 100 ng of diphtheria toxin (DT) transcranially on two consecutive days and analyzed by flow cytometry for immune cells in the dural meninges (C) and the brain (D) the following day. (C) Bar graphs show the number of immune cells. Bar graphs show the mean ± s.e.m. for the indicated groups and asterisks denote statistical significance (ns=not significant; *p<0.05; Kruskall Wallis test followed by Mann-Whitney two-tailed test with Holm-Sidak correction for multiple analysis). Data are representative of 3 independent experiments with 7 mice (Control + DT) and 6 mice (Cd163-Cre : Csf1r-LSL-DTR + DT) per group. (D) Bar graphs show the number of immune cells. Bar graphs show the mean ± s.e.m. for the indicated groups (ns=not significant; Kruskall Wallis test followed by Mann-Whitney two-tailed test with Holm-Sidak correction for multiple analysis). Data are representative of 3 independent experiments with 9 mice (Control + DT) and 6 mice (Cd163-Cre : Csf1r-LSL-DTR + DT) per group.

E, F. Cd163-Cre : Csf1r-LSL-DTR mice were subjected to DT injections as previously described, infected with LCMV and analyzed 6 days later. (E) Bar graphs show the number of meningeal immune cells. Bar graphs show the mean ± s.e.m. for the indicated groups (ns=not significant; Kruskall Wallis test followed by Mann-Whitney two-tailed test with Holm-Sidak correction for multiple analysis). Data are representative of 2 independent experiments with 8 mice (Control + DT + LCMV) and 4 mice (Cd163-Cre : Csf1r-LSL-DTR + DT + LCMV) per group. (F) LCMV mRNA levels were quantified in the brains of Cd163-Cre : Csf1r-LSL-DTR mice injected with DT, at day 6 post LCMV infection. Bar graphs show the mean ± s.e.m. and asterisks denote statistical significance (*p<0.05; Mann-Whitney two-tailed test). Data are representative of 2 independent experiments with 4 mice (Control + DT + LCMV) and 5 mice (Cd163-Cre : Csf1r-LSL-DTR + DT + LCMV) per group.

G. Survival curves of Cd163-Cre : Csf1r-LSL-DTR or control mice after infection. Asterisks denote statistical significance (**p<0.01; Log-rank Mantel Cox test). Data are representative of 2 independent experiments with 13 mice (Control + DT + LCMV) and 10 mice (Cd163-Cre : Csf1r-LSL-DTR + DT + LCMV) per group.

H. Maximal intensity projection of meningeal whole mounts from Cd163-Cre : Csf1r-LSL-DTR and controls injected with DT prior to infection, showing LCMV (green) expression at day 3 and day 6 post-infection. Scale bar: 3 mm. Magnified areas highlighted in white boxes are shown in lower panels. Scale bar: 200 µm. Data are representative of 3 independent experiments with 5 mice (PBS D3), 2 mice (WT D3), 2 mice (CD163-Cre : Csf1r-LSL-DTR D3),

7 mice (WT D6) and 8 mice (Cd163-Cre : Csf1r-LSL-DTR D6) per group. D3: day 3 post-infection. D6: day 6 post-infection.

Figure 5. MM antiviral action requires *Stat1* and *Ifnar*

A. At day 6 post-infection, meningeal immune cells of LysM-Cre : Stat1$^{fl/fl}$ mice were analyzed by flow cytometry. Bar graphs show the mean ± s.e.m. and asterisks denote statistical significance (ns=not significant; *p<0.05; ***p<0.001; Kruskall Wallis test followed by Mann-Whitney two-tailed test with Holm-Sidak correction for multiple analysis). Data are representative of 3 independent experiments with 20 mice (Control + LCMV) and 8 mice (LysM-Cre : Stat1$^{fl/fl}$ + LCMV) per group.

B. LCMV mRNA levels were quantified in the brains of LysM-Cre : Stat1$^{fl/fl}$ mice at day 6 post-infection. Bar graphs show the mean ± s.e.m. and asterisks denote statistical significance (****p<0.0001; Mann-Whitney two-tailed test). Data are representative of 4 independent experiments with 18 mice (Control + LCMV) and 9 mice (LysM-Cre : Stat1$^{fl/fl}$ + LCMV) per group.

C. Maximal intensity projection of meningeal whole mounts from LysM-Cre : Stat1$^{fl/fl}$ at day 6 post-infection show numerous clusters of LCMV (green) surrounded by monocytes (red) and MHC-II+ cells (blue) compared to controls. Magnified area of highlighted white box shows viral patches in LysM-Cre : Stat1$^{fl/fl}$ mice. Data are representative of 2 independent experiments with 2 mice per group. Scale bar: 3 mm (full dural meninges) and 200 µm (inset). D6: day 6 post-infection.

D. At day 6 post-infection, meningeal immune cells of Cd163-Cre : Stat1$^{fl/fl}$ mice were analyzed by flow cytometry. Bar graphs show the mean ± s.e.m. and asterisks denote statistical significance (ns=not significant; *p<0.05; **p<0.01; ****p<0.0001; Kruskall Wallis test followed by Mann-Whitney two-tailed test with Holm-Sidak correction for multiple analysis). Data are representative of 6 independent experiments with 25 mice (Control + LCMV) and 15 mice (Cd163-Cre : Stat1$^{fl/fl}$ + LCMV) per group.

E. LCMV mRNA levels were quantified in the brains of Cd163-Cre : Stat1$^{fl/fl}$ mice at day 6 post-infection. Bar graphs show the mean ± s.e.m. and asterisks denote statistical significance (**p<0.01; Mann-Whitney two-tailed test). Data are representative of 7 independent experiments with 21 mice (Control + LCMV) and 15 mice (Cd163-Cre : Stat1$^{fl/fl}$ + LCMV) per group.

F. Maximal intensity projection of meningeal whole mounts from Cd163-Cre : Stat1$^{fl/fl}$ at day 6 post-infection show few clusters of LCMV (green) surrounded by monocytes (red) compared to controls. Data are representative of 3 independent experiments with 6 mice (Control D6) and 7 mice (Cd163-Cre : Stat1$^{fl/fl}$ D6) per group. Magnified area of highlighted white box shows

viral patches in Cd163-Cre : Stat1$^{fl/fl}$ mice. Scale bar: 3 mm (full dural meninges) and 200 µm (inset). D6: day 6 post-infection

G. At day 6 post-infection, meningeal immune cells of Cd163-Cre : Ifnar$^{fl/fl}$ mice were analyzed by flow cytometry. Bar graphs show the mean ± s.e.m. and asterisks denote statistical significance (ns=not significant; *p<0.05; **p<0.01; ***p<0.001; ****p<0.0001; Kruskall Wallis test followed by Mann-Whitney two-tailed test with Holm-Sidak correction for multiple analysis). Data are representative of 2 independent experiments with 12 mice per group.

H. LCMV mRNA levels were quantified in the brains of Cd163-Cre : Ifnar$^{fl/fl}$ mice at day 6 post-infection. Bar graphs show the mean ± s.e.m. and asterisks denote statistical significance (***p<0.001; Mann-Whitney two-tailed test). Data are representative of 2 independent experiments with 12 mice per group.

Figure 6. MM depletion through pharmacological PLX3397 increases susceptibility to fatal meningitis

A. B6 mice were injected transcranially with a CSF1R antagonist (PLX3397) to deplete MM and compared to mock-injected mice. Immune cells were assessed by flow cytometry. Bar graphs show the mean ± s.e.m and asterisks denote statistical significance (ns=not significant; *p<0.05; One-way ANOVA test followed by unpaired two-tailed Student's *t*-test with Holm-Sidak test for pairwise comparison). Data are representative of 2 independent experiments with 5 mice (Mock) and 7 mice (PLX3397) per group. A representative FACS plot of MM among CD11b+ Ly6c- Ly6g- cells, in mock and PLX-treated mice is shown on the right.

B. MM density was assessed on whole mount images. Bar graphs show the mean ± s.e.m and asterisks denote statistical significance (ns=not significant; *p<0.05; **p<0.01; Kruskall Wallis test followed by Mann-Whitney two-tailed test with Holm-Sidak correction for multiple analysis). Data are representative of 3 independent experiments with 7 mice (Mock) and 12 mice (PLX3397) per group.

C. Maximal intensity projection of meningeal whole mounts from PLX3397-treated mice were stained for CD206 (green), Ly6C (blue) and MHC-II (red). Scale bar: 1 mm. The insets show a region of the suture and of the lobe represented by the white box. Scale bar: 100 µm. Data are representative of 3 independent experiments with 7 mice (Mock) and 12 mice (PLX3397) per group.

D. Brain macrophages (perivascular macrophages, choroid plexus macrophages and pial macrophages), were assessed by flow cytometry. Bar graphs show the mean ± s.e.m. (ns=not significant; Mann-Whitney two-tailed test). Data are representative of 2 independent experiments with 10 mice (Mock) and 9 mice (PLX3397) per group.

E. Density of pial macrophages was assessed on brain surfaces stained with CD206 for macrophage quantification in PLX3397- and mock-injected mice. Bar graphs show the mean

± s.e.m. and asterisks denote statistical significance (****p<0.0001; Unpaired two-tailed Student's *t*-test). Data are representative of 2 experiments with 8 mice per group for which 2 lobes per mouse and 2 to 3 regions per lobe were quantified.

F. Microglia were assessed by flow cytometry (left panel). Bar graphs show the mean ± s.e.m. (ns=not significant; Mann-Whitney two-tailed test). Data are representative of 3 independent experiments with 13 mice (Mock) and 12 mice (PLX3397) per group. Maximal intensity projection of brain sections from PLX- and mock-injected mice were stained for IBA1 (green) and DAPI (blue) (middle panel). Scale bar: 100 µm. Microglial density was quantified (right panel). Bar graphs show the mean ± s.e.m. (ns=not significant; Unpaired two-tailed Student's *t*-test). Data are representative of 3 independent experiments with 10 mice per group.

G. Blood neutrophils and monocytes were quantified by flow cytometry. Bar graphs show the mean ± s.e.m. (ns=not significant; Kruskall Wallis test followed by Mann-Whitney two-tailed test with Holm-Sidak correction for multiple analysis). Data are representative of 3 independent experiments with 13 mice (Mock) and 12 mice (PLX3397) per group.

H. Spleen neutrophils, monocytes and macrophages were quantified by flow cytometry. Bar graphs show the mean ± s.e.m (ns=not significant; Kruskall Wallis test followed by Mann-Whitney two-tailed test with Holm-Sidak correction for multiple analysis). Data are representative of 3 independent experiments with 13 mice per group.

I. PLX3397-treated mice were infected with LCMV intravenously. At day 6 post-infection, meningeal neutrophils, monocytes, MM and $CD8^+$ T cells were enumerated. Bar graphs show the mean ± s.e.m and asterisks denote statistical significance (ns=not significant; **p<0.01; ****p<0.0001; Kruskall Wallis test followed by Mann-Whitney two-tailed test with Holm-Sidak correction for multiple analysis). Data are representative of 3 independent experiments with 13 mice per group.

J. LCMV mRNA levels were quantified in the brains (left) and spleens (right) of PLX3397- and mock-injected mice, at day 6 post-infection. Bar graphs show the mean ± s.e.m. and asterisks denote statistical significance (ns=not significant; **p<0.01; Mann-Whitney two-tailed test). Data are representative of 2 independent experiments with 12 mice (Mock, Brain) and 12 mice (PLX3397, Brain) per group and 13 mice (Mock, Spleen) and 13 mice (PLX3397, Spleen) per group.

K. Survival curves of PLX3397- or mock-injected mice after infection with LCMV. Asterisks denote statistical significance (*p<0.05; Log-rank Mantel Cox test). Data are representative of 3 independent experiments with 14 mice (Mock + LCMV) and 19 mice (PLX3397 + LCMV) per group.

L. A representative zoom on whole mount dural meninges showing $Ly6C^+$ vessels (red), $CD8^+$ T cells (blue), and LCMV (green) in naive mice (left), and at day 6 post-infection of mock-injected (middle) and PLX3397-treated mice (right). Scale bar: 100 µm. Data are

representative of two independent experiments with 2 non-infected mice (NI), 4 mice (Mock + LCMV) and 4 mice (PLX3397 + LCMV) per group. D6: day 6 post-infection.

Figure 7. Low levels of MHC-II+ MM are associated with increased neuroinfection

A. Mice were subjected to an injection of lipopolysaccharide (LPS) or saline solution (PBS), 24 h before infection with LCMV. At day 6 post-infection, LCMV mRNA was quantified in brains of mice injected with LPS and compared to controls (PBS), showing significantly higher viral load in LPS-injected mice. Bar graphs show the mean ± s.e.m. and asterisks denote statistical significance (*p<0.05; Mann-Whitney two-tailed test). Data are representative of 2 experiments with 4 mice (PBS + LCMV) and 8 mice (LPS + LCMV) per group.

B. Four months-old (4MO) and one month-old (1MO) B6 mice were injected with LCMV. Bar graphs show the mean ± s.e.m. and asterisks denote statistical significance (*p<0.05; Mann-Whitney two-tailed test). Data are representative of 3 independent experiments with 11 mice per group.

C, D. Mice were subjected to meningeal 'rejuvenation' before infection with LCMV. (C) LysM-Cre : Csf1r-LSL-DTR mice and controls were injected with DT and with blocking antibodies (anti-LFA/VLA) to block MHC-II+ cells infiltration and promote local MHC-II- MM proliferation. MM were analyzed by flow cytometry at day 8 post DT. Bar graphs show mean ± s.e.m and asterisks denote statistical significance (ns=not significant; **p<0.01; One-way ANOVA test followed by unpaired two-tailed Student's *t*-test with Holm-Sidak test for pairwise comparison). Data are representative of 2 independent experiments with 5 mice per group. (D) At day 8 post DT injection, mice were infected with LCMV. At day 6 post-infection, LCMV mRNA was quantified in brains of 'rejuvenated' mice and compared with controls. Bar graphs show the mean ± s.e.m. and asterisks denote statistical significance (***p<0.001; Mann-Whitney two-tailed test). Data are representative of 2 independent experiments with 7 mice per group.

E. Mice were subjected to meningeal 'rejuvenation' before infection with LCMV (as in D). Two days after infection, the whole meningeal tissue was used to assess gene expression by primePCR (SAB antiviral plate). Among the 89 genes tested, the top 20 differentially expressed genes between PBS and LCMV infection were indicated, and their expression was normalized to PBS-injected mice. Data are representative of 2 experiments with 6 (control) and 5 (rejuvenated) mice per group.

F. MHC-II+ and MHC-II- MM (gated on $CD45^+$ $CD11b^+$ $CD64^+$ $CD206^+$ cells) were sorted at 24 h and 48 h post-LCMV infection *in vivo*, and LCMV was quantified in each sample. The proportion of samples positive for LCMV is indicated. Bar graphs show the mean ± s.e.m. and asterisks denote statistical significance (*p<0.05; **p<0.01; Unpaired two-tailed Student's *t*-test). Data are representative of 3 independent experiments, with pools of 4, 7 and 10 mice (24 h) and 5, 5 and 10 mice (48 h).

Declaration of interests

The authors declare no competing interests.

References

Abtin, A., Jain, R., Mitchell, A.J., Roediger, B., Brzoska, A.J., Tikoo, S., Cheng, Q., Ng, L.G., Cavanagh, L.L., von Andrian, U.H.*, et al.* (2014). Perivascular macrophages mediate neutrophil recruitment during bacterial skin infection. Nat Immunol *15*, 45-53.

Banks, W.A. (2016). From blood-brain barrier to blood-brain interface: new opportunities for CNS drug delivery. Nat Rev Drug Discov *15*, 275-292.

Barth, M.W., Hendrzak, J.A., Melnicoff, M.J., and Morahan, P.S. (1995). Review of the macrophage disappearance reaction. J Leukoc Biol *57*, 361-367.

Baruch, K., Deczkowska, A., David, E., Castellano, J.M., Miller, O., Kertser, A., Berkutzki, T., Barnett-Itzhaki, Z., Bezalel, D., Wyss-Coray, T.*, et al.* (2014). Aging. Aging-induced type I interferon response at the choroid plexus negatively affects brain function. Science *346*, 89-93.

Brioschi, S., Wang, W.L., Peng, V., Wang, M., Shchukina, I., Greenberg, Z.J., Bando, J.K., Jaeger, N., Czepielewski, R.S., Swain, A.*, et al.* (2021). Heterogeneity of meningeal B cells reveals a lymphopoietic niche at the CNS borders. Science *373*.

Brynskikh, A., Warren, T., Zhu, J., and Kipnis, J. (2008). Adaptive immunity affects learning behavior in mice. Brain Behav Immun *22*, 861-869.

Chakarov, S., Lim, H.Y., Tan, L., Lim, S.Y., See, P., Lum, J., Zhang, X.M., Foo, S., Nakamizo, S., Duan, K.*, et al.* (2019). Two distinct interstitial macrophage populations coexist across tissues in specific subtissular niches. Science *363*.

Chaudhry, A., Samstein, R.M., Treuting, P., Liang, Y., Pils, M.C., Heinrich, J.M., Jack, R.S., Wunderlich, F.T., Bruning, J.C., Muller, W., and Rudensky, A.Y. (2011). Interleukin-10 signaling in regulatory T cells is required for suppression of Th17 cell-mediated inflammation. Immunity *34*, 566-578.

Cugurra, A., Mamuladze, T., Rustenhoven, J., Dykstra, T., Beroshvili, G., Greenberg, Z.J., Baker, W., Papadopoulos, Z., Drieu, A., Blackburn, S.*, et al.* (2021). Skull and vertebral bone marrow are myeloid cell reservoirs for the meninges and CNS parenchyma. Science *373*.

de Vries, L.S. (2019). Viral Infections and the Neonatal Brain. Semin Pediatr Neurol *32*, 100769.

Dragunow, M. (2013). Meningeal and choroid plexus cells--novel drug targets for CNS disorders. Brain Res *1501*, 32-55.

Dulken, B.W., Buckley, M.T., Navarro Negredo, P., Saligrama, N., Cayrol, R., Leeman, D.S., George, B.M., Boutet, S.C., Hebestreit, K., Pluvinage, J.V.*, et al.* (2019). Single-cell analysis reveals T cell infiltration in old neurogenic niches. Nature *571*, 205-210.

Ellwardt, E., Walsh, J.T., Kipnis, J., and Zipp, F. (2016). Understanding the Role of T Cells in CNS Homeostasis. Trends Immunol *37*, 154-165.

Etzerodt, A., Tsalkitzi, K., Maniecki, M., Damsky, W., Delfini, M., Baudoin, E., Moulin, M., Bosenberg, M., Graversen, J.H., Auphan-Anezin, N.*, et al.* (2019). Specific targeting of CD163(+) TAMs mobilizes inflammatory monocytes and promotes T cell-mediated tumor regression. J Exp Med *216*, 2394-2411.

Fitzpatrick, Z., Frazer, G., Ferro, A., Clare, S., Bouladoux, N., Ferdinand, J., Tuong, Z.K., Negro-Demontel, M.L., Kumar, N., Suchanek, O.*, et al.* (2020). Gut-educated IgA plasma cells defend the meningeal venous sinuses. Nature *587*, 472-476.

Franceschi, C., Garagnani, P., Parini, P., Giuliani, C., and Santoro, A. (2018). Inflammaging: a new immune-metabolic viewpoint for age-related diseases. Nat Rev Endocrinol *14*, 576-590.

Gaya, M., Castello, A., Montaner, B., Rogers, N., Reis e Sousa, C., Bruckbauer, A., and Batista, F.D. (2015). Host response. Inflammation-induced disruption of SCS macrophages impairs B cell responses to secondary infection. Science *347*, 667-672.

Ginhoux, F., Bleriot, C., and Lecuit, M. (2017). Dying for a Cause: Regulated Necrosis of Tissue-Resident Macrophages upon Infection. Trends Immunol *38*, 693-695.

Ginhoux, F., Schultze, J.L., Murray, P.J., Ochando, J., and Biswas, S.K. (2016). New insights into the multidimensional concept of macrophage ontogeny, activation and function. Nat Immunol *17*, 34-40.

Goldmann, T., Wieghofer, P., Jordao, M.J., Prutek, F., Hagemeyer, N., Frenzel, K., Amann, L., Staszewski, O., Kierdorf, K., Krueger, M.*, et al.* (2016). Origin, fate and dynamics of macrophages at central nervous system interfaces. Nat Immunol *17*, 797-805.

Guilliams, M., Dutertre, C.A., Scott, C.L., McGovern, N., Sichien, D., Chakarov, S., Van Gassen, S., Chen, J., Poidinger, M., De Prijck, S.*, et al.* (2016). Unsupervised High-Dimensional Analysis Aligns Dendritic Cells across Tissues and Species. Immunity *45*, 669-684.

Guilliams, M., and Scott, C.L. (2017). Does niche competition determine the origin of tissue-resident macrophages? Nat Rev Immunol *17*, 451-460.

Jordao, M.J.C., Sankowski, R., Brendecke, S.M., Sagar, Locatelli, G., Tai, Y.H., Tay, T.L., Schramm, E., Armbruster, S., Hagemeyer, N.*, et al.* (2019). Single-cell profiling identifies myeloid cell subsets with distinct fates during neuroinflammation. Science *363*.

Jung, S.R., Ashhurst, T.M., West, P.K., Viengkhou, B., King, N.J.C., Campbell, I.L., and Hofer, M.J. (2020). Contribution of STAT1 to innate and adaptive immunity during type I interferon-mediated lethal virus infection. PLoS Pathog *16*, e1008525.

Kamphuis, E., Junt, T., Waibler, Z., Forster, R., and Kalinke, U. (2006). Type I interferons directly regulate lymphocyte recirculation and cause transient blood lymphopenia. Blood *108*, 3253-3261.

Kang, S.S., Herz, J., Kim, J.V., Nayak, D., Stewart-Hutchinson, P., Dustin, M.L., and McGavern, D.B. (2011). Migration of cytotoxic lymphocytes in cell cycle permits local MHC I-dependent control of division at sites of viral infection. J Exp Med *208*, 747-759.

Kang, S.S., and McGavern, D.B. (2008). Lymphocytic choriomeningitis infection of the central nervous system. Front Biosci *13*, 4529-4543.

Kang, S.S., and McGavern, D.B. (2009). Inflammation on the mind: visualizing immunity in the central nervous system. Curr Top Microbiol Immunol *334*, 227-263.

Kim, J.V., Kang, S.S., Dustin, M.L., and McGavern, D.B. (2009). Myelomonocytic cell recruitment causes fatal CNS vascular injury during acute viral meningitis. Nature *457*, 191-195.

Kim, K.S. (2010). Acute bacterial meningitis in infants and children. Lancet Infect Dis *10*, 32-42.

Kipnis, J., Cohen, H., Cardon, M., Ziv, Y., and Schwartz, M. (2004). T cell deficiency leads to cognitive dysfunction: implications for therapeutic vaccination for schizophrenia and other psychiatric conditions. Proc Natl Acad Sci U S A *101*, 8180-8185.

Kipnis, J., Gadani, S., and Derecki, N.C. (2012). Pro-cognitive properties of T cells. Nat Rev Immunol *12*, 663-669.

Korin, B., Ben-Shaanan, T.L., Schiller, M., Dubovik, T., Azulay-Debby, H., Boshnak, N.T., Koren, T., and Rolls, A. (2017). High-dimensional, single-cell characterization of the brain's immune compartment. Nat Neurosci *20*, 1300-1309.

Kwong, B., Rua, R., Gao, Y., Flickinger, J., Jr., Wang, Y., Kruhlak, M.J., Zhu, J., Vivier, E., McGavern, D.B., and Lazarevic, V. (2017). T-bet-dependent NKp46(+) innate lymphoid cells regulate the onset of TH17-induced neuroinflammation. Nat Immunol *18*, 1117-1127.

Le Bon, A., Thompson, C., Kamphuis, E., Durand, V., Rossmann, C., Kalinke, U., and Tough, D.F. (2006). Cutting edge: enhancement of antibody responses through direct stimulation of B and T cells by type I IFN. J Immunol *176*, 2074-2078.

Liu, Z., Gu, Y., Chakarov, S., Bleriot, C., Kwok, I., Chen, X., Shin, A., Huang, W., Dress, R.J., Dutertre, C.A.*, et al.* (2019). Fate Mapping via Ms4a3-Expression History Traces Monocyte-Derived Cells. Cell *178*, 1509-1525 e1519.

Ma, T., Wang, F., Xu, S., and Huang, J.H. (2021). Meningeal immunity: Structure, function and a potential therapeutic target of neurodegenerative diseases. Brain Behav Immun *93*, 264-276.

Malissen, M., Gillet, A., Ardouin, L., Bouvier, G., Trucy, J., Ferrier, P., Vivier, E., and Malissen, B. (1995). Altered T cell development in mice with a targeted mutation of the CD3-epsilon gene. EMBO J *14*, 4641-4653.

Manglani, M., and McGavern, D.B. (2017). New advances in CNS immunity against viral infection. Curr Opin Virol *28*, 116-126.

Mrdjen, D., Pavlovic, A., Hartmann, F.J., Schreiner, B., Utz, S.G., Leung, B.P., Lelios, I., Heppner, F.L., Kipnis, J., Merkler, D.*, et al.* (2018). High-Dimensional Single-Cell Mapping of Central Nervous System Immune Cells Reveals Distinct Myeloid Subsets in Health, Aging, and Disease. Immunity *48*, 380-395 e386.

Nobs, S.P., and Kopf, M. (2021). Tissue-resident macrophages: guardians of organ homeostasis. Trends Immunol *42*, 495-507.

Oh, J., and Shin, J.S. (2015). Molecular mechanism and cellular function of MHCII ubiquitination. Immunol Rev *266*, 134-144.

Perdiguero, E.G., and Geissmann, F. (2016). The development and maintenance of resident macrophages. Nat Immunol *17*, 2-8.

Polfliet, M.M., Goede, P.H., van Kesteren-Hendrikx, E.M., van Rooijen, N., Dijkstra, C.D., and van den Berg, T.K. (2001a). A method for the selective depletion of perivascular and meningeal macrophages in the central nervous system. J Neuroimmunol *116*, 188-195.

Polfliet, M.M., Zwijnenburg, P.J., van Furth, A.M., van der Poll, T., Dopp, E.A., Renardel de Lavalette, C., van Kesteren-Hendrikx, E.M., van Rooijen, N., Dijkstra, C.D., and van den Berg, T.K. (2001b). Meningeal and perivascular macrophages of the central nervous system play a protective role during bacterial meningitis. J Immunol *167*, 4644-4650.

Prinz, M., Erny, D., and Hagemeyer, N. (2017). Ontogeny and homeostasis of CNS myeloid cells. Nat Immunol *18*, 385-392.

Rua, R., Lee, J.Y., Silva, A.B., Swafford, I.S., Maric, D., Johnson, K.R., and McGavern, D.B. (2019). Infection drives meningeal engraftment by inflammatory monocytes that impairs CNS immunity. Nat Immunol *20*, 407-419.

Rua, R., and McGavern, D.B. (2018). Advances in Meningeal Immunity. Trends Mol Med.

Rustenhoven, J., Drieu, A., Mamuladze, T., de Lima, K.A., Dykstra, T., Wall, M., Papadopoulos, Z., Kanamori, M., Salvador, A.F., Baker, W.*, et al.* (2021). Functional characterization of the dural sinuses as a neuroimmune interface. Cell *184*, 1000-1016 e1027.

Sahu, R.N., Kumar, R., and Mahapatra, A.K. (2009). Central nervous system infection in the pediatric population. J Pediatr Neurosci *4*, 20-24.

Salvador, A.F., de Lima, K.A., and Kipnis, J. (2021). Neuromodulation by the immune system: a focus on cytokines. Nat Rev Immunol *21*, 526-541.

Schafflick, D., Wolbert, J., Heming, M., Thomas, C., Hartlehnert, M., Borsch, A.L., Ricci, A., Martin-Salamanca, S., Li, X., Lu, I.N.*, et al.* (2021). Single-cell profiling of CNS border compartment leukocytes reveals that B cells and their progenitors reside in non-diseased meninges. Nat Neurosci *24*, 1225-1234.

Schwartz, M., and Baruch, K. (2014). The resolution of neuroinflammation in neurodegeneration: leukocyte recruitment via the choroid plexus. EMBO J *33*, 7-22.

Steel, C.D., Kim, W.K., Sanford, L.D., Wellman, L.L., Burnett, S., Van Rooijen, N., and Ciavarra, R.P. (2010). Distinct macrophage subpopulations regulate viral encephalitis but not viral clearance in the CNS. J Neuroimmunol *226*, 81-92.

Stoeckius, M., Zheng, S., Houck-Loomis, B., Hao, S., Yeung, B.Z., Mauck, W.M., 3rd, Smibert, P., and Satija, R. (2018). Cell Hashing with barcoded antibodies enables multiplexing and doublet detection for single cell genomics. Genome Biol *19*, 224.

Stuart, T., Butler, A., Hoffman, P., Hafemeister, C., Papalexi, E., Mauck, W.M., 3rd, Hao, Y., Stoeckius, M., Smibert, P., and Satija, R. (2019). Comprehensive Integration of Single-Cell Data. Cell *177*, 1888-1902 e1821.

Tomasello, E., Naciri, K., Chelbi, R., Bessou, G., Fries, A., Gressier, E., Abbas, A., Pollet, E., Pierre, P., Lawrence, T.*, et al.* (2018). Molecular dissection of plasmacytoid dendritic cell activation in vivo during a viral infection. EMBO J *37*.

Utz, S.G., See, P., Mildenberger, W., Thion, M.S., Silvin, A., Lutz, M., Ingelfinger, F., Rayan, N.A., Lelios, I., Buttgereit, A.*, et al.* (2020). Early Fate Defines Microglia and Non-parenchymal Brain Macrophage Development. Cell *181*, 557-573 e518.

Van Hove, H., Martens, L., Scheyltjens, I., De Vlaminck, K., Pombo Antunes, A.R., De Prijck, S., Vandamme, N., De Schepper, S., Van Isterdael, G., Scott, C.L.*, et al.* (2019). A single-cell atlas of mouse brain macrophages reveals unique transcriptional identities shaped by ontogeny and tissue environment. Nat Neurosci *22*, 1021-1035.

Waisman, A., Liblau, R.S., and Becher, B. (2015). Innate and adaptive immune responses in the CNS. Lancet Neurol *14*, 945-955.

Wang, A.Z., Bowman-Kirigin, J.A., Desai, R., Kang, L.I., Patel, P.R., Patel, B., Khan, S.M., Bender, D., Marlin, M.C., Liu, J.*, et al.* (2022). Single-cell profiling of human dura and meningioma reveals cellular meningeal landscape and insights into meningioma immune response. Genome Med *14*, 49.

Weller, R.O., Sharp, M.M., Christodoulides, M., Carare, R.O., and Mollgard, K. (2018). The meninges as barriers and facilitators for the movement of fluid, cells and pathogens related to the rodent and human CNS. Acta Neuropathol *135*, 363-385.

Key resources table

REAGENT or RESOURCE	SOURCE	IDENTIFIER
Antibodies		
Brilliant Violet 421 rat monoclonal anti-mouse I-A/I-E (clone M5/114.15.2)	BioLegend	Cat#107632 ; RRID:AB_2650896
Alexa Fluor 488 rat monoclonal anti-mouse Ly-6C (clone HK1.4)	BioLegend	Cat# 128022, RRID:AB_10639728
Alexa Fluor 488 rat monoclonal anti-mouse Ly-6C (clone HK1.4)	BioLegend	Cat# 128022, RRID:AB_10639728
Alexa Fluor 488 rat monoclonal anti-mouse CD206 (MMR) (clone C068C2)	BioLegend	Cat# 141710, RRID:AB_10900445
Alexa Fluor(R) 647 rat monoclonal anti-mouse CD206 (clone C068C2)	BioLegend	Cat# 141712, RRID:AB_10900420
Alexa Fluor(R) 488 rat monoclonal anti-mouse/human CD11b (clone M1/70)	BioLegend	Cat# 101217, RRID:AB_389305
PE rat monoclonal anti-mouse CD31 (clone 390)	BioLegend	Cat# 102408, RRID:AB_312903
PE rat monoclonal anti-mouse CD8a (clone 53-6.7)	BioLegend	Cat# 100707, RRID:AB_312746
Alexa Fluor 647 donkey polyclonal anti-rabbit IgG (Poly4064)	BioLegend	Cat# 406414, RRID:AB_2563202
Mouse monoclonal anti-human HLA-DR	BioLegend	Cat# 307602, RRID:AB_314680
Brilliant Violet 570(TM) rat monoclonal anti-mouse/human CD11b (clone M1/70)	BioLegend	Cat# 101233, RRID:AB_10896949
Brilliant Violet 711 rat monoclonal anti-mouse Ly-6G (clone RA3–6B2)	BioLegend	Cat# 127643, RRID:AB_2565971
PE/Cyanine7 rat monoclonal anti-mouse CD206 (clone C068C2)	BioLegend	Cat# 141720, RRID:AB_2562248
PE mouse (C3H) anti-mouse H-2Kb/H-2Db (clone 28–8-6	BioLegend	Cat# 114607, RRID:AB_313598
Alexa Fluor 700 rat monoclonal anti-mouse CD8a (clone SK1)	BioLegend	Cat# 100730, RRID:AB_493703
APC mouse monoclonal anti-mouse NK-1.1 (clone S17016D)	BioLegend	Cat# 108710, RRID:AB_313397
Brilliant Violet 605 mouse monoclonal anti-mouse CD64 (FcgammaRI) (clone X54–5/7.1)	BioLegend	Cat# 139323, RRID:AB_2629778
Alexa Fluor 647 rat monoclonal anti-mouse CD115 (clone AFS98)	BioLegend	Cat# 135530, RRID:AB_2566525
PE rat monoclonal anti-mouse CD26 (clone H194-112)	BioLegend	Cat# 137804, RRID:AB_2293047
Brilliant Violet 510 mouse monoclonal anti-mouse/rat XCR1 (clone ZET)	BioLegend	Cat# 148218, RRID:AB_2565231
APC/Cyanine7 rat monoclonal anti-mouse F4/80 (clone BM8)	BioLegend	Cat# 123118, RRID:AB_893477
PE rat monoclonal anti-mouse CD68 (clone FA-11)	BioLegend	Cat# 137013, RRID:AB_10613469
Alexa Fluor 647 armenian hamster monoclonal anti-mouse CD55 (clone DAF)	BioLegend	Cat# 131805, RRID:AB_1279263
PE rat monoclonal anti-mouse CD38	BioLegend	Cat# 102707, RRID:AB_312928

Goat anti-mouse Iba1	Novus	Cat# NB 100-1028, RRID:AB_521594
Rabbit polyclonal anti-mouse Iba1	FUJIFILM Wako Shibayagi	Cat# 019-19741, RRID:AB_839504
Rabbit polyclonal anti-mouse NF-H	Abcam	Cat# ab8135, RRID:AB_306298
Donkey anti-Goat IgG (H+L) Cross-Adsorbed Secondary Antibody, Alexa Fluor™ 488	Thermo Fisher Scientific	Cat# A-11055, RRID:AB_2534102
Chicken recombinant monoclonal anti-human Iba1	Synaptic Systems	Cat# 234 009, RRID:AB_2891282
Rat monoclonal anti-mouse CD16/CD32	BD Biosciences	Cat# 553141, RRID:AB_394656
Mouse IgG whole molecule	Jackson ImmunoResearch Labs	Cat# 015-000-003, RRID:AB_2337188
BUV395 rat monoclonal anti-mouse CD90.2 (clone 53-2.1)	BD Biosciences	Cat# 565257, RRID:AB_2739136
PE-CF594 rat monoclonal anti-mouse Ly-6C (clone AL-21)	BD Biosciences	Cat# 562728, RRID:AB_2737749
BV786 rat monoclonal anti-mouse CD4 (Clone RM4-5)	BD Biosciences	Cat# 563727, RRID:AB_2728707
PE-Cyanine5.5 Armenian hamster monoclonal anti-mouse CD11c (clone N418)	Thermo Fisher Scientific	Cat# 35-0114-82, RRID:AB_469709
BV650 rat monoclonal anti-mouse CD24 (clone M1/69)	BD Biosciences	Cat# 563545, RRID:AB_2738271
AF700 rat monoclonal anti-mouse MerTK (clone DS5MMER)	Thermo Fisher Scientific	Cat# 56-5751-80, RRID:AB_2784770
FITC rat monoclonal anti-mouse CD172a (clone P84)	BD Biosciences	Cat# 560316, RRID:AB_1645240
InVivo mAb anti-LCMV nucleoprotein (clone VL-4)	Bio X Cell	Cat# BE0106, RRID:AB_10949017
Alexa Fluor 647 rat IgG2A anti-LCMV Nucleoprotein (clone VL-4) in house conjugation	Bio X Cell	Cat# BE0106, RRID:AB_10949017
InVivoMAb anti-mouse CD8α (clone YTS169.4)	Bio X Cell	Cat# BE0117, RRID:AB_10950145
InVivoMab anti-mouse CD4 (clone GK1.5)	Bio X Cell	Cat# BE0003-1, RRID:AB_1107636
InVivoPlus anti-mouse IL-10R (clone 1B1.3A)	Bio X Cell	Cat# BE0050, RRID:AB_1107611
InVivoMAb rat IgG1 isotype control, anti-horseradish peroxidase (clone LTF-2)	Bio X Cell	Cat# BE0088, RRID:AB_1107775
InVivoMab anti-mouse LFA-1α (clone M17/4)	Bio X Cell	Cat# BE0006, RRID:AB_1107578
InVivoMab anti-mouse/human VLA-4 (clone PS/2)	Bio X Cell	Cat# BE0071, RRID:AB_1107657
TotalSeq-A, clone M1/42; 30-F11	BioLegend	Cat# 155809; Cat# 155811; Cat# 155813; Cat#155815
Bacterial and virus strains		
LCMV Armstrong clone 53b	Laboratory of Dr. D. McGavern	Kang & McGavern, 2008
SARS-CoV-2	Dr. X Lescure and Pr. Y Yazdanpanah, Bichat Hospital Paris	EVAg: BetaCoV/France/IDF 0372/2020
Biological samples		

Baboons	Rousset	N/A
Chemicals, peptides, and recombinant proteins		
Formalin solution, neutral buffered, 10%	Sigma-Aldrich	Cat# HT501128
Cytofix/Cytoperm	BD Biosciences	Cat# 554714
LiveDead fixable Blue Cell Staining kit	Thermo Fisher Scientific	Cat# L23105
Mix-n-Stain CF 647	Sigma-Aldrich	Cat# MX647S100
Click-iT™ EdU Alexa Fluor™ 488 Flow Cytometry Assay Kit	Thermo Fisher Scientific	Cat# C10425
Collagenase D	Sigma-Aldrich	Cat# 11088866001
DNase I	Sigma-Aldrich	Cat# 11284932001
Percoll	Sigma-Aldrich	Cat# GE17-0891-01
RBC 1X Lysis Buffer	Thermo Fisher Scientific	Cat# 00-4333-57
Histodenz clearing medium	Sigma-Aldrich	Cat# D2158
PLX3397	DC Chemicals	Cat# DC8158
PLX5622	DC Chemicals	Cat# DC21518
Corn oil	Sigma-Aldrich	Cat# C8267
LPS	InvivoGen	Cat# tlrl-3pelps
Dextran-Rhodamine B isothiocyanate (70 kDa)	Sigma-Aldrich	Cat# R9379
Evans Blue	Sigma-Aldrich	Cat# E2129
Carboxymethylcellulose	Sigma-Aldrich	Cat# C4888
Diphteria Toxin	Sigma-Aldrich	Cat# D0564
Tamoxifen	Cayman Chemicals	Cat# 13258
Hoechst 33342	Sigma-Aldrich	Cat# B2261
Draq7	Thermo Fisher Scientific	Cat# D15106
TRIzol Reagent	Thermo Fisher Scientific	Cat# 15596026
UltraPure agarose	Thermo Fisher Scientific	Cat# 16500500
1Kb Plus DNA Ladder	Thermo Fisher Scientific	Cat# 10787026
Critical commercial assays		
Antiviral response (SAB Target List) M96	BioRad	Cat# 10034277
Single Cell 3'v3 Gel Bead and Library Kit	10X Genomics	Cat# 1000092
Chromium i7 Multiplex kit	10X Genomics	Cat# 120262
DynaBeads MyOne Silane Beads	Thermo Fisher Scientific	Cat# 37002D
iScript cDNA Synthesis Kit	BioRad	Cat# 1708891
TB Green® Advantage® qPCR Premix	Takara	Cat# 639676
NextSeq500/500 High Output Kit (75 Cycles)	Illumina	Cat# 20024906
ExactLadder DNA Premix	Ozyme	Cat# OZYC002-100
SPRIselect Reagent Kit	Beckman Coulter	Cat #B23317
SsoADV Universal SYBR Green Supermix	BioRad	Cat# 1725272
CD8 negative selection kit	Stem Cell Technologies	Cat# 19853
Deposited data		
scRNAseq	This paper	Gene Expression Omnibus : GSE189887

Experimental models: Cell lines		
Vero E6 cells	American Type Culture Collection	CRL-1586
Experimental models: Organisms/strains		
Mouse: B6 : C57BL/6J	The Jackson Laboratory	RRID:IMSR_JAX:000664
Mouse: Cx3cr1-CreERT2: B6.129P2(Cg)-*Cx3cr1*$^{tm2.1(Cre/ERT2)Litt}$/WganJ	The Jackson Laboratory	RRID:IMSR_JAX:021160
Mouse: LysM-Cre: B6.129P2-*Lyz2*$^{tm1(cre)Ifo}$/J	The Jackson Laboratory	RRID:IMSR_JAX:004781
Mouse: R26- LSL-TdTomato: B6.Cg-*Gt(ROSA)26Sor*$^{tm14(CAG-tdTomato)Hze}$/J	The Jackson Laboratory	RRID:IMSR_JAX:007914
Mouse: R26-LSL-YFP: B6.129X1-*Gt(ROSA)26Sor*$^{tm1(EYFP)Cos}$/J	The Jackson Laboratory	RRID:IMSR_JAX:006148
Mouse: Cs1fr-LSL-DTR: C57BL/6-Tg(Csf1r-HBEGF/mCherry)1Mnz/J	The Jackson Laboratory	RRID:IMSR_JAX:024046
Mouse: K18-hACE2: B6.Cg-Tg(K18-ACE2)2Prlmn/J	The Jackson Laboratory	RRID:IMSR_JAX:034860
Mouse: H2-Ab1$^{fl/fl:}$ B6.129X1-*H2-Ab1*^{tm1Koni}/J	The Jackson Laboratory	RRID:IMSR_JAX:013181
Mouse: CD3$^{-/-}$: *Cd3e*$^{\Delta 5/\Delta 5}$	Laboratory of Dr. B. Malissen	Malissen et al., 1995
Mouse: Ms4a3-Cre : *Ms4a3*^{Cre}	F. Ginhoux; Liu et al., 2019	RRID:IMSR_JAX:036382
Mouse: P14: C57BL/6 GFP $D^bGP_{33–41}$ TCR-tg	Laboratory of Dr. D. McGavern	Rua et al., 2019
Mouse: actin-OFP	Laboratory of Dr. D. McGavern	Rua et al., 2019
Mouse: Ifnar$^{fl/fl}$: 129/Sv-Ifnar1^{tm1Uka}	Laboratory of Dr. M. Dalod	Le Bon et al., 2006
Mouse: Stat1$^{fl/fl}$: C57BL/6-Stat1$^{tm1c(EUCOMM)Wts}$	Laboratory of Dr. M. Dalod	Tomasello et al., 2018
Mouse: Cd163-Cre	Laboratory of Dr. T. Lawrence	Etzerodt et al., 2019
Oligonucleotides		
Primers for mouse Actin (*Actb*) Forward : 5'-AGCTCATTGTAGAAGGTGTGG-3' ; Reverse : 5'-GTGGGAATGGGTCAGAAGG-3'	Integrated DNA Technologies	NCBI : NM_007393
Primers for LCMV glycoprotein : Forward : 5'-CAGAAATGTTGATGCTGGACTGC-3' ; Reverse : 5'-CAGACCTTGGCTTGCTTTACACAG-3'	Integrated DNA Technologies	N/A
Primers for mouse Ifnar : Forward : 5'-AGACCAGCAACTTCAGTGAAA-3' ; Reverse 5'-TTGAAGGCGGCTCAGAGA-3'	Integrated DNA Technologies	NCBI : NM_01508.2
Software and algorithms		
FlowJo	TreeStar Inc.	https://www.flowjo.com/
Prism 9.1.2.	GraphPad	https://www.graphpad.com/scientific-software/prism/
Imaris 9.6.0	Oxford Instruments	https://imaris.oxinst.com/versions/9-6
R v. 4.0.3	The R Project	https://www.r-project.org/

Seurat package version 3.2.2	Stuart et al., 2019	https://github.com/satijalab/seurat/tree/release/3.0
Code	This paper	https://github.com/mteleman/LCMV_paper_RRLab_PBS_LPS_single_cell
CellRanger version 4	10X Genomics	https://support.10xgenomics.com/single-cell-gene-expression/software/pipelines/latest/installation
CITE-seq-count version 1.4.3	Stoeckius et al., 2018	https://github.com/Hoohm/CITE-seq-Count
Other		
BD FACS Aria III Cell Sorter	BDBiosciences	N/A
2100 BioAnalyzer	Agilent	N/A
Chromium Controller	10X Genomics	N/A
Cytek Aurora CS	Cytek	https://cytekbio.com/pages/aurora-cs
BD FACS Symphony A5 Cell Analyzer	BDBiosciences	N/A

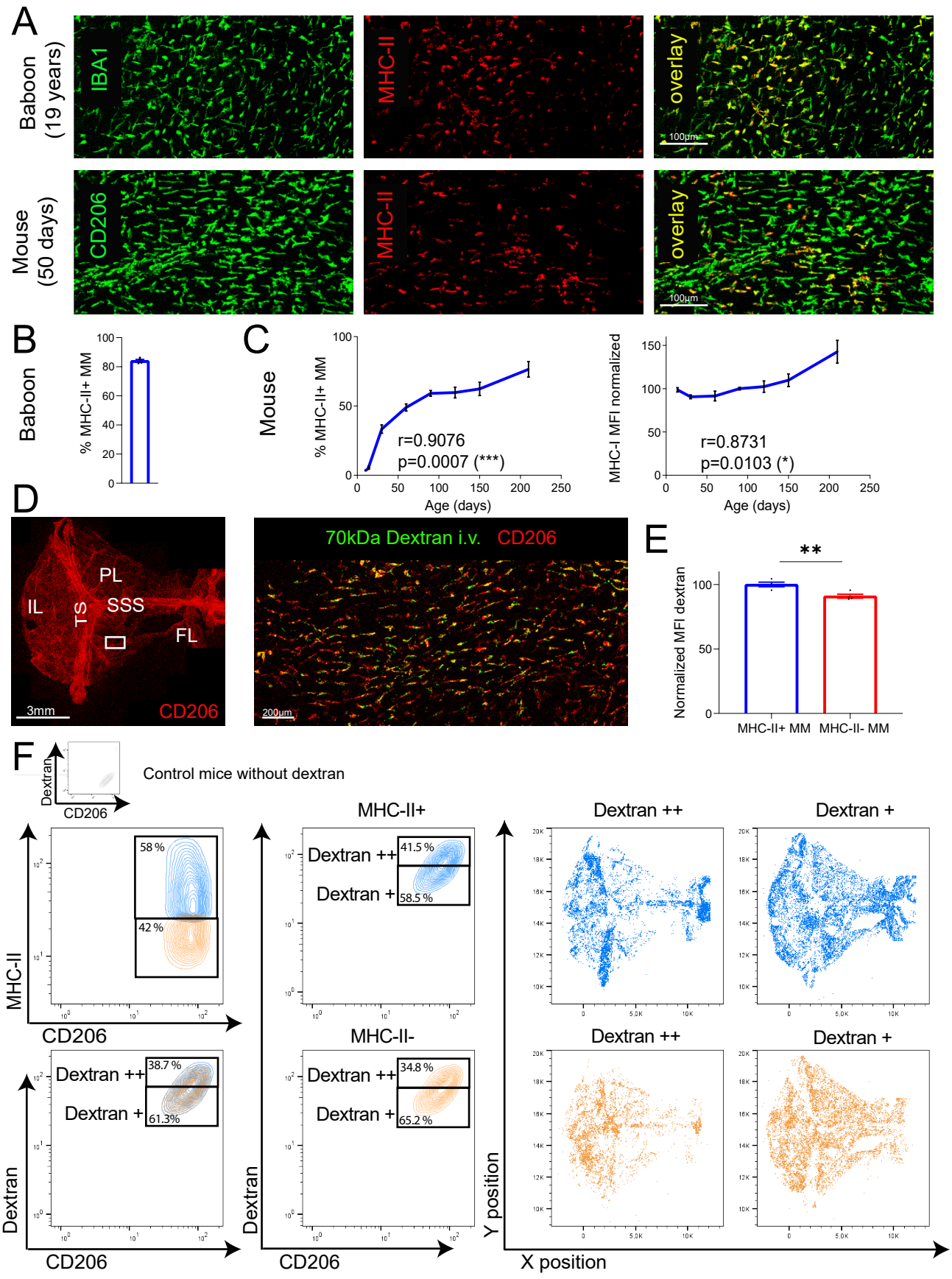
A
Baboon (19 years)
IBA1
MHC-II
overlay
100µm
Mouse (50 days)
CD206
MHC-II
overlay
100µm
B
Baboon
% MHC-II+ MM
C
Mouse
% MHC-II+ MM
r=0.9076
p=0.0007 (***)
Age (days)
MHC-I MFI normalized
r=0.8731
p=0.0103 (*)
Age (days)
D
PL
IL
TS
SSS
FL
3mm
CD206
70kDa Dextran i.v.
CD206
200µm
E
**
Normalized MFI dextran
MHC-II+ MM
MHC-II- MM
F
Dextran
CD206
Control mice without dextran
MHC-II+
MHC-II-
Dextran ++
Dextran +
58 %
42 %
41.5 %
58.5 %
38.7 %
61.3%
34.8 %
65.2 %
MHC-II
CD206
Dextran
Y position
X position

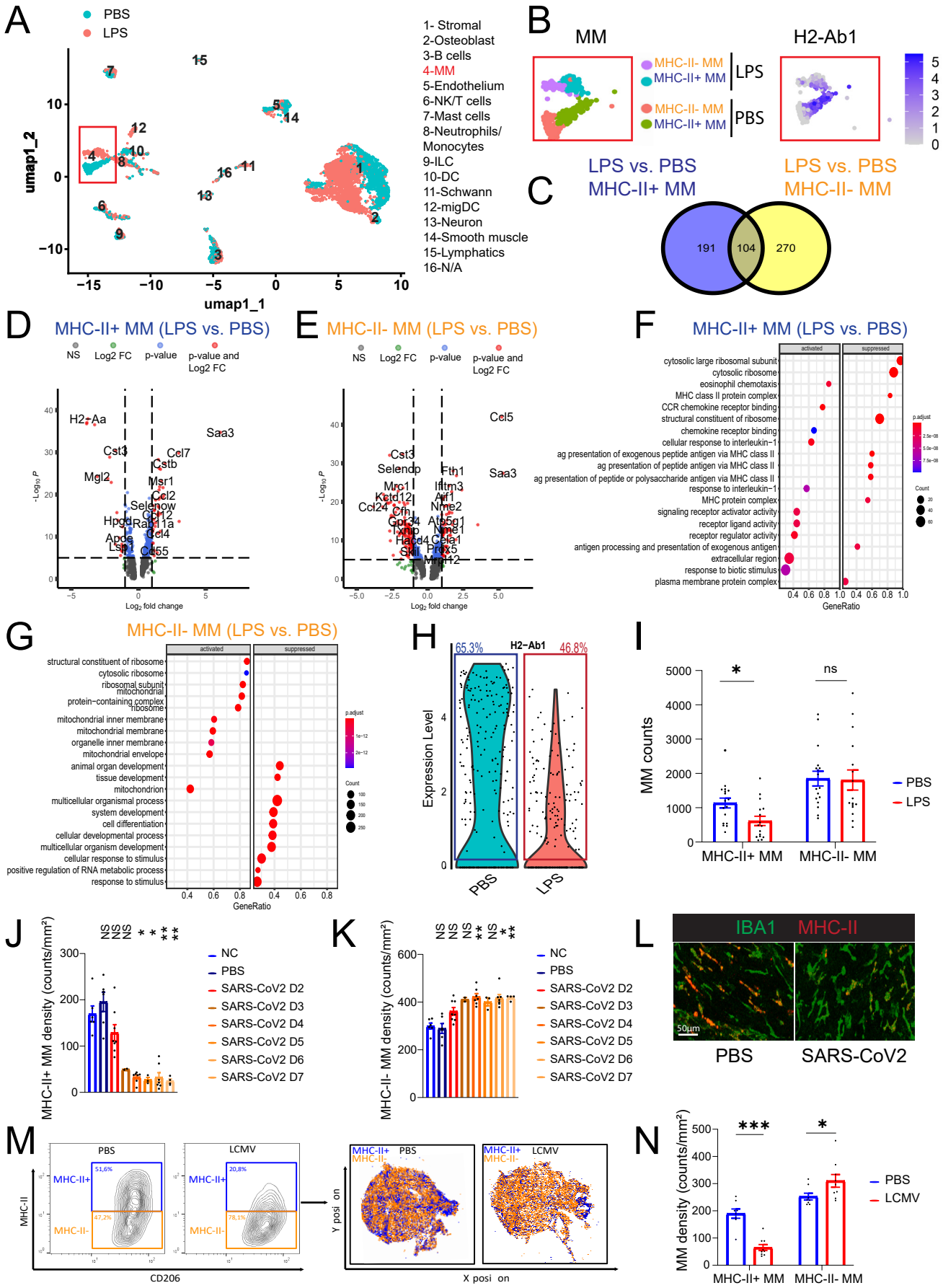
A
PBS
LPS
1- Stromal
2-Osteoblast
3-B cells
4-MM
5-Endothelium
6-NK/T cells
7-Mast cells
8-Neutrophils/ Monocytes
9-ILC
10-DC
11-Schwann
12-migDC
13-Neuron
14-Smooth muscle
15-Lymphatics
16-N/A
umap1_1
umap1_2
B
MM
H2-Ab1
MHC-II- MM
MHC-II+ MM
LPS
PBS
C
LPS vs. PBS MHC-II+ MM
LPS vs. PBS MHC-II- MM
191
104
270
D
MHC-II+ MM (LPS vs. PBS)
NS
Log2 FC
p-value
p-value and Log2 FC
H2-Aa
Saa3
Cst3
Ccl7
Cstb
Mgl2
Msr1
Ccl2
Selenow
Ccl12
Hpgd
Rab11a
Ccl4
Apoe
Lsp1
Ccl5
Log2 fold change
E
MHC-II- MM (LPS vs. PBS)
Ccl5
Saa3
Selenop
Fth1
Mrc1
Ifitm3
Ccl24
Arf1
Nme2
Cfh
Gpr34
Atp6g1
Lyzp
Nme1
Hacd4
Cela1
Skil
Prdx5
Mmp12
F
MHC-II+ MM (LPS vs. PBS)
activated
suppressed
cytosolic large ribosomal subunit
cytosolic ribosome
eosinophil chemotaxis
MHC class II protein complex
CCR chemokine receptor binding
structural constituent of ribosome
chemokine receptor binding
cellular response to interleukin−1
ag presentation of exogenous peptide antigen via MHC class II
ag presentation of peptide antigen via MHC class II
ag presentation of peptide or polysaccharide antigen via MHC class II
response to interleukin−1
MHC protein complex
signaling receptor activator activity
receptor ligand activity
receptor regulator activity
antigen processing and presentation of exogenous antigen
extracellular region
response to biotic stimulus
plasma membrane protein complex
p.adjust
Count
GeneRatio
G
MHC-II- MM (LPS vs. PBS)
activated
suppressed
structural constituent of ribosome
cytosolic ribosome
ribosomal subunit
mitochondrial protein−containing complex
ribosome
mitochondrial inner membrane
mitochondrial membrane
organelle inner membrane
mitochondrial envelope
animal organ development
tissue development
mitochondrion
multicellular organismal process
system development
cell differentiation
cellular developmental process
multicellular organism development
cellular response to stimulus
positive regulation of RNA metabolic process
response to stimulus
p.adjust
Count
GeneRatio
H
H2-Ab1
65.3%
46.8%
Expression Level
PBS
LPS
I
MM counts
*
ns
MHC-II+ MM
MHC-II- MM
PBS
LPS
J
MHC-II+ MM density (counts/mm²)
NS NS NS * * * *
NC
PBS
SARS-CoV2 D2
SARS-CoV2 D3
SARS-CoV2 D4
SARS-CoV2 D5
SARS-CoV2 D6
SARS-CoV2 D7
K
MHC-II- MM density (counts/mm²)
NS NS NS * * NS **
NC
PBS
SARS-CoV2 D2
SARS-CoV2 D3
SARS-CoV2 D4
SARS-CoV2 D5
SARS-CoV2 D6
SARS-CoV2 D7
L
IBA1
MHC-II
50µm
PBS
SARS-CoV2
M
PBS
LCMV
MHC-II+
MHC-II-
51,6%
47,2%
20,8%
78,1%
MHC-II
CD206
Y posi on
X posi on
N
MM density (counts/mm²)
***
*
PBS
LCMV
MHC-II+ MM
MHC-II- MM

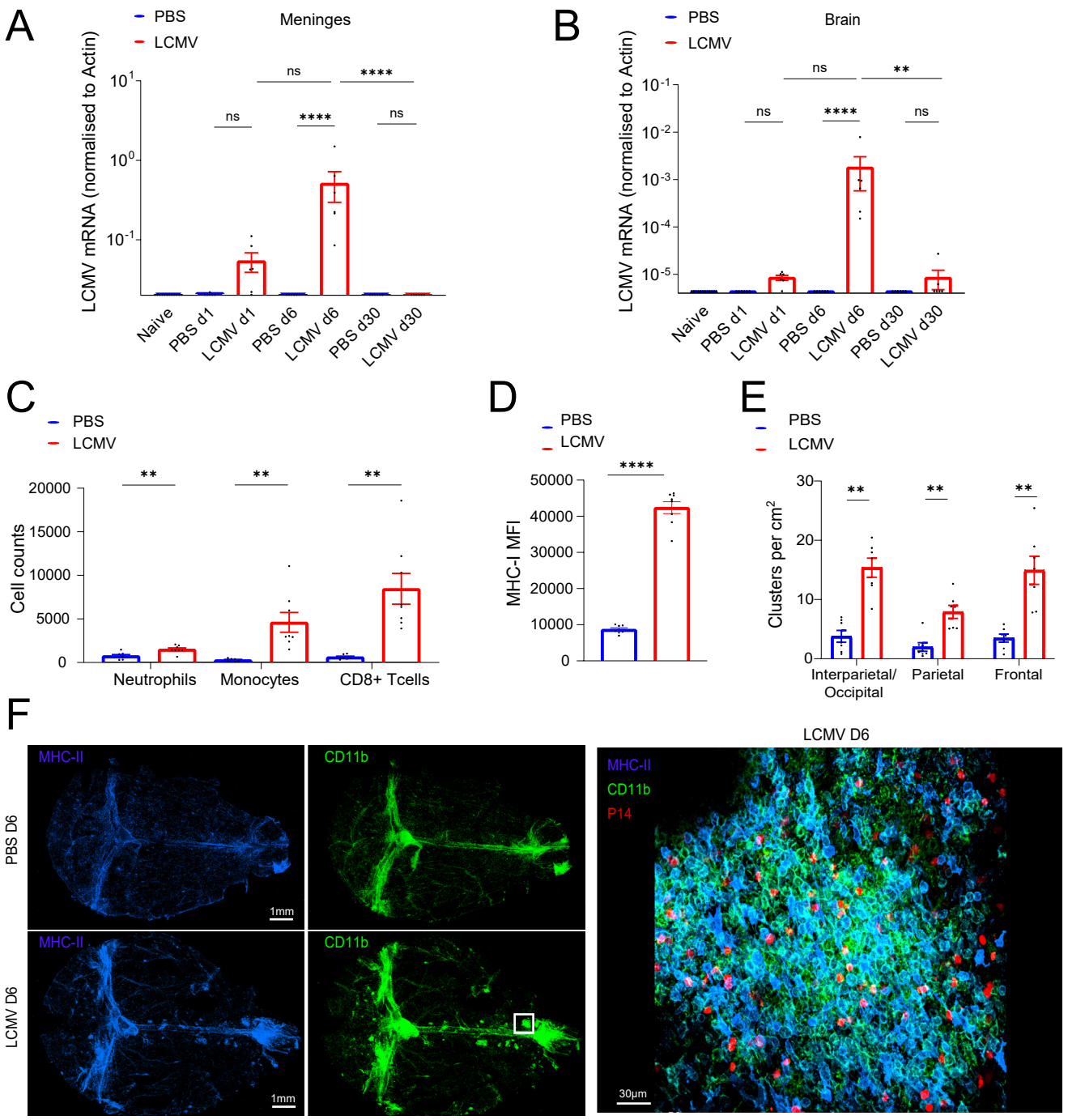
A
PBS
LCMV
Meninges
LCMV mRNA (normalised to Actin)
ns
****
ns
****
ns
Naive
PBS d1
LCMV d1
PBS d6
LCMV d6
PBS d30
LCMV d30
B
PBS
LCMV
Brain
LCMV mRNA (normalised to Actin)
ns
**
ns
****
ns
C
PBS
LCMV
Cell counts
**
**
**
Neutrophils
Monocytes
CD8+ Tcells
D
PBS
LCMV
MHC-I MFI
****
E
PBS
LCMV
Clusters per cm2
**
**
**
Interparietal/ Occipital
Parietal
Frontal
F
PBS D6
LCMV D6
MHC-II
CD11b
1mm
LCMV D6
MHC-II
CD11b
P14
30µm

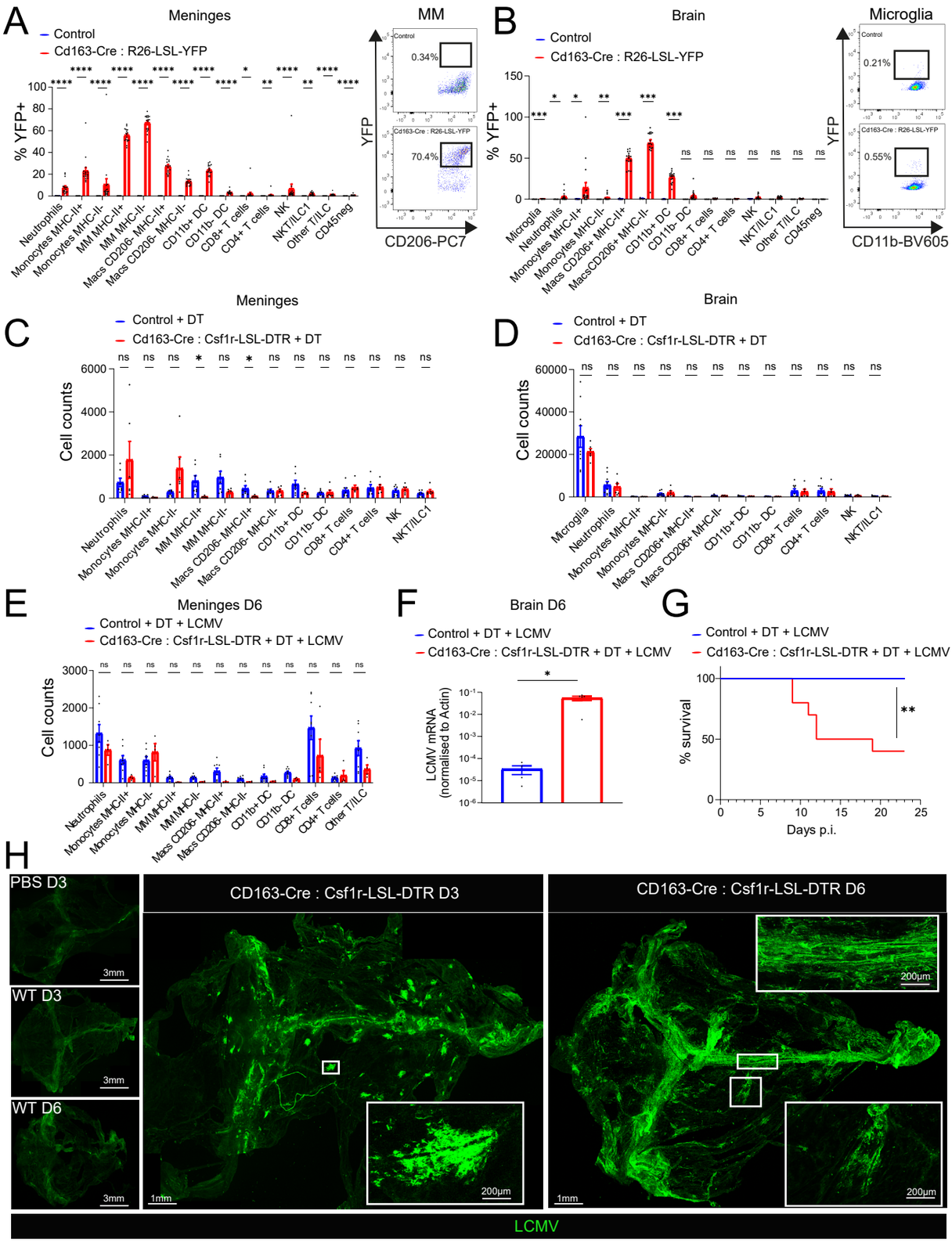
A
Meninges
Control
Cd163-Cre : R26-LSL-YFP
% YFP+
Neutrophils
Monocytes MHC-II+
Monocytes MHC-II-
MM MHC-II+
MM MHC-II-
Macs CD206- MHC-II+
Macs CD206- MHC-II-
CD11b+ DC
CD11b- DC
CD8+ T cells
CD4+ T cells
NK
NKT/ILC1
Other T/ILC
CD45neg
MM
YFP
CD206-PC7
0.34%
70.4%
B
Brain
Microglia
Macs CD206+ MHC-II+
MacsCD206+ MHC-II-
Microglia
0.21%
0.55%
CD11b-BV605
C
Meninges
Control + DT
Cd163-Cre : Csf1r-LSL-DTR + DT
Cell counts
D
Brain
E
Meninges D6
Control + DT + LCMV
Cd163-Cre : Csf1r-LSL-DTR + DT + LCMV
F
Brain D6
LCMV mRNA (normalised to Actin)
G
% survival
Days p.i.
H
PBS D3
WT D3
WT D6
CD163-Cre : Csf1r-LSL-DTR D3
CD163-Cre : Csf1r-LSL-DTR D6
3mm
1mm
200µm
LCMV

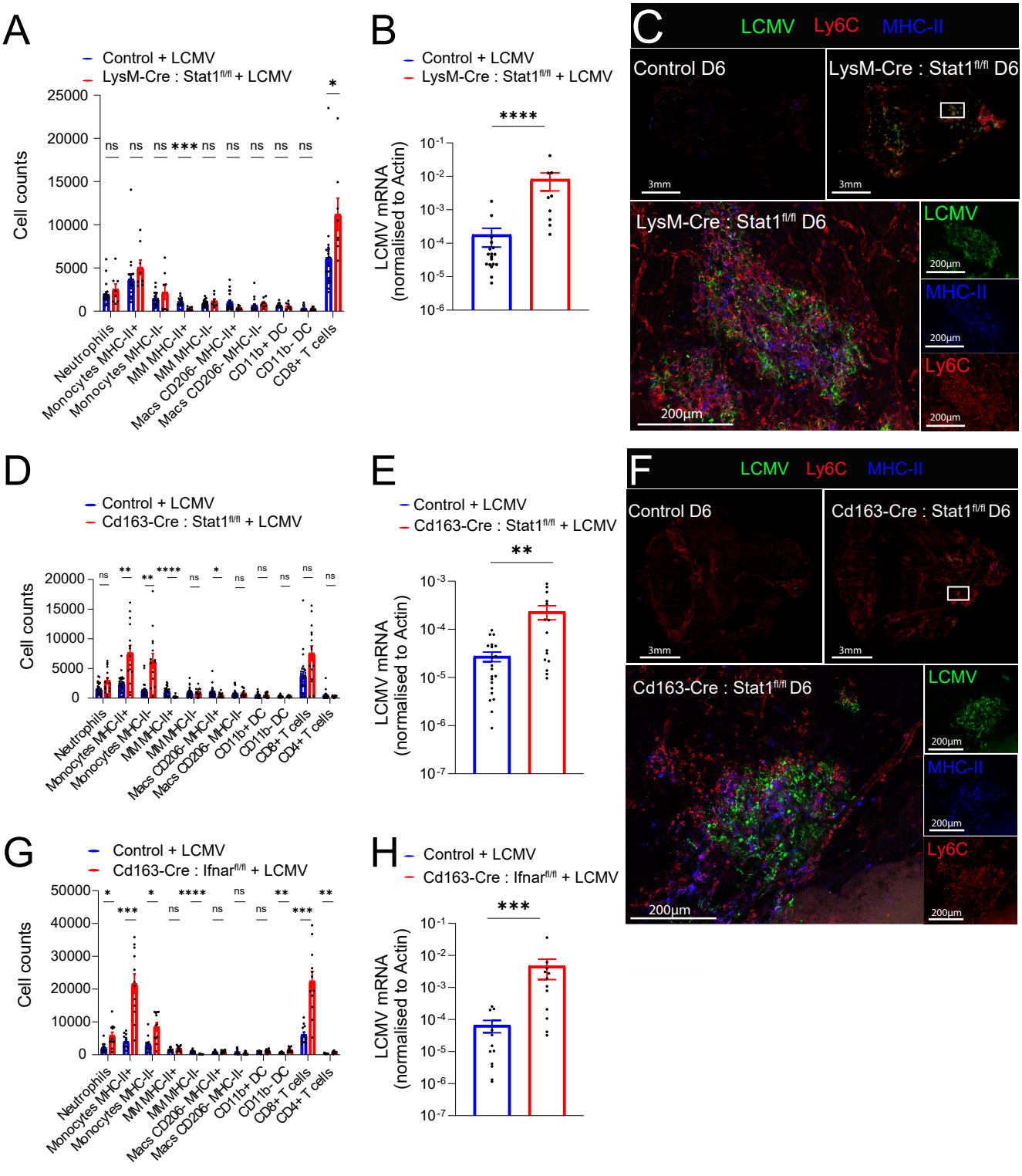
A
Control + LCMV
LysM-Cre : Stat1fl/fl + LCMV
Cell counts
Neutrophils
Monocytes MHC-II+
Monocytes MHC-II-
MM MHC-II+
MM MHC-II-
Macs CD206- MHC-II+
Macs CD206- MHC-II-
CD11b+ DC
CD11b- DC
CD8+ T cells
B
Control + LCMV
LysM-Cre : Stat1fl/fl + LCMV
LCMV mRNA (normalised to Actin)
****
C
LCMV Ly6C MHC-II
Control D6
LysM-Cre : Stat1fl/fl D6
3mm
200µm
D
Control + LCMV
Cd163-Cre : Stat1fl/fl + LCMV
Cell counts
CD4+ T cells
E
Control + LCMV
Cd163-Cre : Stat1fl/fl + LCMV
LCMV mRNA (normalised to Actin)
**
F
LCMV Ly6C MHC-II
Control D6
Cd163-Cre : Stat1fl/fl D6
3mm
200µm
G
Control + LCMV
Cd163-Cre : Ifnarfl/fl + LCMV
Cell counts
H
Control + LCMV
Cd163-Cre : Ifnarfl/fl + LCMV
LCMV mRNA (normalised to Actin)
***

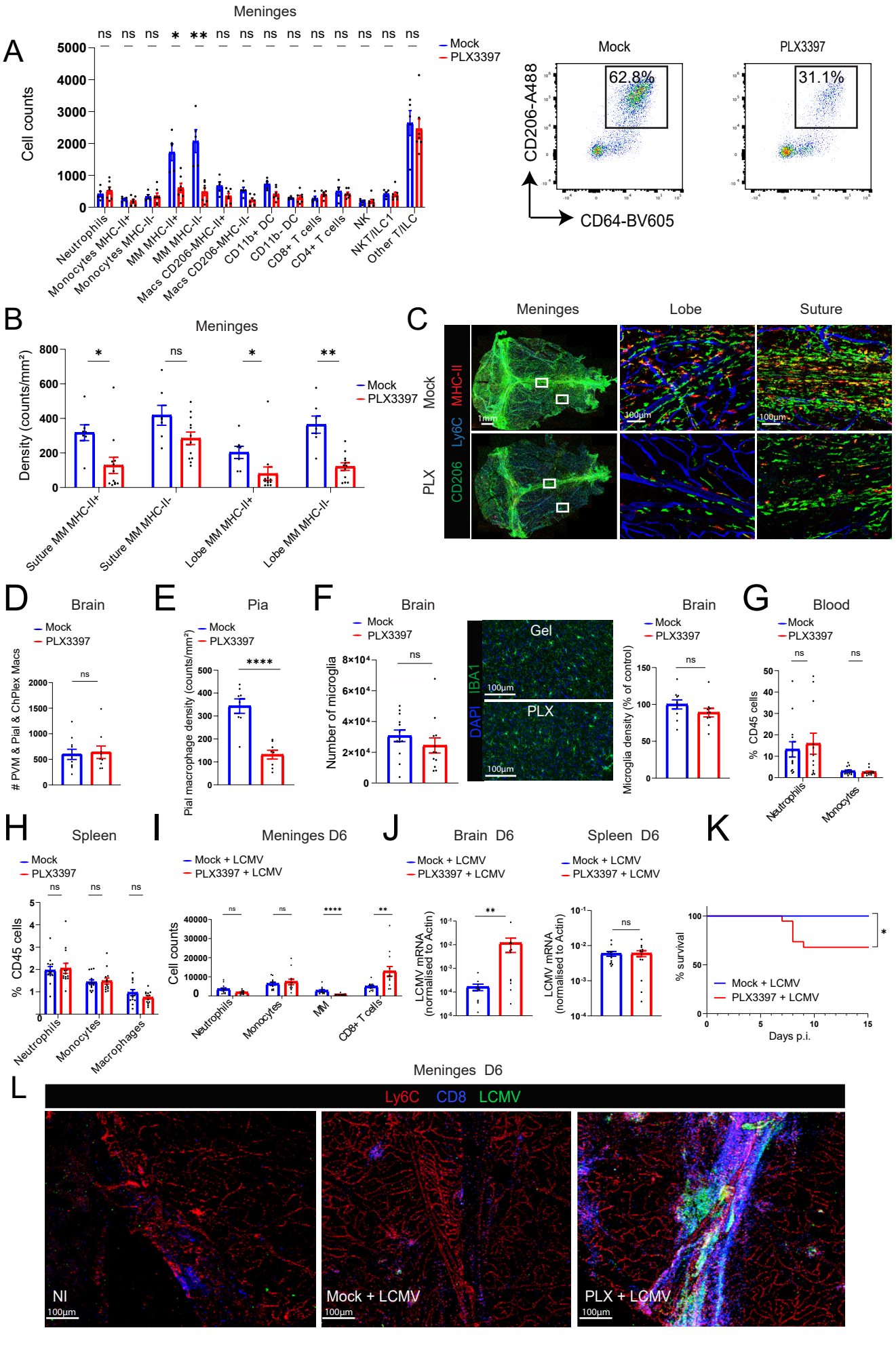
A
Meninges
Cell counts
Mock
PLX3397
Neutrophils
Monocytes MHC-II+
Monocytes MHC-II-
MM MHC-II+
MM MHC-II-
Macs CD206-MHC-II+
Macs CD206-MHC-II-
CD11b+ DC
CD11b- DC
CD8+ T cells
CD4+ T cells
NK
NKT/ILC1
Other T/ILC
Mock
PLX3397
62.8%
31.1%
CD206-A488
CD64-BV605
B
Meninges
Density (counts/mm²)
Suture MM MHC-II+
Suture MM MHC-II-
Lobe MM MHC-II+
Lobe MM MHC-II-
C
Meninges
Lobe
Suture
Mock
PLX
MHC-II
Ly6C
CD206
1mm
100µm
D
Brain
PVM & Pial & ChPlex Macs
E
Pia
Pial macrophage density (counts/mm²)
F
Brain
Number of microglia
Gel
PLX
IBA1
DAPI
Brain
Microglia density (% of control)
G
Blood
% CD45 cells
Neutrophils
Monocytes
H
Spleen
% CD45 cells
Neutrophils
Monocytes
Macrophages
I
Meninges D6
Mock + LCMV
PLX3397 + LCMV
Cell counts
Neutrophils
Monocytes
MM
CD8+ T cells
J
Brain D6
Spleen D6
LCMV mRNA (normalised to Actin)
K
% survival
Days p.i.
Mock + LCMV
PLX3397 + LCMV
L
Meninges D6
Ly6C CD8 LCMV
NI
Mock + LCMV
PLX + LCMV
100µm

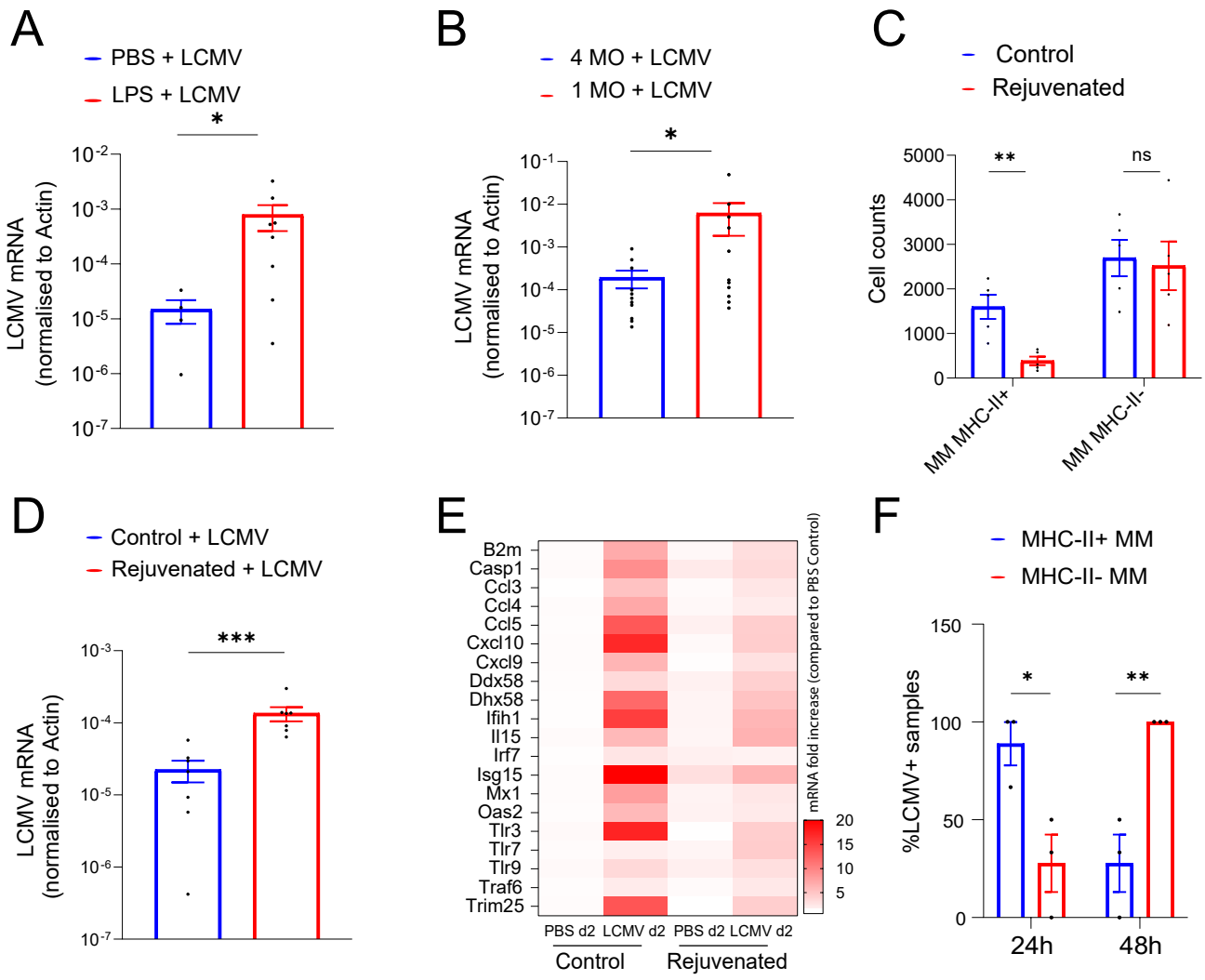
A
PBS + LCMV
LPS + LCMV
*
LCMV mRNA (normalised to Actin)
B
4 MO + LCMV
1 MO + LCMV
*
LCMV mRNA (normalised to Actin)
C
Control
Rejuvenated
**
ns
Cell counts
MM MHC-II+
MM MHC-II-
D
Control + LCMV
Rejuvenated + LCMV
***
LCMV mRNA (normalised to Actin)
E
B2m
Casp1
Ccl3
Ccl4
Ccl5
Cxcl10
Cxcl9
Ddx58
Dhx58
Ifih1
Il15
Irf7
Isg15
Mx1
Oas2
Tlr3
Tlr7
Tlr9
Traf6
Trim25
PBS d2
LCMV d2
PBS d2
LCMV d2
Control
Rejuvenated
mRNA fold increase (compared to PBS Control)
F
MHC-II+ MM
MHC-II- MM
*
**
%LCMV+ samples
24h
48h

Supplementary legends

Supplementary Figure 1. MM represent a dense network at the surface of the CNS and gating strategy for meningeal immune cells (related to Figure 1)

A. Maximal intensity projections of meningeal whole mounts of B6 mice, showing the presence of MM stained with CD206 (green) in the dura mater of the spinal cord. Scale bar: 1 mm. Data is representative of 2 independent experiments, with 5 mice.

B, C. Maximal intensity projections of meningeal whole mounts of B6 mice, showing the presence of MM (CD206, green), blood vessels (CD31, red) and nerve fibers (NF-H, white) in the dura mater of the brain. Scale bar: 1 mm (B). The white inset shows a magnified view of the lobe area. Scale bar: 30 µm (C). Data is representative of 2 independent experiments, with 5 mice.

D. Quantification of the density of MM based on CD206 staining in the brain dural meninges and spinal ventral (Ventral Sp.) and dorsal (Dorsal Sp.) dural meninges. Bar graphs show mean ± s.e.m and asterisks denote statistical significance (ns=not significant; *p<0.05; One-way ANOVA test with Holm-Sidak test for pairwise comparison). Data are representative of 2 independent experiments, with 4 mice (spinal meninges) and 8 mice (brain meninges) per group, and 2 regions (spinal meninges) and 4 regions (brain meninges) quantified per mouse.

E. Quantification of the density of MM based on CD206 staining. Bar graphs show mean ± s.e.m (ns=not significant; One-way ANOVA test with Holm-Sidak test for pairwise comparison). Data are representative of 2 independent experiments, with 5 mice per group, and 2 regions quantified per mouse. D: days old. MO: months old.

F. Quantification of the density of MM based on IBA1 staining showing the density of MM in the baboon dural meninges. Bar graph shows mean ± s.e.m. and data are representative of 4 independent baboons, with 3 regions quantified per baboon.

G. Maximal intensity projections of meningeal whole mounts of B6 mice, showing the presence of MM stained with CD206 (green) and IBA1 (red) in the dura mater of the brain. Scale bar: 50 µm. For *in situ* histocytometry analysis, CD206+ (blue) and IBA1+ (red) surfaces were created and plotted against their isotype (grey), and the proportion of CD206+ and IBA1+ cells, mainly double positive (Q2), is indicated. Data is representative of 2 independent experiments, with 8 mice.

H. Gating strategy for neutrophils, monocytes, MM, other macrophages, $CD11b^+$ DC, $CD11b^-$ DC, $CD8^+$ T cells, $CD4^+$ T cells, NK cells, NKT/ILC1 cells, other T cells/ILC.

I, J. Alternative antibody panel used to stain macrophages and DC was performed using MerTK, CD26, XCR1 and CD172a which confirmed the presence of macrophage markers on MM, cDC2 markers on CD11b+ DC and cDC1 markers on CD11b- DC. The isotype is gated from the macrophage population. Representative histograms (I) and gating strategy (J) are indicated.

Supplementary Figure 2. MM composition of CD3$^{-/-}$ mice; monocyte input in adult MM maintenance; dextran uptake by MM using flow cytometry (related to Figure 1)

A-D. Meninges of WT and CD3$^{-/-}$ mice were analyzed by flow cytometry. (A, B) Representative contour plot (A) and quantification (B) of Thy1.2^{+} cells showing the lack of CD4^{+} and CD8^{+} T cells in the meninges of CD3$^{-/-}$ mice. Bar graphs show the mean ± s.e.m. and asterisks denote statistical significance (****p<0.0001; Unpaired two-tailed Student's *t*-test with Holm-Sidak test for pairwise comparison). Data are representative of 2 independent experiments with 5 (WT) and 4 (CD3$^{-/-}$) mice per group. (C, D) Representative contour plot (C) and quantification (D) of the proportion of MHC-II+ MM in the meninges of CD3$^{-/-}$ mice. Bar graphs show the mean ± s.e.m. and asterisks denote statistical significance (*p<0.05; Unpaired two-tailed Student's *t*-test). Data are representative of 2 independent experiments with 5 (WT) and 4 (CD3$^{-/-}$) mice per group.

E, F. Cx3cr1-CreERT2 : R26-LSL-TdTomato mice were pulsed at 6 weeks old with tamoxifen. Myeloid cells from the dural meninges, brain, and blood were analyzed 2 months later by flow cytometry for TdTomato expression. The proportion of monocyte-derived cells, labelled in TdTomato, is indicated for each MM population. Bar graph shows mean ± s.e.m. for the indicated groups and asterisk denote statistical significance (*p<0.05; Unpaired two-tailed Student's *t*-test). Data are representative of 2 independent experiments, with 5 mice per group.

G. Ms4a3-Cre : R26-LSL-TdTom mice were analyzed at 3 months old (3MO) and 6 months old (6MO) by flow cytometry. The proportion of monocyte-derived cells, labelled in TdTomato, is indicated for each MM population. Bar graphs show the mean ± s.e.m. and asterisks denote statistical significance (*p<0.05; ****p<0.0001; ANOVA test with Holm-Sidak test for pairwise comparison). Data are representative of 4 independent experiments with 9 mice (3MO) or 6 mice (6MO) per group.

H-K. B6 mice were injected intravenously with PBS or 70 kDa fluorescent Dextran 60 min prior to sacrifice and dextran uptake by MM (H,I) and by other meningeal immune cells (J,K) was analyzed by flow cytometry. Representative FACS histograms of Dextran intensity for MM MHC-II+, MM MHC-II- (I) and CD11b+ DC (K) are shown in blue with the proportion of positive cells compared to control (grey). Bar graphs show the mean ± s.e.m. and asterisks denote statistical significance (ns=not significant; *p<0.05; ****p<0.0001; ANOVA test followed by Holm-Sidak multiple comparisons test (H), and Kruskall Wallis test followed by Mann-Whitney two-tailed test with Holm-Sidak correction for multiple analysis (J). Data are representative of 2 independent experiments with 6 mice (PBS) or 7 mice (Dextran) per group.

Supplementary Figure 3. MHC-II+ MM and MHC-II- MM respond to i.v. LPS challenge; confirmation of scRNAseq data at the protein level; MHC-II+ MM and MHC-II- MM putative interactions with meningeal cells upon LPS challenge (related to Figure 2)

A. UMAP representation of nucleated meningeal cells (7,035 cells). MM are indicated by the red box. Single-cell RNA sequencing was performed on 4 meningeal samples (from 2 mice injected with PBS and 2 with LPS) using 10X genomics and data was analyzed using Seurat software in combination with public datasets (http://brainimmuneatlas.org). Clustering was done with 50 dimensionalities of PCA, 30 number of neighbors and a resolution of Louvain's algorithm of 2 and the 29 clusters were regrouped into 16 cell clusters to facilitate visualization, based on similarity of their marker genes.

B-E. Pseudo-time inference of the activation trajectory of macrophages. (B,C) Activation trajectory of MHC-II+ MM. Results using Monocle algorithm on MHC-II+ MM (PBS) combined with MHC-II- and MHC-II+ (LPS). Cell color corresponds to MM cluster (B) or pseudo-time scores computed by Monocle (C). (D,E) Activation trajectory of MHC-II- MM. Results using Monocle algorithm on MHC-II- MM (PBS) combined with MHCII- and MHC-II+ (LPS). Cell color corresponds to MM cluster (D) or pseudo-time scores computed by Monocle (E). Of note, an inferred activation trajectory should only be used to follow cells between a non-activated condition (PBS) and an activated condition (LPS). Thus, the connection between MHC-II+ and MHC-II- upon LPS is not biologically relevant.

F-H. B6 mice were injected intravenously with PBS or LPS 24 hours prior to sacrifice and MM MHC-II+ and MHC-II- MM populations were analyzed by flow cytometry for the expression of surface markers (BST2, CD38, CD55, CD68). Representative FACS histograms are shown (F). Bar graphs (G) show the mean ± s.e.m. and asterisks denote statistical significance (*p<0.05; **p<0.01; ****p<0.0001; Unpaired two-tailed Student's *t*-test (BST2, CD38, CD55) and Mann-Whitney two-tailed test (CD68) with Holm-Sidak test for multiple analysis). Data are representative of 2 experiments with 5 mice per group. (H) Violin plots of Bst2, Cd38, Cd55 and Cd68 expression, in each macrophage population (extracted from our single-cell data set), are shown (ns=not significant; *p<0.05; **p<0.01; ****p<0.0001; Wilcoxon Rank Sum test with Bonferroni correction for multiple analysis).

I, J. Ligand-receptor interactions between MHC-II+ MM versus MHC-II- MM and all meningeal cells were analyzed using NicheNet and CellChat R packages. Representation of sent and received interactions from MHC-II+ MM (I) and MHC-II- MM (J) cells in LPS condition were given by CellChat analyses. Edge colors are consistent with the sources as sender, and edge weights are proportional to the interaction strength. Thicker edge line indicates a stronger signal. Circle sizes are proportional to the number of cells in each cell group. A schematic example of sent/received ligands, facilitating the reading of the diagram, is given on the left.

K. Analysis of potential ligands ('Sent ligands upon LPS'), computed by Nichenet, expressed by MHC-II+ and MHC-II- MM that could interact with their cognate receptors expressed by other meningeal cells. Average expression (color of the dot) and proportion expression (size of the dot) are indicated for each MM population with Seurat's function DotPlot.

Supplementary Figure 4. Changes in proportion of MHC-II+ MM upon LPS activation and upon LCMV infection; IL10R and IFNAR are involved in the changes in proportion of MHC-II+ MM upon LPS or LCMV infection respectively; infectious particles in the brain and meninges of LCMV-infected mice (related to Figure 2)

A-C. B6 mice were injected with LPS i.v. Twenty-four hours later, dural MM were analyzed by *in situ* histocytometry for MHC-II expression. (A) Representative confocal image of MM from PBS and LPS-injected mice. Scale bar: 200 µm. (B) *In situ* histocytometry analysis showing a representative contour plot of MM from PBS and LPS-injected mice. (C) Quantification of the proportion of MHC-II+ MM in the meninges of PBS and LPS-injected mice. Bar graphs show the mean ± s.e.m. and asterisks denote statistical significance (***p<0.001; Unpaired two-tailed Student's *t*-test). Data are representative of 2 independent experiments with 4 mice per group.

D-G. MM were identified based on CD206 staining, with MHC-II subsets, 48 h after intravenous PBS or LCMV injections. MHC-II+ and MHC-II- MM density (D, F) and MHC-II+ MM proportion (E, G) was calculated by histocytometry 48 h after PBS or LCMV intravenous injection in the suture (D, E) and the lobes (F, G). Bar graphs show the mean ± s.e.m. and asterisks denote statistical significance (ns=not significant; **p<0.01; ****p<0.0001; ANOVA test followed by unpaired two-tailed Student's *t*-test with Holm-Sidak test for pairwise comparison for D and F, and Mann-Whitney two-tailed test for E and G). Data are representative of 4 independent experiments with 8 mice (PBS) and 9 mice (LCMV) per group.

H-K. Mice were pretreated transcranially and i.v. with IL10R blocking antibody (α-IL10R) or isotype control (Iso) for 4 hours and then injected with PBS or LPS i.v. Twenty-four hours later, MM were analyzed by flow cytometry to assess levels of MHC-II. Representative flow plots are indicated (H) and proportion of MHC-II+ MM is quantified (I). Bar graphs show the mean ± s.e.m. and asterisks denote statistical significance (ns=not significant, *p<0.05, ***p<0.001; One-way ANOVA test with Holm-Sidak test for pairwise comparison). Data are representative of 2 independent experiments with 6 mice (Iso) and 7 mice (α-IL10R) per group. (J) Mice were pretreated transcranially and i.v. with IL10R blocking antibody (α-IL10R) or isotype control (Iso) for 4 hours and then injected with PBS or LCMV i.v. Forty eight hours later, MM were analyzed by flow cytometry to assess the levels of MHC-II in MM. The proportion of MHC-II+ MM is quantified. Bar graphs show the mean ± s.e.m. and asterisks denote statistical significance (ns=not significant, ***p<0.001; One-way ANOVA test followed with Holm-Sidak test for

pairwise comparison). Data are representative of 2 independent experiments with 4 mice per group. (K) Cd163-Cre : Ifnar$^{fl/fl}$ mice and controls were injected with PBS or LCMV and their meninges were analyzed 48 hours later by flow cytometry to assess the levels of MHC-II in MM. The proportion of MHC-II+ MM is quantified. Bar graphs show the mean ± s.e.m. and asterisks denote statistical significance (ns=not significant, ****p<0.0001; One-way ANOVA test followed with Holm-Sidak test for pairwise comparison). Data are representative of 2 independent experiments with 9 mice (Control + PBS), 8 mice (Cd163-Cre : Ifnar$^{fl/fl}$ + PBS), 9 mice (Control + LCMV) and 10 mice (Cd163-Cre : Ifnar$^{fl/fl}$ + LCMV) per group.
L-N. B6 mice were injected with PBS or LCMV and CD45-negative meningeal cells, which are the main targets of LCMV, were analyzed by flow cytometry 6 days later and stained for LCMV. Representative FACS plots of LCMV staining (gated on CD45-negative cells) are shown for PBS- and LCMV-injected mice (L). Meninges and brains of mock and LCMV-infected mice were collected at day 6 post infection, and their infectivity was quantified on Vero cells by flow cytometry (M) and by plaque assay (N). Bar graphs show the mean ± s.e.m. and asterisks denote statistical significance (ns=not significant, *p<0.05; ***p<0.001; Mann-Whitney two-tailed test). Data are representative of 2 independent experiments with 6 mice (PBS) or 9 mice (LCMV) per group (L) and 6 mice (PBS) or 8 mice (LCMV) per group (M,N).

Supplementary Figure 5. Viral load upon genetic MM depletion and role of *Stat1* and *Ifnar* in macrophages upon LCMV infection; meningeal immune cell composition and viral load upon LCMV challenge in MM- and CD8+ T or CD4+ T- depleted mice; meningeal immune cell composition and viral load upon LCMV challenge in Cd163-Cre : H2-Ab1$^{fl/fl}$ mice; absence of major vascular leak in the absence of meningeal macrophages; effect of PLX3397 on macrophages/DC being independent of the gating strategy (related to Figure 5)

A. LCMV mRNA levels were quantified by RT-qPCR in the spleens of Cd163-Cre : Csf1r-LSL-DTR mice and controls treated with DT, at day 6 post-infection. LCMV mRNA levels were significantly higher in Cd163-Cre : Csf1r-LSL-DTR mice. Bar graphs show the mean ± s.e.m. and asterisks denote statistical significance (****p<0.0001; Mann-Whitney two-tailed test). Data are representative of 3 independent experiments with 11 mice (Control + DT + LCMV) and 14 mice (Cd163-Cre : Csf1r-LSL-DTR + DT + LCMV) per group.
B-D. LysM-Cre : Stat1$^{fl/fl}$ mice and controls were injected intravenously with LCMV. (B) Survival was monitored (ns=not significant; Log-rank Mantel Cox test). (C) Weight was measured in LysM-Cre : Stat1$^{fl/fl}$ mice and controls following infection. Graphs show the mean ± s.e.m. and asterisks denote statistical significance (ns=not significant; *p<0.05; **p<0.01; ***p<0.001; One-way ANOVA test followed by unpaired two-tailed Student's *t*-test with Holm-Sidak test for pairwise comparison). Data are representative of 2 independent experiments with 6 mice

(Control + LCMV) and 14 mice (LysM-Cre : Stat1$^{fl/fl}$ + LCMV) per group. (D) LCMV mRNA levels were quantified by RT-qPCR in the spleens of LysM-Cre : Stat1$^{fl/fl}$ mice and compared with controls. Bar graphs show the mean ± s.e.m. and asterisks denote statistical significance (*p<0.05; Mann-Whitney two-tailed test). Data are representative of 2 independent experiments with 6 mice (Control + LCMV) and 4 mice (LysM-Cre : Stat1$^{fl/fl}$ + LCMV) per group. E, F. Cd163-Cre : Stat1$^{fl/fl}$ mice and controls were injected intravenously with LCMV. (E) Survival was monitored (ns=not significant; Log-rank Mantel Cox test). (F) Weight was measured in Cd163-Cre : Stat1$^{fl/fl}$ mice and controls following infection. Graphs show the mean ± s.e.m. (ns=not significant, Kruskall Wallis test followed by Mann-Whitney two-tailed test with Holm-Sidak correction for multiple analysis). Data are representative of 2 independent experiments with 3 mice (Control + LCMV) and 7 mice (Cd163-Cre : Stat1$^{fl/fl}$ + LCMV) per group.

G. MM-negative fraction and MM fraction of the dural meninges were sorted from Cd163-Cre : Ifnar$^{fl/fl}$ mice and controls. Detection of the excised *Ifnar* cDNA (exon 10) was performed by RT-qPCR for detection of the complete version (Tm~82°C, 0.2kb) and the excised version (Tm~78°C, 0.07kb). Representative gel of actin amplicons and Ifnar amplicons (exon 9->11) are shown (1kb DNA ladder starting at 0.1kb) (left). Plots of corresponding melting curves are indicated (middle). Graphs show the mean ± s.e.m. and asterisks denote statistical significance (ns=not significant; ****p<0.001; unpaired two-tailed Student's *t*-test with Holm-Sidak test for pairwise comparison) (right). Data are representative of 2 experiments with 4 mice per group.

H-J. Cd163-Cre : Ifnar$^{fl/fl}$ mice and controls were injected intravenously with LCMV. (H) Survival was monitored (**p<0.01; Log-rank Mantel Cox test). (I) Weight was measured in Cd163-Cre : Ifnar$^{fl/fl}$ mice and controls following infection. Graphs show the mean ± s.e.m. (ns=not significant; *p<0.05; **p<0.01; ***p<0.001; ****p<0.0001; Kruskall Wallis test followed by Mann-Whitney two-tailed test with Holm-Sidak correction for multiple analysis). Data are representative of 2 independent experiments with 15 mice (Control + LCMV) and 15 mice (Cd163-Cre : Ifnar$^{fl/fl}$ + LCMV) per group. (J) LCMV mRNA levels were quantified by RT-qPCR in the spleens of Cd163-Cre : Ifnar$^{fl/fl}$ mice and compared with controls. Bar graphs show the mean ± s.e.m. and asterisks denote statistical significance (***p<0.001; Mann-Whitney two-tailed test). Data are representative of 2 independent experiments with 10 mice (Control + LCMV) and 9 mice (Cd163-Cre : Ifnar$^{fl/fl}$ + LCMV) per group.

K,L. Cd163-Cre : Csf1r-LSL-DTR mice and controls were injected with 100 ng of diphtheria toxin (DT) transcranially at days -2 and -1 to deplete myeloid cells and then injected intravenously with LCMV at day 0. CD8-depleting antibodies were injected at day 3 and day 5 p.i.. At day 6 p.i., meningeal immune cells were analyzed by flow cytometry (K), and brains and spleens were analyzed by RT-qPCR to quantify viral loads (L). Bar graphs show mean

± s.e.m (ns=not significant; *p<0.05; **p<0.01; Kruskall Wallis test followed by Mann-Whitney two-tailed test with Holm-Sidak correction for multiple analysis for K, and Mann-Whitney two-tailed test for L). Data are representative of 2 independent experiments with 7 (control) and 6 (Cd163-Cre : Csf1r-LSL-DTR) mice per group.

M,N. Cd163-Cre : Csf1r-LSL-DTR mice and controls were injected with 100 ng of diphtheria toxin (DT) transcranially at days -2 and -1 to deplete myeloid cells and then injected intravenously with LCMV at day 0. CD4-depleting antibodies were injected at day 3 and day 5 p.i.. At day 6 p.i., meningeal immune cells were analyzed by flow cytometry (M), and brains and spleens were analyzed by RT-qPCR to quantify viral loads (N). Bar graphs show mean ± s.e.m (ns=not significant; *p<0.05; **p<0.01; Kruskall Wallis test followed by Mann-Whitney two-tailed test with Holm-Sidak correction for multiple analysis for M, and Mann-Whitney two-tailed test for N). Data are representative of 2 independent experiments with 7 (control) and 5 (Cd163-Cre : Csf1r-LSL-DTR) mice per group.

O,P. Cd163-Cre : H2-Ab1$^{fl/fl}$ mice and controls were infected with LCMV i.v. Six days later, dural MM were analyzed by flow cytometry for MHC-II expression (O) and brains and spleens were used to quantify LCMV viral load by RT-qPCR (P). Bar graphs show the mean ± s.e.m. and asterisks denote statistical significance (ns=not significant, ****p<0.001; Unpaired two-tailed Student's *t*-test for O and Mann-Whitney two-tailed test for P). Data are representative of 2 independent experiments with 6 mice per group.

Q. Cd163-Cre : H2-Ab1$^{fl/fl}$ mice and controls were infected with LCMV i.v. Six days later, dural meninges were stained for Ly6C (vessels/monocytes), CD64 (macrophages), MHC-II and LCMV. LCMV staining was below detection levels in the meninges of both genotypes. Representative images of 2 experiments with 3 mice per group.

R-S. Cd163-Cre : Csf1r-LSL-DTR mice and controls were injected with 100 ng of diphtheria toxin (DT) transcranially at days -2 and -1 to deplete myeloid cells and then injected intraperitoneally with Evans Blue for 1 hour. As a positive control, a group of littermate controls was injected with 5 µl PBS i.c. 1 hour before injection of Evans Blue. Representative images are shown for each group showing macrophages (CD206, blue), blood vessels (Ly6C, red) and Evans blue (Green) (R). Bar graphs show mean ± s.e.m (ns=not significant; ****p<0.0001; One-way ANOVA test followed by with Holm-Sidak test for pairwise comparison (S). Scale bar: 200 µm. Data are representative of 2 independent experiments with 5 (control + DT), 5 (Cd163-Cre : Csf1r-LSL-DTR + DT) and 4 (positive control) mice per group.

Supplementary Figure 6. Pharmacological depletion of MM using PLX3397 and PLX5622 result in fatal meningtis (related to Figure 6)

A. B6 mice were injected transcranially with mock or PLX3397 and meningeal samples were analysed by flow cytometry based on cDC1/cDC2 gating strategy to assess macrophages

(gated on CD45$^+$ CD64$^+$ F4/80$^+$ CD206$^+$ cells, with MHC-II subsets) and DC (gated on CD45$^+$ CD64$^-$ F4/80$^-$ Thy1.2$^-$ MHC-II$^+$ CD11c$^+$ CD26$^+$ XCR1$^+$ CD172a$^-$ cells for cDC1 and CD45$^+$ CD64$^-$ F4/80$^-$ Thy1.2$^-$ MHC-II$^+$ CD11c$^+$ CD26$^+$ XCR1$^-$ CD172a$^+$ cells for cDC2) depletion. Bar graphs show the mean ± s.e.m. and asterisks denote statistical significance (ns=not significant; *p<0.05; **p<0.01; Unpaired two-tailed Student's *t*-test with Holm-Sidak test for pairwise comparison). Data are representative of 2 independent experiments with 5 (Mock) and 7 (PLX3397) mice per group.

B, C. B6 mice were injected with mock or PLX5622 transcranially at day 0, 2, 4 and sacrificed at day 6. Meninges were analyzed by flow cytometry using usual strategy (B) or cDC1/cDC2 gating strategy (C), in which macrophages were gated on CD45$^+$ CD64$^+$ F4/80$^+$ CD206$^+$ cells, with MHC-II subsets and DC were gated on CD45$^+$ CD64$^-$ F4/80$^-$ Thy1.2$^-$ MHC-II$^+$ CD11c$^+$ CD26$^+$ XCR1$^+$ CD172a$^-$ cells for cDC1 and CD45$^+$ CD64$^-$ F4/80$^-$ Thy1.2$^-$ MHC-II$^+$ CD11c$^+$ CD26$^+$ XCR1$^-$ CD172a$^+$ cells for cDC2. Bar graphs show the mean ± s.e.m. and asterisks denote statistical significance (ns=not significant; *p<0.05; **p<0.01; Kruskall Wallis test followed by Mann-Whitney two-tailed test with Holm-Sidak correction for multiple analysis). Data are representative of 3 independent experiments with 11 mice (Mock) or 13 mice (PLX5622) per group.

D, E. Pia whole mounts (D) and brains (E) of mock- or PLX5622-injected mice were analyzed for pial macrophage counts and microglia respectively, based on CD206 staining (D) and IBA1 staining (E). Bar graphs show the mean ± s.e.m. and asterisks denote statistical significance (ns=not significant; ****p<0.0001; Unpaired two-tailed Student's *t*-test). Data are representative of 2 independent experiments with 11 mice (Mock, D), 12 mice (PLX5622, D), 6 mice (Control, E) and 11 mice (PLX5622, E) per group.

G. Mock- or PLX5622-injected mice were infected with LCMV and six days later, meningeal immune cells were analyzed by flow cytometry. Bar graphs show the mean ± s.e.m. and asterisks denote statistical significance (ns=not significant; *p<0.05; **p<0.01; ***p<0.001; Kruskall Wallis test followed by Mann-Whitney two-tailed test with Holm-Sidak correction for multiple analysis). Data are representative of 2 independent experiments 13 mice (PBS) and 22 mice (LCMV) per group.

G, H. Control or PLX5622-injected mice were infected with LCMV and six days later, brains (G) and spleens (H) were analyzed by RT-qPCR to measure LCMV viral load. Bar graphs show the mean ± s.e.m. and asterisks denote statistical significance (*p<0.05; **p<0.01; Mann-Whitney two-tailed test). Data are representative of 2 independent experiments with 10 mice (PBS) and 22 mice (LCMV) per group for the brains, and 13 mice (PBS) and 22 mice (LCMV) per group for the spleens.

I. Survival curves of PLX5622-treated mice or control mice after LCMV infection. Asterisks denote statistical significance (*p<0.05; Log-rank Mantel Cox test). Data are representative of 2 independent experiments with 15 mice (Control + LCMV) and 8 mice (PLX5622 + LCMV) per group.

Supplementary Figure 7. Meningeal immune cell composition upon LCMV challenge in models of reduced MHC-II+ MM levels (LPS and age); meningeal rejuvenation protocol and kinetics; meningeal immune cell composition and viral load upon LCMV challenge in rejuvenated mice (related to Figure 7)

A, B. Mice were subjected to an injection of lipopolysaccharide (LPS) or of saline solution (PBS) before infection with LCMV. Dural meninges were analyzed by flow cytometry before (A) and after (B) injection with LCMV. Neutrophils, monocytes, other macrophages, $CD11b^+$ DC, $CD11b^-$ DC, $CD8^+$ T cells, $CD4^+$ T cells, NKT/ILC1 cells were enumerated. Bar graphs show the mean ± s.e.m. for the indicated groups (ns=not significant; *p<0.05; Kruskall Wallis test followed by Mann-Whitney two-tailed test with Holm-Sidak correction for multiple analysis). Data are representative of 3 independent experiments with 7 mice (PBS) and 6 mice (LPS) per group (A) and 6 mice (PBS + LCMV) and 8 mice (LPS + LCMV) per group (B).

C. Four months-old (4MO) and one month-old (1MO) mice were injected with LCMV. Dural meninges were analyzed by flow cytometry 6 days later. Neutrophils, monocytes, MM, other macrophages, $CD11b^+$ DC, $CD11b^-$ DC, $CD8^+$ T cells and $CD4^+$ T cells were enumerated. Bar graphs show the mean ± s.e.m. for the indicated groups, and asterisks denote statistical significance (ns=not significant; *p<0.05; **p<0.01; ***p<0.001; Kruskall Wallis test followed by Mann-Whitney two-tailed test with Holm-Sidak correction for multiple analysis). Data are representative of 3 independent experiments with 11 mice per group.

D-G. Mice were subjected to meningeal 'rejuvenation'. LysM-Cre : Csf1r-LSL-DTR mice (Rejuvenated) and controls were injected with 100 ng of diphtheria toxin (DT) transcranially at days 0 and 1 to deplete myeloid cells and then injected intravenously with blocking antibodies (anti-LFA/VLA) at day 2 and day 3 to promote local MM MHC-II- cells proliferation over MM MHC-II+ cells infiltration. (D) The kinetics of MM recovery was analyzed by confocal imaging and quantified, in the MHC-II+ and the MHC-II- MM compartments, at day 1, 4 and 8 post initial DT injection, in 4 different meningeal regions of the lobes (frontal, interparietal/occipital, parietal and suture). Bar graphs show the mean ± s.e.m. and asterisks denote statistical significance (ns=not significant; *p<0.05; **p<0.01; ***p<0.001; ****p<0.0001; One-way ANOVA test followed by unpaired two-tailed Student's *t*-test with Holm-Sidak test for pairwise comparison). Data are representative of 2 independent experiments with 3 mice (Control) and 5 mice (Rejuvenated) per group and 2 to 3 regions were quantified per mouse. (E) Maximal intensity projections of meningeal whole mounts of rejuvenated and control mice at day 1, 4

and 8 post initial DT injection. The first row shows the whole dural meninges of control mice and rejuvenated mice. The 2nd and 3rd rows show magnification of the red insets (R1, R3). Scale bar: 3 mm (whole meninges) and 100 µm (insets). Data are representative of 2 independent experiments with 3 mice (Control) and 4 mice (Rejuvenated) per group. D1, D4, D8: days post-DT injection. (F) Maximal intensity projection of a region of meningeal whole mounts of rejuvenated and control mice showing proliferating cells (EDU^+, yellow) among MM (red) at day 8 post-treatment. (G) Quantification of four different meningeal regions (frontal, interparietal/occipital, parietal and suture) from confocal images of meningeal whole mounts of rejuvenated and control mice. Scale bar: 50 µm. Bar graphs show the mean ± s.e.m. and asterisks denote statistical significance (ns=not significant; *p<0.05; Unpaired two-tailed Student's *t*-test with Holm-Sidak test for pairwise comparison). Data are representative of 2 independent experiments with 3 mice (Control) and 4 mice (Rejuvenated) per group and 1 to 3 regions were quantified per mouse.

H, I. Mice were subjected to 'meningeal rejuvenation'. LysM-Cre : Csf1r-LSL-DTR mice (Rejuvenated) and controls were injected with 100 ng of diphtheria toxin (DT) transcranially at days 0 and 1 to deplete myeloid cells and then injected intravenously with blocking antibodies (anti-LFA/VLA) at day 2 and day 3 to promote local MM MHC-II- cells proliferation over MM MHC-II+ cells infiltration. (H) At day 8 post initial DT injection, neutrophils, monocytes, other macrophages, $CD11b^+$ DC, $CD11b^-$ DC, $CD8^+$ T cells, and $CD4^+$ T cells were analyzed by flow cytometry. Bar graphs show mean ± s.e.m (ns=not significant; Kruskall Wallis test followed by Mann-Whitney two-tailed test with Holm-Sidak correction for multiple analysis). Data are representative of 2 independent experiments with 5 mice per group. (I) At day 8 post first DT injection, mice were infected with LCMV. Six days later, neutrophils, monocytes, MM, other macrophages, $CD11b^+$ DC, $CD11b^-$ DC, $CD8^+$ T cells, and $CD4^+$ T cells were assessed by flow cytometry. Bar graphs show mean ± s.e.m (ns=not significant, Kruskall Wallis test followed by Mann-Whitney two-tailed test with Holm-Sidak correction for multiple analysis). Data are representative of 2 independent experiments with 8 mice (Control + LCMV) and 5 mice (Rejuvenated + LCMV) per group.

J. LCMV mRNA levels at day 6 post-infection were quantified by RT-qPCR in the spleens of rejuvenated mice and compared with controls. Bar graphs show the mean ± s.e.m. and asterisks denote statistical significance (**p<0.01; Mann-Whitney two-tailed test). Data are representative of 2 independent experiments with 8 mice (Control + LCMV) and 7 mice (Rejuvenated + LCMV) per group.

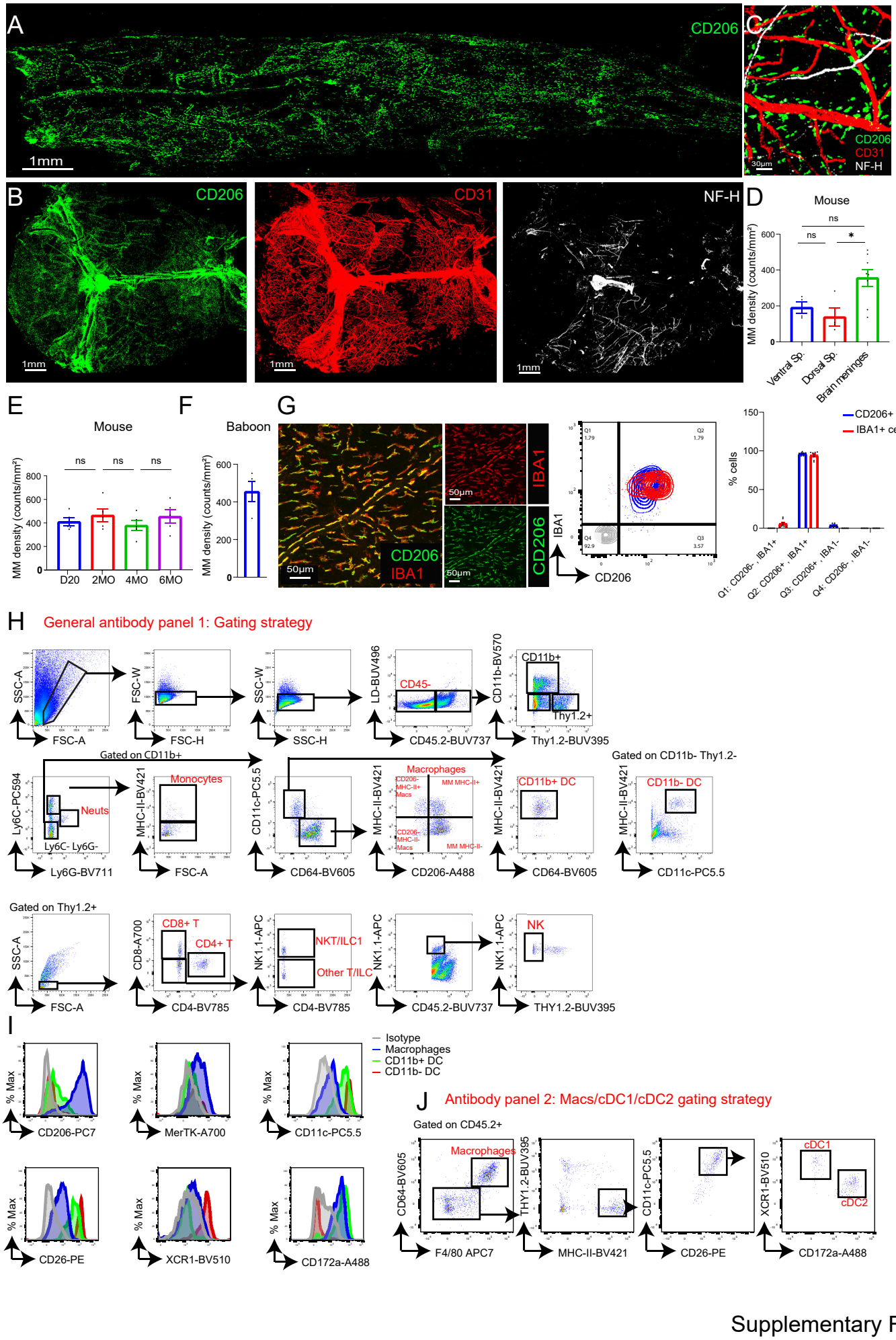

Supplementary Figure S1

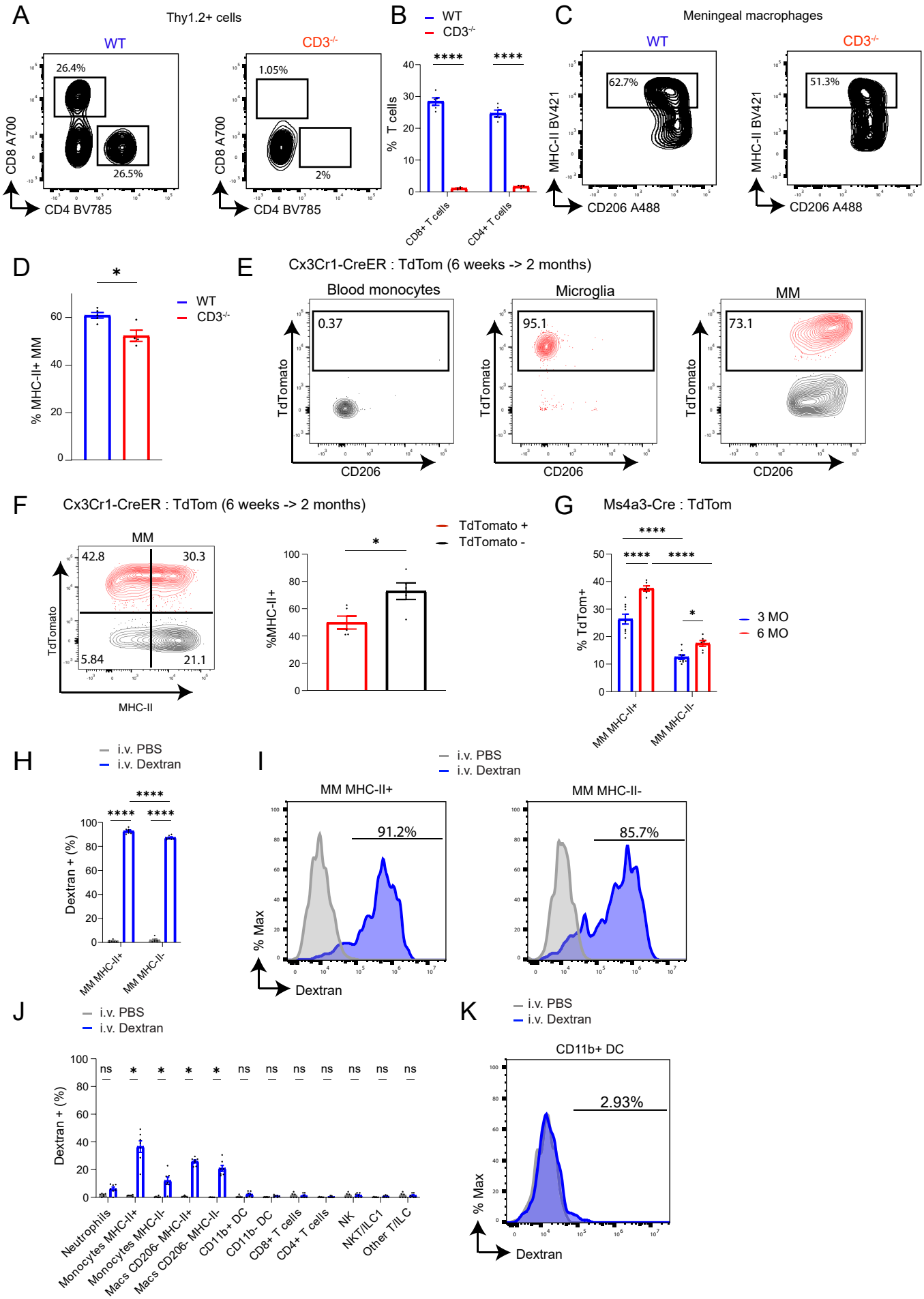

Supplementary Figure S2

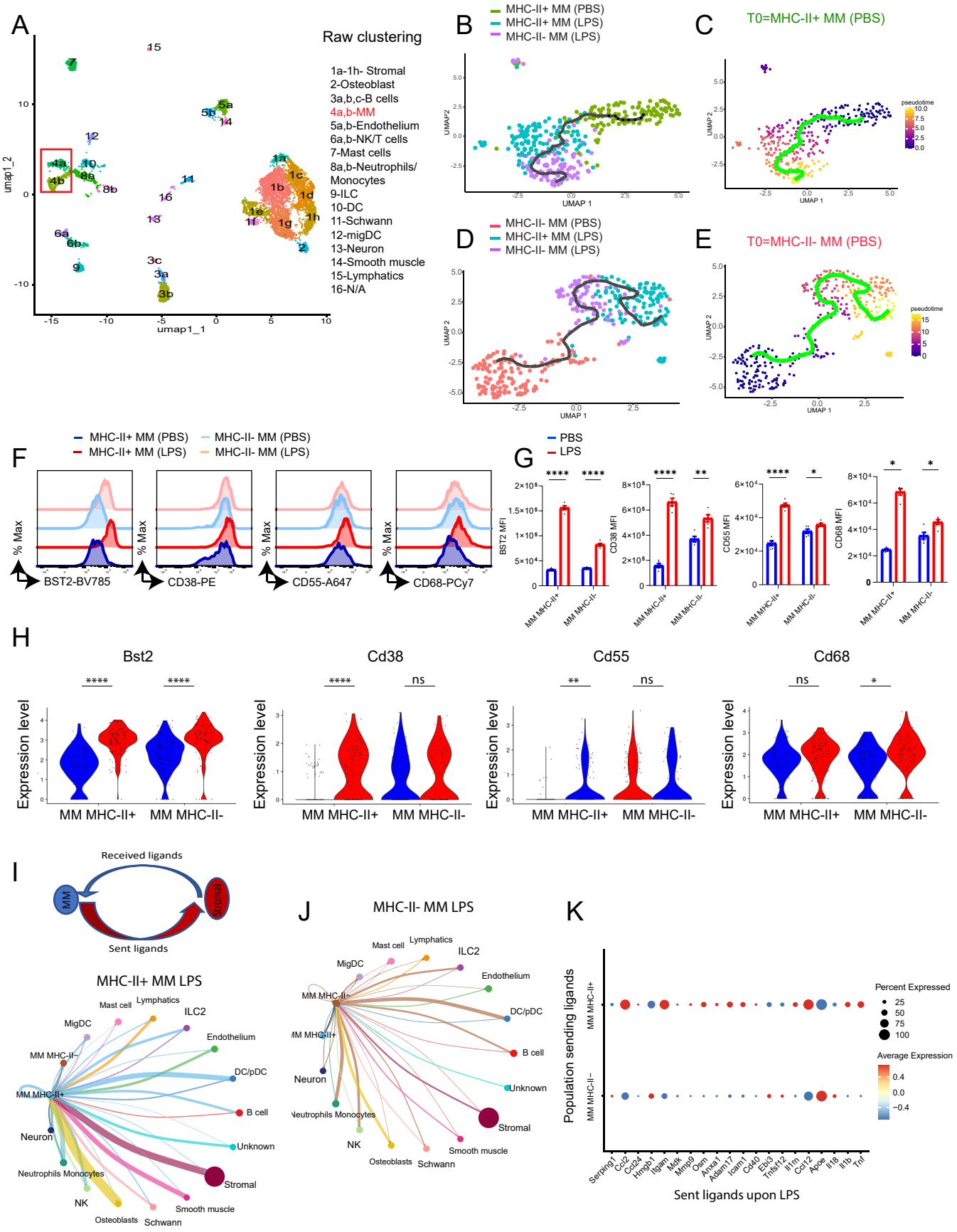

Supplementary Figure S3

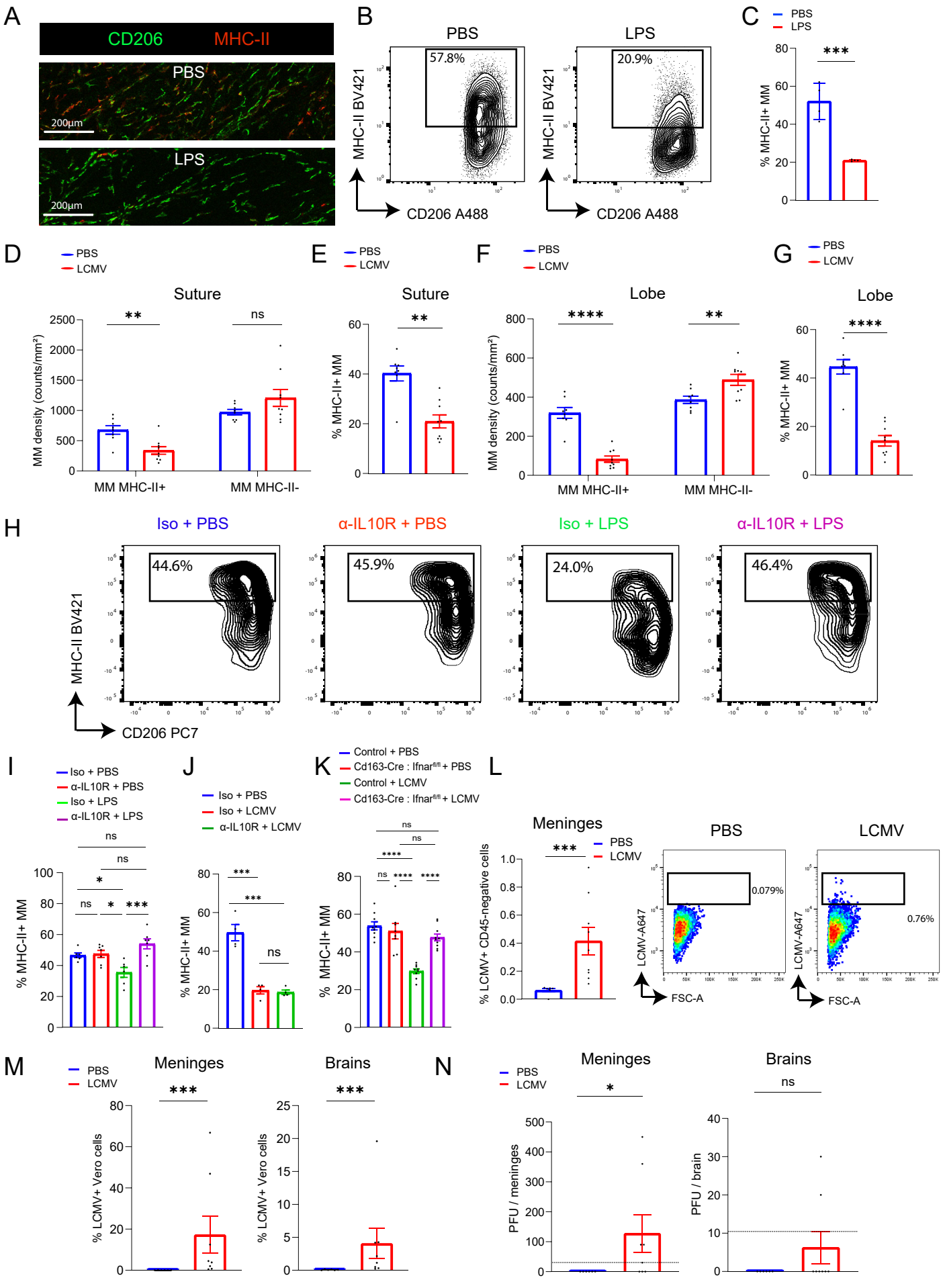

Supplementary Figure S4

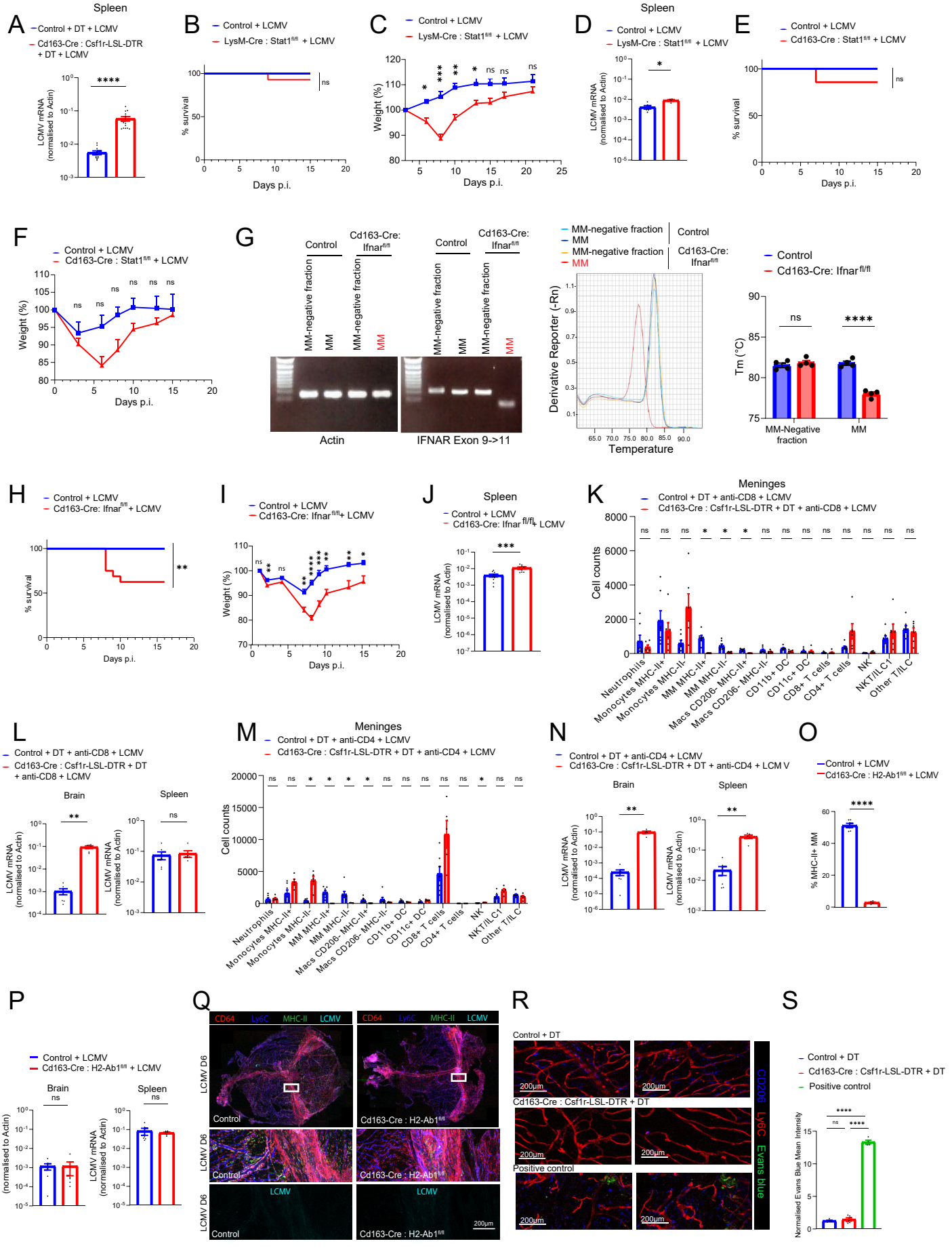

Supplementary Figure S5

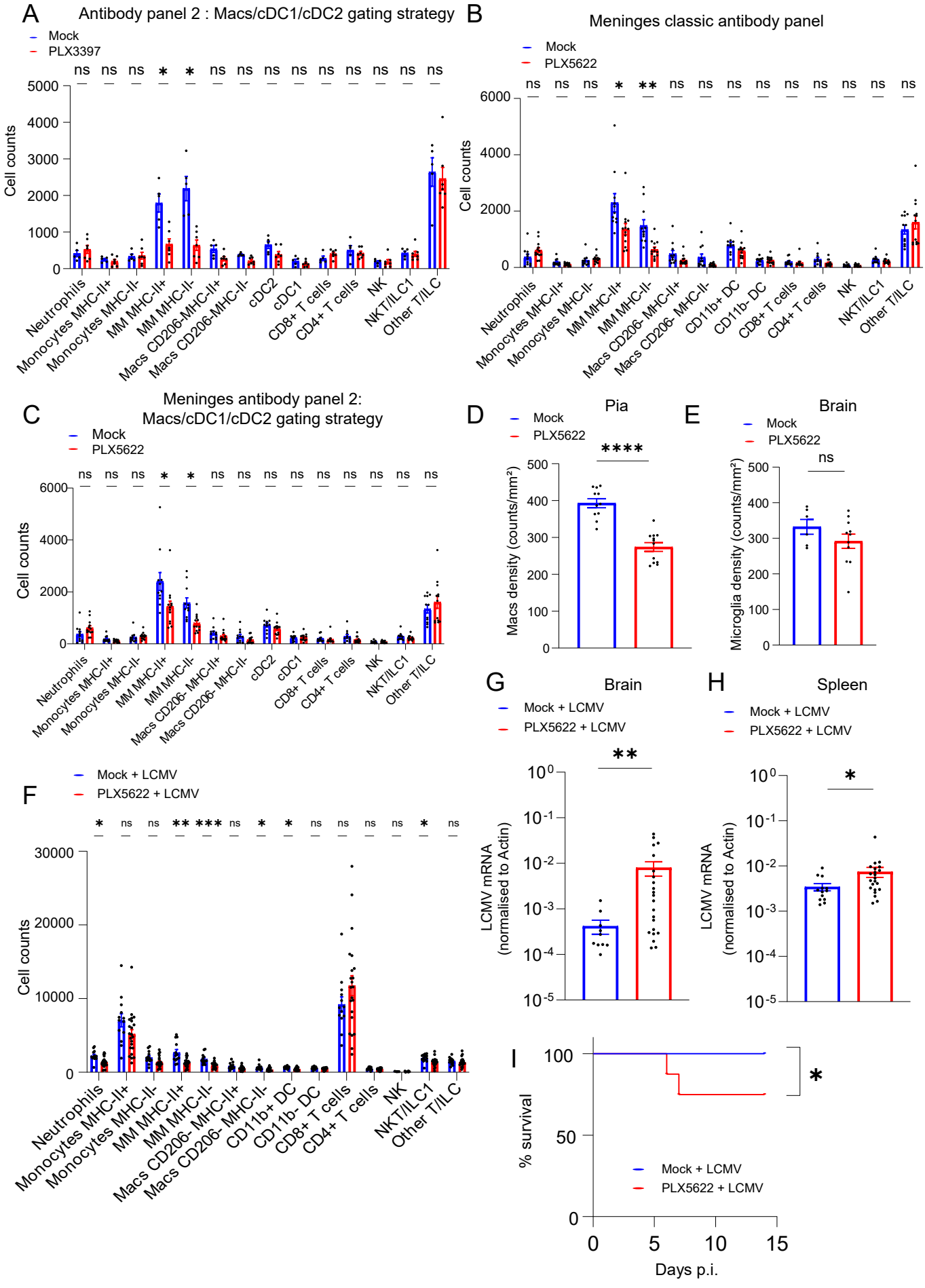

Supplementary Figure S6

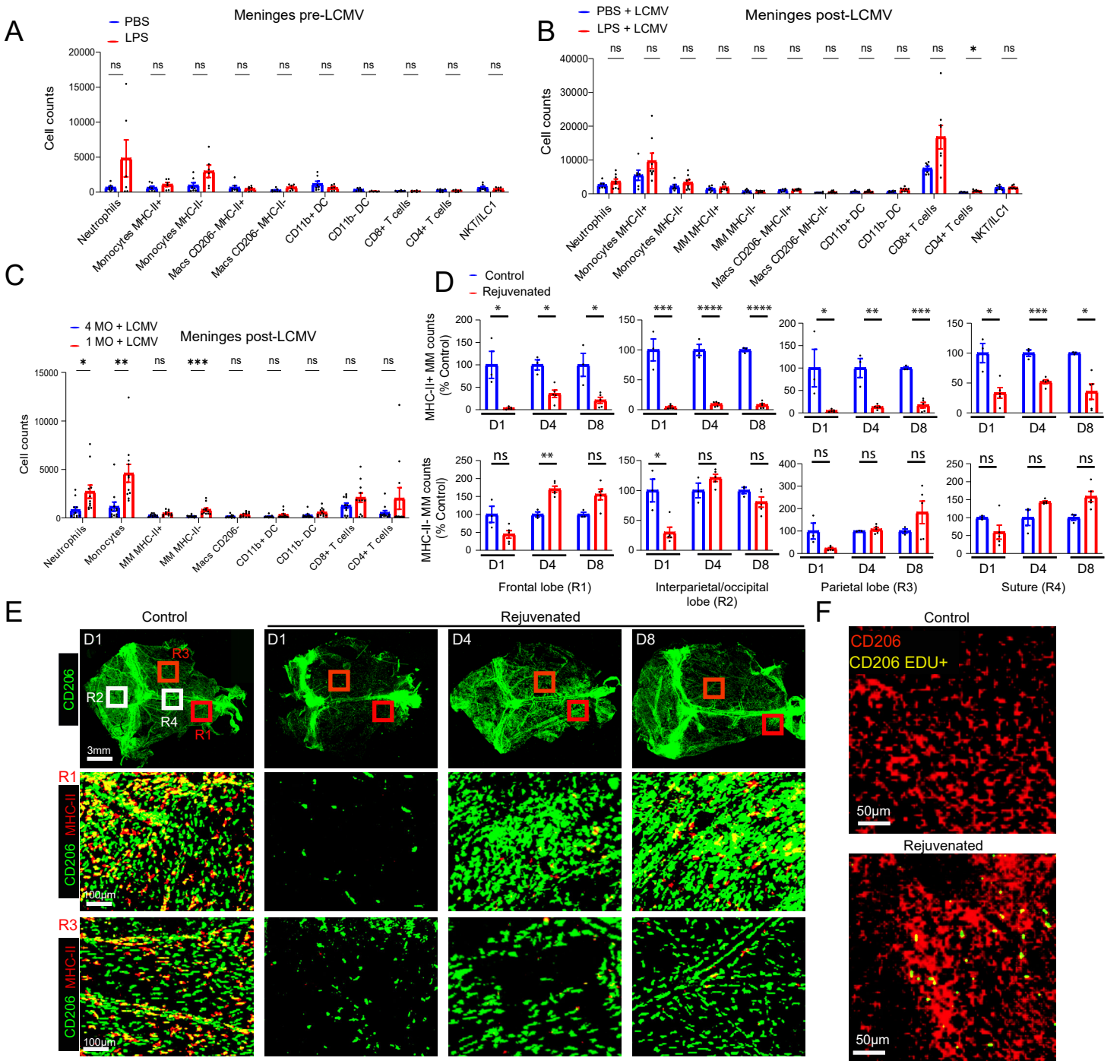

Supplementary Figure S7

Supplemental Table 1

Click here to access/download

Supplemental Videos and Spreadsheets

Supplementary Table 1.xlsx

Supplemental Table 2

Click here to access/download

Supplemental Videos and Spreadsheets

Supplementary Table 2.xlsx